LEHRSTUHL FÜR BIOMEDIZINISCHE PHYSIK
TECHNISCHE UNIVERSITÄT MÜNCHEN

Advanced Acquisition Methods
for
Anisotropic X-ray Dark-field Imaging

Yash Sharma

PhD Thesis

March, 2018

Supervisors:
Dr. Tobias Lasser
Prof. Dr. Franz Pfeiffer

Technische Universität München

TECHNISCHE UNIVERSITÄT MÜNCHEN
Physik Department
Lehrstuhl für Biomedizinische Physik

Advanced Acquisition Methods
for
Anisotropic X-ray Dark-field Imaging

Yash Sharma

Vollständiger Abdruck der von der Fakultät für Physik der Technischen Universität München zur Erlangung des akademischen Grades eines

Doktors der Naturwissenschaften (Dr. rer. nat.)

genehmigten Dissertation.

Vorsitzender: Prof. Dr. Martin Zacharias

Prüfer der Dissertation: 1. Prof. Dr. Franz Pfeiffer

2. Priv.-Doz. Dr. Tobias Lasser

Die Dissertation wurde am 20.03.2018 bei der Technischen Universität München eingereicht und durch die Fakultät für Physik am 08.06.2018 angenommen.

To my parents . . .

Abstract

X-ray Dark-field is a relatively new contrast mechanism that combines the high resolution of X-ray scattering to the large field-of-view of X-ray imaging. It exhibits the property of orientation-selectivity, which forms the basis of a new sub-category of imaging methods, namely, Anisotropic X-ray Dark-field (AXDF) imaging. AXDF imaging utilizes the orientation selectivity of the dark-field signal to reveal information about sub-pixel sized structures without the need of directly resolving them. In addition, AXDF tomography aims at the reconstruction of the three dimensional scattering information inside every three dimensional volume element.

AXDF imaging is a suitable candidate for non-destructive testing, a field with an ever increasing demand for higher resolution and larger field-of-view. Currently available high resolution imaging methods, such as X-ray micro Computed Tomography, are unable to meet these demands due to the trade-off between the spatial resolution and the measurable sample size. AXDF imaging, with at least two orders of magnitude difference between the size of the structures probed versus the size of the investigated sample, is a promising tool for this industry. However, AXDF imaging methods require bulky hardware and long acquisition time that severely hinder their translation to industrial applications. Development of optimized and industrially compatible AXDF acquisition protocols is the main goal of this thesis.

With the above goal in mind, we present a method for fast two dimensional AXDF imaging of continuously moving samples. Further, we investigate AXDF tomographic methods where the directional dependence of the dark-field signal renders standard tomographic acquisition unusable. We present two approaches to design tomographic acquisition schemes for optimal sampling of the real and reciprocal space, simultaneously. We validate the proposed methods with numerical and experimental analysis. In both cases, the proposed methods reduce the hardware and time complexity of two and three dimensional AXDF imaging methods and, hence, are a significant step forward for using these methods outside the laboratory.

Zusammenfassung

Das Röntgen-Dunkelfeld (XDF) ist eine neuartige Kontrastart welche die hohe Auflösung von Röntgen-Streumethoden mit dem großen Sichtfeld konventioneller Röntgen-Bildgebung verbindet. XDF ermöglicht die Detektion von richtungsabhängigen Streueigenschaften und bildet damit die Basis einer neuen Kategorie von Bildgebungsmethoden, der Anisotropischen Röntgen-Dunkelfeld (AXDF) Bildgebung. In Projektionsgeometrie kann man mittels AXDF die Orientierung von nicht direkt auflösbaren Mikrostrukturen untersuchen. Darauf aufbauend wird mittels AXDF-Tomographie die dreidimensionale Streuinformation in jedem Raumpunkt rekonstruiert.

AXDF hat viele potentielle Anwendungen in der zerstörungsfreien Werkstoffprüfung, einem Gebiet mit steigenden Anforderungen an hohe Auflösungen bei gleichzeitig großem Sichtfeld. Mikro-Tomographie, der aktuelle Gold-Standard in hochauflösender Bildgebung, kann diese Anforderungen nicht erfüllen da eine hohe Auflösung immer mit einem verkleinerten Sichtfeld verbunden ist. AXDF kann Strukturen mehr als zwei Größenordnungen unter der Probengröße detektieren und überwindet somit die Limitationen von Mikro-Tomographie. Um der Anwendung der AXDF-Bildgebung in der Industrie näher zu kommen, werden in dieser Dissertation ist die Entwicklung neuer und schnellerer Aufnahmemethoden mit reduzierter Hardware-Komplexität untersucht.

Das oben genannte Ziel vor Augen, präsentieren wir eine in der Industrie anwendbare Methode für zweidimensionale AXDF-Bildgebung mit kontinuierlicher Probenbewegung, beispielsweise durch ein Förderband. Darüber hinaus untersuchen wir AXDF-Tomographie für Fälle, in denen die Richtungsabhängigkeit des Dunkelfeldsignals eine konventionelle Tomographie unbrauchbar macht. Wir präsentieren neue Ansätze zur optimalen Abrasterung sowohl des Realraums als auch des reziproken Raums sowohl für die zweidimensionale als auch die dreidimensionale AXDF-Bildgebung. Die vorgeschlagenen Methoden werden numerisch und experimentell validiert. Die Optimierung erfolgt im Hinblick auf eine vereinfachte Aufnahme und höhere Aufnahmegeschwindigkeit und stellt somit einen signifikanten Schritt zur Anwendung dieser Methoden außerhalb des Labors dar.

Contents

List of Figures

List of Tables

Chapter 1

Introduction

X-rays are a form of electromagnetic waves discovered by William Conrad Roentgen in 1895. They have wavelengths typically in the range of 0.01 to 10 nm and energies in the range of 100 eV to 100 keV [Attwood (1999)]. Owing to the short wavelength, X-rays have the ability to penetrate matter. This was immediately clear with the first pictures taken with X-rays [Kevles (1997)]. Since then, X-rays have been crucial to the development of several fields of science including but not limited to physics, chemistry, material science and medicine. Moreover, a lot of these developments have made their way directly into the real world through applications such as the diagnosis of diseases in medicine and safety screening at airports.

X-ray Imaging is one of the foremost uses of X-rays in the real world. The easy application of X-ray Imaging stems from the fact that it relies on the phenomena of X-rays attenuation. Compared to other modes of X-ray interaction with matter, this is the one that is easy to measure and quantify. In simple terms, X-ray attenuation is analogous to shadows we see in everyday life. When a beam of visible light is obstructed by an opaque object, we see a shadow of the object. We can decipher the shape of an object merely by looking at the shadow. Since X-rays are able to penetrate matter, a shadow obtained using X-rays reveals the details of the internal structure of the object in addition to the outer shape. A significant step in the development of X-ray Imaging is X-ray Computed Tomography (CT) [Cormack (1963), Cormack (1964)]. By looking at the attenuation of an object from several directions, CT allows the reconstruction of the internal details in three dimensions.

X-ray Imaging has been used as a diagnostic tool in medicine and non-destructive testing for several decades. Over the years, significant advancements have been made in increasing the value of this tool by addressing aspects such as the spatial resolution and image quality. In an attempt to increase the spatial resolution of X-ray CT, another branch of methods have been developed under the category of industrial X-ray micro computed tomography (μCT) [Maire and Withers (2014)]. μCT aims at very high resolution imaging of material specimens. Industrial scanners have demonstrated resolution down to half a micrometer [Withers (2007)]. However, these systems suffer from a trade-off between the achievable resolution and the measurable sample size [Cnudde and Boone (2013)].

Recently, a novel model of contrast mechanism with X-rays, namely X-ray Dark-field imaging has shown promise to break this barrier.

X-ray Dark-field (XDF) [Pfeiffer et al. (2008)] is a relatively new contrast mechanism for X-rays. It originates from the small and ultra small angle scattering of X-rays. This is not the first time that scattering of X-rays is used for imaging. X-rays scattering based imaging methods [Guinier and Fournet (1955)] are commonly used to probe structures in the nano and micro meter regime. They probe the entire scattering (also known as reciprocal) space at one spatial location (pixel) in one measurement. As a result, scattering based imaging has, until recently, required a point-wise raster scanning approach [Fratzl et al. (1997), Rinnerthaler et al. (1999), Kinney et al. (2001)]. X-ray dark-field contrast mechanism combines the high reciprocal space resolution of scattering methods with the real space (spatial) resolution of imaging. This implies that we can probe information in the sub-micrometer regime and still measure macro sized samples without the need of raster scanning. This has opened an exciting research area aimed at the applications of this new contrast mechanism. Some applications that have been reported include lung imaging [Gromann et al. (2017), Hellbach et al. (2018)] , mammography [Rieger et al. (2013), Wang et al. (2014), Coello et al. (2017), Scherer et al. (2017)], cardiac imaging [Hetterich et al. (2017)], human joint imaging [Tanaka et al. (2013), Thüring et al. (2013)] and non-destructive testing [Nielsen et al. (2014), Gresil et al. (2017)].

An interesting property of X-ray dark field contrast is its anisotropicity [Jensen et al. (2010), Bayer et al. (2013)], which makes it sensitive to structures that have a preferred orientation. By combining the two properties of the dark-field contrast i.e. sub-pixel resolution and anisotropicity, a new sub-category of imaging methods has recently emerged, namely, Anisotropic X-ray Dark-field (AXDF). AXDF imaging aims to resolve the trade-off between resolution and sample size by revealing information about micron sized oriented scatterers inside macro sized samples. Analogous to attenuation based X-ray imaging, Anisotropic X-ray dark-field imaging has also been developed in both 2D (radiography) [Potdevin et al. (2012), Schaff et al. (2014), Eggl et al. (2015), Prade et al. (2016), Kagias et al. (2016) ,Jud et al. (2016)] and 3D (tomography) [Malecki et al. (2014), Bayer et al. (2014), Vogel et al. (2015), Wieczorek et al. (2016)]. These methods have shown promise for revealing useful information about structures inside industrial and biological samples without the need of directly resolving them. Having been proposed recently, these methods are still in the early stages of development and there is scope of developing this field similar to conventional X-ray imaging for real world applications. One of the major hurdles for the application of AXDF methods is their complex and time consuming acquisition methods. Hence, there is a need to understand the requirements for the simultaneous real and reciprocal space sampling for AXDF radiography and tomography. The goal of this thesis is to design, develop and optimize the acquisition protocols for these methods in order to enable their translation to real-world medical and industrial applications.

1.1 Outline

This thesis is divided into seven chapters classified under three themes (parts).

1. X-ray Imaging Basics

   In the first part, we review the information necessary to understand conventional X-ray Imaging. This consists of a basic understanding of the interaction of X-rays with matter in Chapter 2, followed by a brief explanation of X-ray Computed Tomography in Chapter 3.

2. X-ray Dark-field Imaging

   This section takes the reader two steps deeper into the topics pertinent to this thesis. In Chapter 4, we review the basics of X-ray dark-field contrast mechanism. We provide a brief overview of this fast growing field and provide details of the methods available to acquire this signal and its anisotropic property. We also introduce a 2D AXDF imaging method in this chapter. Chapter 5 is dedicated to the discussion of AXDF tomography. We discuss, in detail, two recently proposed tomographic reconstruction approaches.

3. Acquisition Schemes for Anisotropic X-ray dark-field Imaging Modalities

   This part details the three main contributions of this thesis. All three contributions are aimed at reducing the complexity of the acquisition methods for AXDF imaging. In Chapter 6, we present an industrially compatible approach for performing 2D AXDF imaging. The following two Chapters i.e. Chapters 7 and 8 deal with a much more complex problem, i.e. sampling schemes for AXDF tomography. In Chapter 7, we present an approach to quantify and optimize the existing schemes for the AXDF tomographic imaging modalities. In Chapter 8, we extend the ideas of Chapter 7 and develop a new mechanism to design acquisition schemes for arbitrary setup configurations and sampling requirements of AXDF tomography.

Finally, we present a summary of our results and an outlook for the future of AXDF imaging in Chapter 9.

Part I

X-ray Imaging Basics

Chapter 2

Interaction of X-rays with Matter

The property of X-rays that makes them so important is that they can penetrate matter. However, the interaction of X-rays with matter is more complex than simply passing through it. At an atomic level, X-rays get absorbed by the photoelectric effect, or scattered upon interaction with matter. Additionally, at a macroscopic level, such as an interface between two media, X-rays get refracted or reflected. In reality, these phenomena are just different ways of explaining similar physical interactions at different scales. Since we are concerned with attenuation and scattering based X-ray imaging in this thesis, we will focus the discussion in this chapter to these two phenomena. In section 2.1, we look at X-ray scattering in a medium. In the following section, we look at the macroscopic interaction of X-rays by means of the complex index of refraction.

2.1   X-ray Scattering

The quantity of interest in scattering experiments is the differential scattering cross-section ($d\sigma/d\Omega$) [Glatter and Kratky (1982), Als-Nielsen and McMorrow (2011)]. It is a measure of the efficiency of the scattering process where the incident flux and the detection parameters have been normalized out. In order to calculate this quantity, we begin with elastic scattering from a single electron. In the
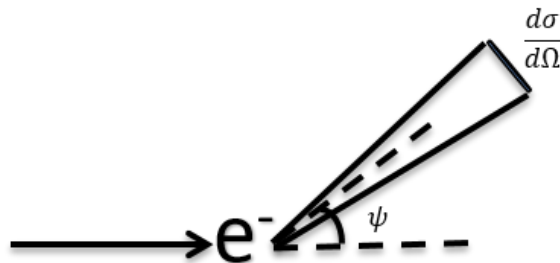
Figure 2.1: Differential cross section of a single electron system at an angle of observation ψ.
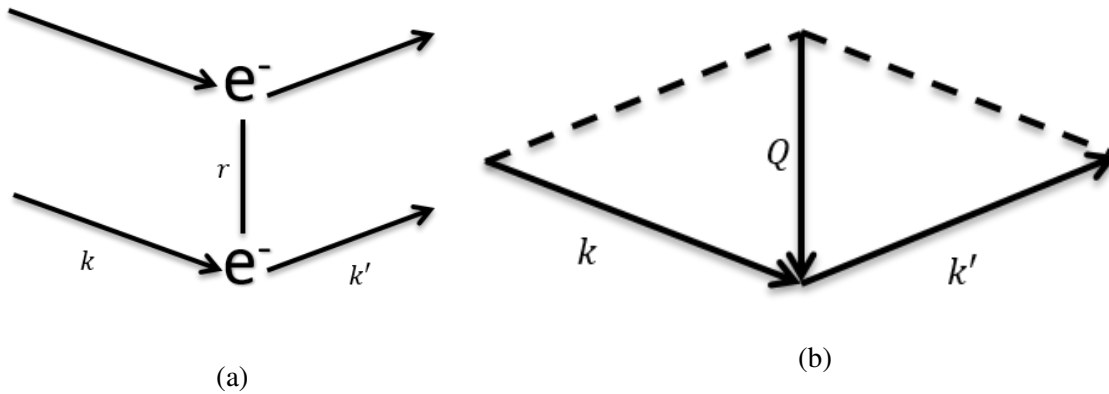
Figure 2.2: (a) Illustration of scattering from a two electron system. (b) Definition of the scattering vector Q.

classical view, an electron, upon illumination with an incident X-ray beam, oscillates and radiates a wave of the same frequency (hence, elastic). Assuming that the polarization of the incident wave is $\hat{\varepsilon}$ and that of the emitted radiation is $\hat{\varepsilon}'$, then the differential cross section for scattering from a single electron is given by:

$$\frac{d\sigma}{d\Omega} = r_0^2 |\langle \hat{\varepsilon}, \hat{\varepsilon}' \rangle|^2, \tag{2.1}$$

where r_0 is the fundamental unit of scattering known as the Thomson scattering length, and $< \cdot, \cdot >$ is the standard inner product. The factor $|\langle \hat{\varepsilon}, \hat{\varepsilon}' \rangle|^2$ is known as the Polarization factor P and depends on the choice of the optical geometry. We have $P = \dfrac{1 + \cos^2 \psi}{2}$ for unpolarized sources, such as the standard laboratory sources, at an angle of observation ψ, as shown in Figure 2.1.

In a real experiment, we are not interested in scattering from a single electron, but from a medium with an electron distribution $\rho(r)$. In order to calculate scattering from a volume element, we need to sum up the scattering from individual electrons while taking the phase difference into account. Let us consider two electrons separated by distance r as shown in Figure 2.2. The incident radiation is described by wave-vector k and the scattered radiation by k'. Since we consider only elastic scattering, $|k| = |k'| = \dfrac{2\pi}{\lambda}$, where λ denotes the wavelength of the incident wave. The phase shift between the waves scattered from the two points can be written as:

$$\triangle\phi(r) = (k - k') \cdot r = Q \cdot r, \tag{2.2}$$

where $Q = (k - k')$ is known as the scattering vector with units of Å^{-1}.

Now, we can calculate the scattering amplitude from a small volume element dr at a distance r from the origin by summing up all secondary waves with the phase shift represented by a factor e^{-iQr}. By replacing the summation with an integration over the whole volume irradiate by the incident beam, we get:

$$F(Q) = \int \rho(r) e^{-iQ \cdot r} dr. \tag{2.3}$$

Mathematically speaking, the above expression is the Fourier transform of the electron density and is known as the atomic form factor. In order to calculate the intensity $I(Q)$ as the absolute square of the amplitude, we multiply F with its complex conjugate F^*,:

$$I(Q) = FF^* = \int\int \rho(r_1)\rho(r_2)e^{-iQ(r_1-r_2)}dr_1dr_2.$$ (2.4)

This is a Fourier transform again in terms of the distance between the pair of points $(r_1 - r_2)$.

We can carry out the double integral in steps. First we sum up all pairs with equal relative distances

$$\gamma(r) = \int \rho(r_1)\rho(r_2)dr$$
$$r = r_1 - r_2 = \text{constant.}$$ (2.5)

$\gamma(r)$ is known as the auto-correlation function at correlation length r and is a point in the so-called reciprocal space or Q space. The second part is the integration over this reciprocal space:

$$I(Q) = \int \gamma(r) \cdot e^{-iQr}dr.$$ (2.6)

This is again the Fourier transform. So, the intensity distribution is determined by the structure of the object as expressed by its auto-correlation function. We can see that the real space and the reciprocal space are related by a Fourier transform related to the factor $Q \cdot r$. The above equation forms the basis of Small Angle X-ray Scattering (SAXS) [Guinier and Fournet (1955),Glatter and Kratky (1982)].

At last, we note that we assumed a free electron in the above consideration while in reality an electron is bound to an atom. Hence, we need to take into account the response of an electron to the incoming field. To do this, we add dispersive coefficients [Als-Nielsen and McMorrow (2011)] to the atomic form factor:

$$F(Q) = f(Q) + f' + if''.$$ (2.7)

f' accounts for the fact that by virtue of the binding energy, the scattering length is reduced. However, it can be ignored for energies greater than the binding energies, which is the case for the rest of this thesis. Due to the dissipation in the system, the response of an electron also has a phase lag with respect to the incoming beam and we added the imaginary term f'' to compensate for it, which is in turn related to the attenuation cross section discussed in the next section [Als-Nielsen and McMorrow (2011)].

2.2   X-ray Attenuation and Phase Shift

In Figure 2.3, we show two linearly polarized electromagnetic waves propagating in the z direction with frequency ω and wave vector k. The first wave travels in vacuum while the second wave travels
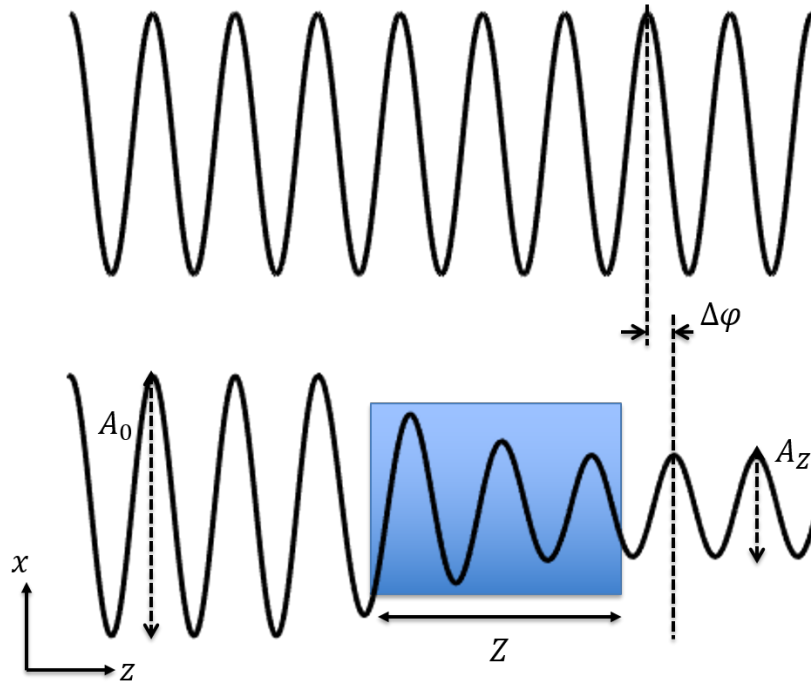
Figure 2.3: X-ray Attenuation and Phase shift while passing through a medium.

through a medium with refractive index n:

$$n = 1 - \delta + i\beta. \tag{2.8}$$

Equation 2.8 describes the two main interactions of the second wave with the medium, namely, phase shift and attenuation. While phase shift is related to the refractive index decrement δ, attenuation is related to the real part β. The second wave after travelling through the material can be written as:

$$\begin{aligned} E(z,t) &= E_0 \, e^{inkz - \omega t}, \\ &= E_0 \, e^{-\beta kz} \, e^{i\delta kz - \omega t}. \end{aligned} \tag{2.9}$$

2.2.1   Attenuation

Attenuation of the incoming beam refers to the decrease in the mean intensity. It is defined as:

$$\frac{I(z)}{I_0} = \frac{|E(z)|^2}{|E_0|^2} = e^{-2k\beta z}. \tag{2.10}$$

We can rewrite the above equation to obtain the Beer Lambert law:

$$I = I_0 e^{-\mu z}, \tag{2.11}$$

where $\mu = 2k\beta$ is the linear attenuation coefficient. μ describes the efficiency of X-ray absorption by an element. The beer lambert law can be generalized to a medium consisting of several materials by using an integral over infinitesimal volumes of homogeneous attenuation coefficients, resulting in:

$$\log\left(\frac{I}{I_0}\right) = -\int_0^z \mu(z)dz. \tag{2.12}$$

μ is related to the absorption cross-section σ and the atomic number density ρ_{at} by:

$$\mu = \rho_{at}\sigma. \tag{2.13}$$

The absorption cross-section is proportional to the atomic number approximately as Z^4, which is the reason that makes X-rays useful for distinguishing between different elements inside objects and forms the basis for X-ray Computed Tomography, discussed in the next chapter.

2.2.2 Phase Shift

The phase shift $\triangle\phi$ of the wave after passing through a material of thickness z with respect to the undisturbed wave (in the absence of attenuation) is given by:

$$\triangle\phi(z) = k\delta z. \tag{2.14}$$

This leads to the refraction of the beam in a direction perpendicular to its propagation and is given by [Paganin (2006)]:

$$\alpha = \frac{\lambda}{2\pi}\frac{d\phi}{dx}, \tag{2.15}$$

where λ is the wavelength of the beam. Similar to attenuation, we can extend this to the generic case in a homogeneous material:

$$\triangle\phi = -\int_0^z k\delta(z)dz. \tag{2.16}$$

This phenomena forms the basis for Phase Contrast X-ray Imaging. We will discuss this contrast mechanism very briefly in Chapter 4.

Chapter 3

X-ray Computed Tomography

We saw in section 2.2.1 that X-ray absorption is one of the major modes of interaction of X-rays with matter. This is also the easiest to detect and quantify and was, infact, the phenomenon that led to the discovery of X-rays. Ever since its discovery in 1895, X-ray absorption has been used in a plethora of fields from medicine, material science and security. A single X-ray image is described by the Beer Lambert law (Eq. 2.11) as explained in section 2.2.1. However, for most applications, a 2D projection is not enough to obtain the desired information and we need to reconstruct the absorption coefficient in the 3D volume. This process of reconstructing the 3D information about the inside structure of a specimen using X-rays is known as X-ray Computed Tomography (CT) [Cormack (1963), Cormack (1964)]. In this chapter, we review the basics of CT with respect to the mathematical reconstruction approach and the acquisition methodology.

3.1 Mathematical Basis of CT Reconstruction

3.1.1 Radon Transform

The basics of an X-ray projection were described by the Radon Transform [Radon (1986)], long before CT was even conceptualized. Let us define the cross-section of a function as $f(x,y)$. Then the projection of f taken from an arbitrary direction $\theta \in [0,\pi)$ is defined as:

$$[Rf](s,\theta) = \int_{-\infty}^{\infty} f(x,y)du, \tag{3.1}$$

where (s,u) is the coordinates of the point (x,y) in the reference frame rotated by the angle θ (Figure 3.1):

$$
\begin{aligned}
s &= x\cos\theta + y\sin\theta, \\
u &= -x\sin\theta + y\cos\theta.
\end{aligned}
\tag{3.2}
$$
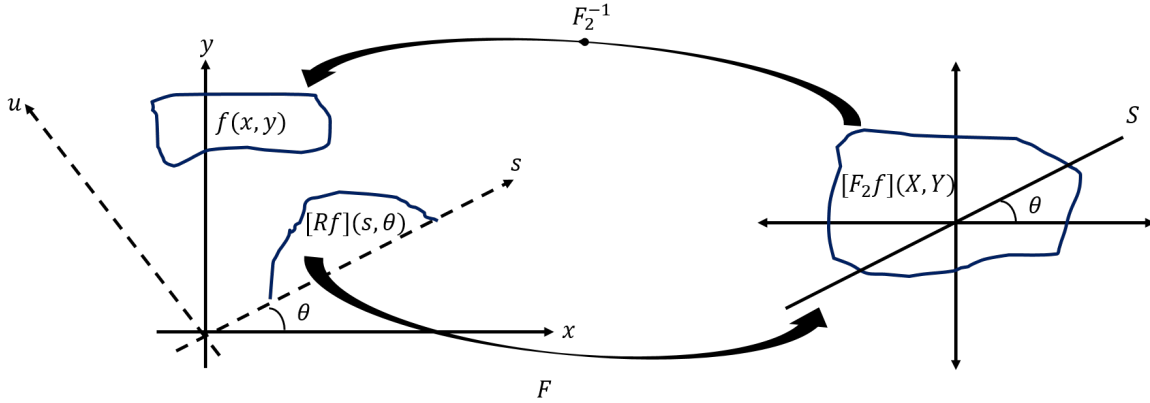
Figure 3.1: Illustration of the Fourier Slice Theorem (Eq. 3.7).

Eq. 3.1 is called the radon transform and gives the projection of any 2D function onto a line at an angle θ. This transform provides a very convenient mathematical description of the image formation process in X-ray imaging. For 3D, the direct interpretation of the radon transform would imply integrals over hyper-planes, which is not the case for X-ray imaging, therefore, the radon transform has been adapted for the 3D case of X-ray imaging as the X-ray Transform [Natterer (2001)]. In this chapter, we limit our discussion to the 2D case. The Radon Transform is related to the well-known fourier transform through the Fourier slice theorem.

3.1.2   Fourier Slice Theorem

The Fourier Slice Theorem [Banhart (2008)], or the Central Slice Theorem is one of the most fundamental concepts of CT reconstruction. The theorem states that the fourier transform of a projection, is a slice in the fourier domain of the function. In order to state this explicitly, lets first revisit the one and two dimensional fourier transform and its inverse. $[Fg](S, \theta)$ is the one dimensional fourier transform of $g(s, \theta)$ if:

$$[Fg](S, \theta) = \int_{-\infty}^{\infty} g(s, \theta) e^{-2\pi i s S} ds, \qquad (3.3)$$

and its inverse,

$$[F^{-1}g](s, \theta) = \int_{-\infty}^{\infty} g(S, \theta) e^{2\pi i s S} dS. \qquad (3.4)$$

$[F_2 f](X, Y)$ is the 2-dimensional fourier transform of $f(x, y)$ if:

$$[F_2 f](X, Y) = \int_{-\infty}^{\infty} \int_{-\infty}^{\infty} f(x, y) e^{-2\pi i (xX + yY)} dx dy. \qquad (3.5)$$

and its inverse in cartesian and polar coordinates, respectively, is:

$$[F_2^{-1}f](x,y) = \int_{-\infty}^{\infty}\int_{-\infty}^{\infty} f(x,y)e^{2\pi i(xX+yY)}dXdY,$$

$$= \int_0^{\pi}\int_{-\infty}^{\infty} f(S\cos\theta, S\sin\theta)e^{2\pi i(x\cos\theta+y\sin\theta)S}|S|dSd\theta. \tag{3.6}$$

The fourier slice theorem states that for all $S \in \mathbb{R}$ and $\theta \in [0,\pi)$.

$$[F_2f](S\cos\theta, S\sin\theta) = [FRf](S,\theta). \tag{3.7}$$

The theorem is illustrated in Figure 3.1. For a detailed proof, we direct the readers to Banhart (2008).

Using Equation 3.7, and taking projections $[Rf](s,\theta)$ over the angular range $\theta \in [0,\pi)$, we can sample the 2D fourier space of the function, as shown in Figure 3.2. Now that we have measured F_2f, we can use the inverse 2D fourier transform to recover the function f. While this is possible in theory, recovering the function $f(x,y)$ via the 2D inverse fourier transform (Eq. 3.6) involves interpolation of the tiled fourier grid, which is non-trivial and leads to inaccurate reconstruction. Methods that use this concept to perform reconstruction exist [Francesco and da Silva (2004)], however, they are not commonly used. Two of the most commonly used methods for CT reconstruction are the Filtered back Projection (FBP) and the so-called iterative methods [Natterer (2001)]. We discuss these two methods briefly in the next section.

3.2   Reconstruction

The problem of CT reconstruction is to invert the radon transform, i.e. given a function $g(s,\theta)$, find a function $f(x,y)$ such that:

$$[Rf](s,\theta) = g(s,\theta) \text{ for all } -\infty < s < \infty, \ \theta \in [0,\pi). \tag{3.8}$$

Below, we present an analytical approach to solving this problem.

3.2.1   Filtered Back Projection

Let us define the backprojection operator:

$$[Bg](x,y) = \int_0^{\pi} g(x\cos\theta + y\sin\theta, \theta)d\theta, \tag{3.9}$$

for all point (x,y) in the plane. It is easy to see that $BRf \neq f$ i.e. backprojection operator is not the inverse of the radon transform. Using this operator, filtered backprojection [Banhart (2008)] is defined as:

$$f = B(F^{-1}(|S|FRf). \tag{3.10}$$
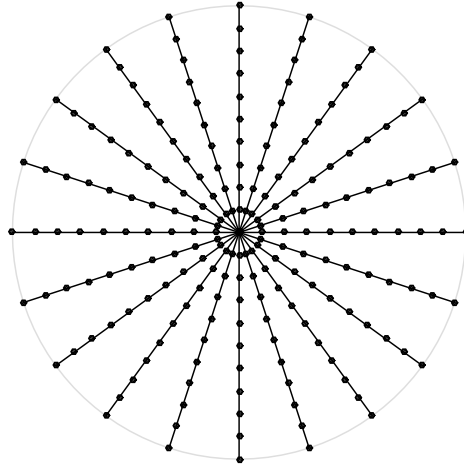
Figure 3.2: Tiling of the fourier space obtained by acquiring projections $g(s, \theta)$, $\theta \in [0, \pi)$ and using the Fourier slice theorem (Eq. 3.7).

$|S|$ is a high pass filter that is multiplied to FRf in order to compensate for the oversampling of the zero frequency as can be seen in Figure 3.2. The reconstruction is performed in two steps:

1. Filtering in fourier domain:

$$g'(s, \theta) = [F^{-1}|S|FRf](s, \theta) \tag{3.11}$$

2. Backprojection in real domain:

$$f(x, y) = [Bg'](x, y). \tag{3.12}$$

3.2.2 Iterative Reconstruction

The FBP algorithm presented above provides an analytical approach to reconstruct the image from a series of projections. However, it suffers from several limitations such as the requirement of a homogeneous distribution of projections over $180°$. Moreover, it does not allow any possibility to incorporate prior information about the sample. Therefore, there is continuous effort to develop novel reconstruction methods with the aim of reducing the dose transmitted to the patient while improving the image quality for diagnosis. We explain the basics of these methods below.

Let us consider a discretized 5×5 two dimensional cross section shown in Figure 3.3. Let us define a ray i passing through the image and recorded on a detector pixel as shown. The value recorded at the pixel can be written as a weighted sum of the contributions from all the pixels intercepted by the ray:

$$b_i = \sum_j a_{ij} x_j, \tag{3.13}$$
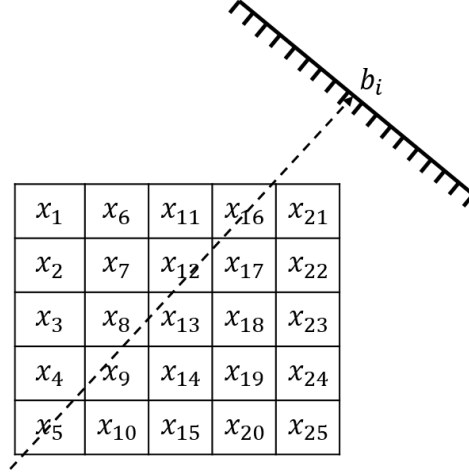
Figure 3.3: Illustration of ray tracing for setting up the linear system for iterative reconstruction (Eq. 3.13).

where a_{ij} is a weight representing the contribution of the jth pixel to the ith ray. Several approaches for calculating the weights are available, most common being the line model, strip model and Joseph's model [Natterer (2001), Joseph (1982)]. By using one of the ray tracing approaches for all rays, we obtain a linear system of equations:

$$Px = b, \tag{3.14}$$

where P is known as the system matrix. It is a 2D array consisting of one column for every pixel j and one row for the ray i. Size of P is typically too large to store in the system memory, hence, it is not possible to solve Eq. 3.14 by factorization. Moreover, the measured data b is characterized by noise owing to the detector electronics, $b = b^* + \text{noise}$. Therefore, we resort to numerical optimization methods to find a least squares solution to the minimization problem $\min_x \|Px - b\|_2^2$.

3.3   Acquisition Schemes in CT

So far, we presented the methods of CT reconstruction. In this section, we deal with another important aspect of CT i.e. the acquisition method. Although we do not directly use the fourier slice theorem for reconstruction, it provides some important conclusions for designing CT acquisition schemes. An important consequence of the Fourier slice theorem is that we can sample the fourier space of the function $f(x,y)$ by obtaining the slices $[FRf](S,\theta)$. Such a frequency domain tiling can be obtained by measuring the projections $[Rf](s,\theta)$ for equally spaced $\theta \in [0,\pi)$. An example of such a tiling is shown in Figure 3.2. Another important criteria is to determine the number of projections required for a good reconstruction. We can again use the fourier slice theorem in combination with the Nyquist Shannon theorem to estimate this number, as is explained below.

Note that in a real experiment, we use the discrete versions of equations 3.11 and 3.12. Lets say that we have N projections and M lines in each projection where M is odd. This implies that the

projection $g = Rf$ of f is sampled as:

$$g(s_m, \theta_n) = g(m \triangle s, n \triangle \theta),$$
$$m = (M-1)/2, \cdots, (M-1)/2, \qquad (3.15)$$
$$n = 0, 1, \cdots, N-1,$$

where $\triangle s > 0$ denotes the sampling of s and $\triangle \theta = \pi/N$. Now, consider that we only reconstruct a band limited version of f by integrating over $-W < s < W$ instead of the infinite integral in Eq. 3.6. Using the Shannon sampling theorem, we know that in order to recover the W bandlimited version of f, we need:

$$\triangle s \leq \frac{1}{2W}. \qquad (3.16)$$

In a real experiment, this boils down to a simple rule of thumb that the number of projections N should be atleast $\pi/2$ times the maximum width of the sample.

3.3.1   Spherical Representation of Acquisition Schemes

In the previous section, we derived the most important criteria for a CT acquisition scheme i.e. we need to measure projections spread uniformly over a full circle. Using this, let us define a standard CT acquisition scheme consisting of N acquisition poses as:

$$X(\Phi_1, \Phi_2, N) := \left\{ x = \phi; \ \phi \in \left\{ \Phi_1, \frac{\Phi_2 - \Phi_1}{N}, \ldots, \Phi_2 - \frac{\Phi_2 - \Phi_1}{N} \right\}; N \in \mathbb{N} \right\}, \qquad (3.17)$$

where Φ_1 and Φ_2 are angles in degrees. Here, we consider an acquisition pose $x := (\phi)$ that defines the orientation of the sample with respect to the setup coordinates in 3D space. A conventional CT system usually provides only one degree of freedom to the sample stage (rotation around the y axis), hence, one angle is usually used to describe the sample rotation. A standard CT acquisition trajectory can be written in the above notation as $X(0°, 180°, N)$, where N is given by the criteria explained in the previous section.

In this section, we introduce a spherical representation of acquisition schemes which will be heavily used throughout this thesis. In this representation, we assume the sample to be stationary at the centre of the sphere and mark the trajectory of the optical axis with blue points for a given acquisition scheme. This trajectory for an acquisition scheme X consists of the points $\pm t(x) \ \forall \ x \in X$. $t(x)$ for a pose x is given by:

$$t(x) = R(x) \cdot T, \qquad (3.18)$$
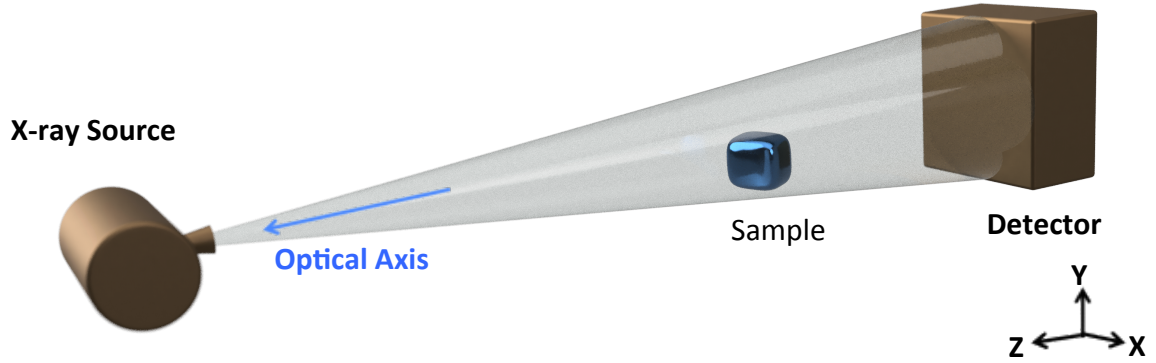
Figure 3.4: Schematic of a setup used for Computed Tomography. The z axis is the tomographic axis and the sample is rotated around the y axis.

where $T \in \mathbb{S}^2$ is the direction of beam propagation shown in Figure 3.4, and $R(x)$ is the euler rotation matrix for rotation of the sample by an angle ϕ about the y axis given by:

$$R_y(\phi) = \begin{bmatrix} \cos\phi & 0 & \sin\phi \\ 0 & 1 & 0 \\ -\sin\phi & 0 & \cos\phi \end{bmatrix}. \tag{3.19}$$

Figure 3.5(a-c) shows the representation for the schemes $X(0°, 180°, 20)$, $X(45°, 180°, 20)$ and $X(0°, 90°, 20)$, respectively.

3.3.2 Null Space Analysis

The spherical representation of acquisition schemes provides a nice tool to visualize the different trajectories. However, we need a method to quantify the effectiveness of these schemes in order to develop dose efficient and task specific schemes. One way to analyze the acquisition schemes and their effect on the reconstruction is to analyze the nature of the full system matrix P.

An important aspect of a linear operator, such as P in the CT model described above, is the null space (or kernel) of P. It is defined as $\ker(P) := \{v \mid Pv = 0\}$ and is of special interest as for $w \notin \ker(P)$ and any $v \in \ker(P)$, the measurement does not change under addition i.e.,

$$Pw = P(w+v). \tag{3.20}$$

The kernel provides a tool to analyze the matrix P and gives information about the uncertainty of a computed reconstruction. While it is well known that incomplete data leads to a larger nullspace, it is of special interest how elements of this space look like as they provide a relative insight of which regions are likely to be affected more/less.

Standard methods such as singular value decomposition (SVD) are typically used for computing the null space of such matrices. However, these methods rely on the full representation of the matrix
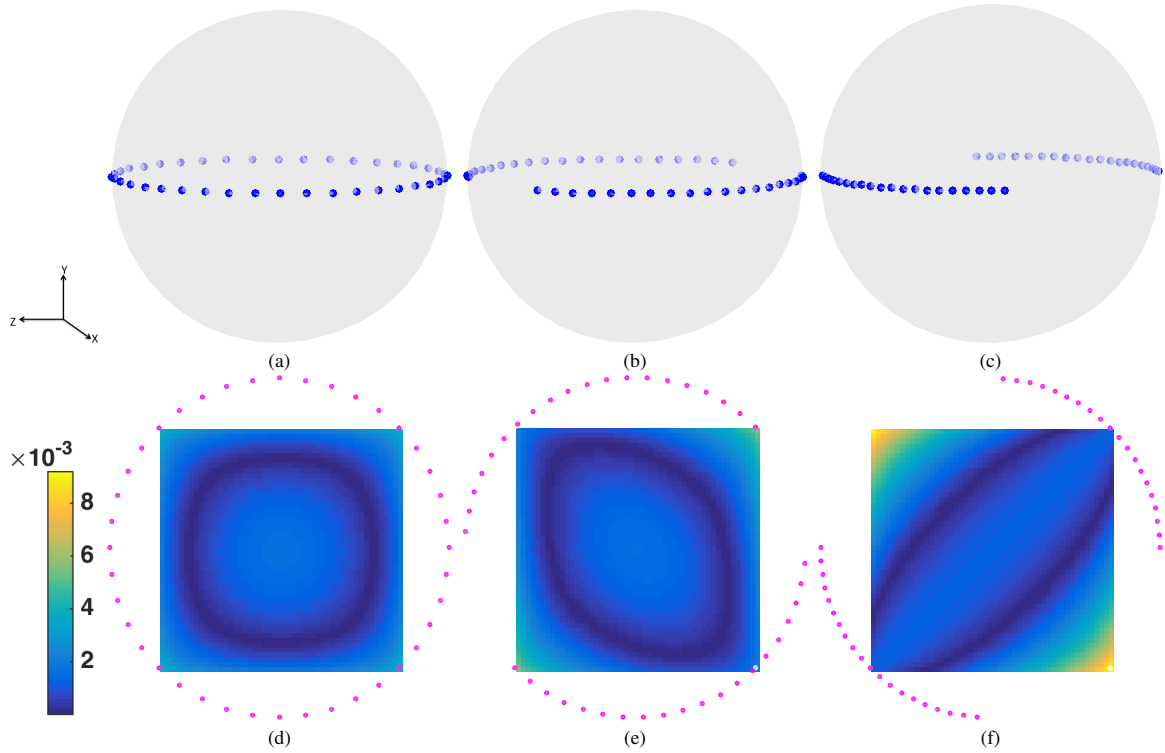
Figure 3.5: Spherical representation of CT schemes (a) $X(0°, 180°, 20)$ (b) $X(45°, 180°, 20)$ (c) $X(0°, 90°, 20)$. (d-f) Null space of the schemes in top row.

and we already saw in section 3.2.2 that P is usually too big to store in system memory. Therefore, we calculate one vector of the null space $v \in \ker(P)$ by solving $Pv = 0$ iteratively using an initial non-zero guess for v. In the simplest case, we can use a uniform initial guess as:

$$v = \begin{pmatrix} 0.01 \\ \vdots \\ 0.01 \end{pmatrix}.$$ (3.21)

This initial guess is especially useful for visualizing the effect of missing angles clearly. We use this guess to calculate the null space of the three schemes shown in Figure 3.5. We set the reconstruction volume size to $50 \times 50 \times 50$, the detector size to 100×100 and use a parallel geometry assumption.

We show the component of null space calculated using this approach and a single iteration of conjugate gradient solver in Figure 3.5. Spherical representation of the acquisition schemes can be seen in the top row along with the null space component at the bottom. The images in the bottom row show the null space averaged over all $x - z$ planes. We can see that missing angle lead to a larger null space component corresponding to the missing information. This effect can also be understood using Figure 3.2 i.e. the frequencies corresponding to the missing projections are missing in the fourier domain, leading to loss of information in the orthogonal direction.

Part II

X-ray Dark-field Imaging

Chapter 4

X-ray Dark-Field

X-ray dark-field (XDF) is a relatively new contrast mechanism for X-rays. The name dark-field is borrowed from light and electron microscopy [Gage (1920)], where it refers to the signal that is observed when the main beam is blocked, hence the term "dark-field". The signal measured as the dark-field contrast originates from small and ultra small angle scattering of X-rays [Yashiro et al. (2010), Lynch et al. (2011), Strobl (2014),Prade et al. (2015)]. However, instead of blocking the source of light, we use optical elements to indirectly separate the absorbed, refracted and scattered part of the radiation [Pfeiffer et al. (2008)]. In this chapter, we outline the concepts and mechanism employed to obtain X-ray dark-field signal in a laboratory setup.

In section 4.1, we review the fundamental principles behind XDF and outline the setup required to measure this contrast mechanism. Next, we review the approaches available to measure the dark-field contrast, and present details of the two methods used in this thesis. We briefly discuss the relation between XDF and conventional X-ray scattering methods in section 4.4. Finally, we introduce Anisotropic X-ray Dark-field Imaging in section 4.5.

4.1   X-ray Grating Interferometry

The basic principle of XGI was discovered many years ago and is known as the Talbot effect [H.F. (1836)]. The Talbot effect sates that a periodic wavefront will repeat itself at certain fixed distances [Jahns and Lohmann (1979)]:

$$d_T = \frac{mp^2}{\lambda}, \text{ m is even} \tag{4.1}$$

where p is the periodicity of the wavefront and λ is the wavelength. One specific case of this effect is observed when a transmission grating [Loewen and Popov (1997)] is placed under spatially coherent illumination. Self-images of the grating are generated at fixed distances given by the expression above.

In case of structures known as Talbot Array Illuminators (TAILs) [Lohmann and Thomas (1990), Hamam (1997), Klaus and Arimoto (1997), Suleski (1997)], we observe the fractional Talbot effect. A
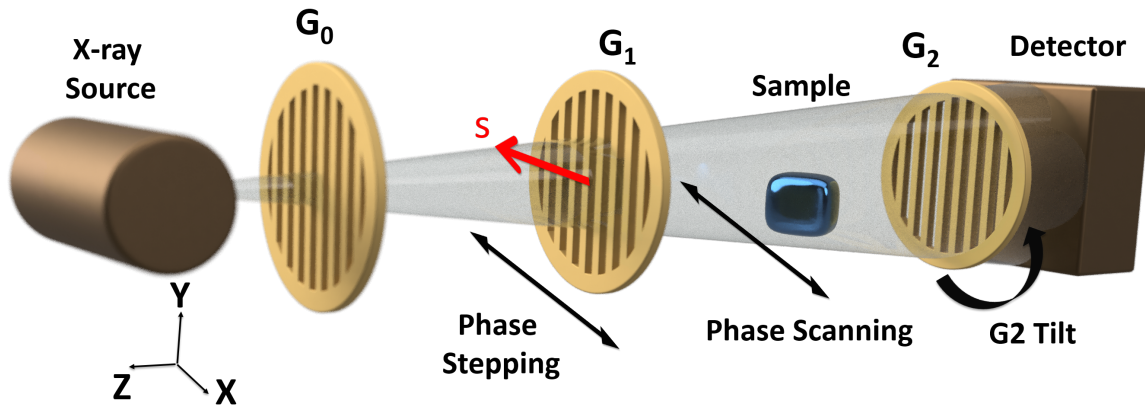
Figure 4.1: Schematic of an X-ray Grating Interferometry (XGI) Setup.

special case of a TAIL is the binary phase grating. It is a periodic structure with regions of thickness w that shift the incoming wavefront by a phase $0 - \pi$. The phase shifted wavefront then interferes with the un-shifted wavefront to create bands of intensity patterns behind the phase grating at fractional talbot distances given by:

$$z = \frac{(m + 1/2)p^2}{\lambda}, \text{ m is even.} \tag{4.2}$$

This phenomena has been studied extensively for visible light [Testorf and neda (1996)]. The fractional Talbot effect was demonstrated for X-rays for the first time by Cloetens et al. (1997).

Using this effect, Momose et al. (2003) introduced the X-ray Grating Interferometer (XGI) by placing a transmission grating at a fractional talbot distance. By placing a transmission grating of the same period as the self image of the phase grating at the position of the grating, Momose et al. (2003) observed moire fringes [Yokozeki (1982)] in the FOV. Moire fringes are equivalent to imprinting a pattern on the wavefront and by observing the distortion of this pattern by a sample, we can reconstruct the real and imaginary parts of the refractive index. Momose et al. (2003) used this principle to obtain differential phase contrast images using an XGI setup, which was a major breakthrough in the available phase contrast imaging methods [Momose (2005)] at that time. While this was a new way of phase contrast imaging, X-ray talbot interferometry still did not solve the problem faced by other phase contrast imaging methods, which is the requirement of a coherent and monochromatic X-ray source.

This limitation was overcome in 2006 by the introduction of a third grating in a XGI setup. Pfeiffer et al. (2006) demonstrated the first XGI setup with a lab X-ray source by using an additional transmission grating close to the source, known as the source grating. The source grating acts as a beam splitter and splits an incoherent laboratory source into several individually coherent but mutually coherent sources. The important condition that is to be met is the fact that the period of the source grating should be chosen such that the position of the highest intensity matches with the position of

the absorption grating. When the three gratings are placed in the optimal configuration, we can obtain differential phase-contrast with a cheap laboratory X-ray source.

In a following publication, Pfeiffer et al. (2008) reported the availability of a third type of contrast modality in an XGI setup, the so-called dark-field contrast. Following these developments, XGI gained popularity as an imaging modality which for the first time extended X-ray imaging beyond the absorption contrast. Nowadays, XGI is an active field of research and several advancements have been made in increasing the sensitivity, resolution and image quality of this technique [Bech et al. (2010), Scholkmann et al. (2014), Birnbacher et al. (2016), Modregger et al. (2011)]. In the next section, we discuss the data processing steps required to obtain the differential phase and dark-field contrast in an XGI setup.

4.2   Three Contrasts

Figure 4.1 shows the schematic of a typical XGI setup using a lab source. In addition to the source and the detector, the setup consists of three gratings as discussed above. The first grating, G0 is an absorption grating that splits an incoherent X-ray wavefront into a number of individually coherent but mutually incoherent beamlets. The second grating G1 is a phase grating that imprints the talbot pattern on the incoming wavefront. The third grating G2, placed right in front of the detector is an absorption grating used to analyze the interference pattern.

As explained in the previous section, when we place G2 at one of the fractional Talbot distances, we observe a moire fringe pattern. This patten can be approximated as a sinusoid of period 2π [Weitkamp et al. (2005), Bech (2009)] and can be described by the first two terms of a Taylor series expansion as follows:

$$I_k = a_0 + a_1 \cos\left(\frac{2\pi}{n}k - \phi\right), \tag{4.3}$$

where $k = 1, 2, \cdots, n$ are the sampling points. The three parameters a_0, ϕ and a_1 represent the mean intensity, phase and the peak intensity of the moire pattern, respectively. In addition, we define a quantity, visibility (V), as:

$$V = \frac{a_1}{a_0}. \tag{4.4}$$

By calculating the three parameters, with and without a sample in the beam, we can obtain three contrast modalities, namely the conventional attenuation contrast (A), differential phase contrast (DPC) and the dark-field contrast (DF) as illustrated in Figure 4.2. The three quantities are defined as:

$$A = \frac{a_0^s}{a_0^r},$$
$$DPC = \phi^s - \phi^r, \tag{4.5}$$
$$DF = \frac{V^s}{V^r},$$
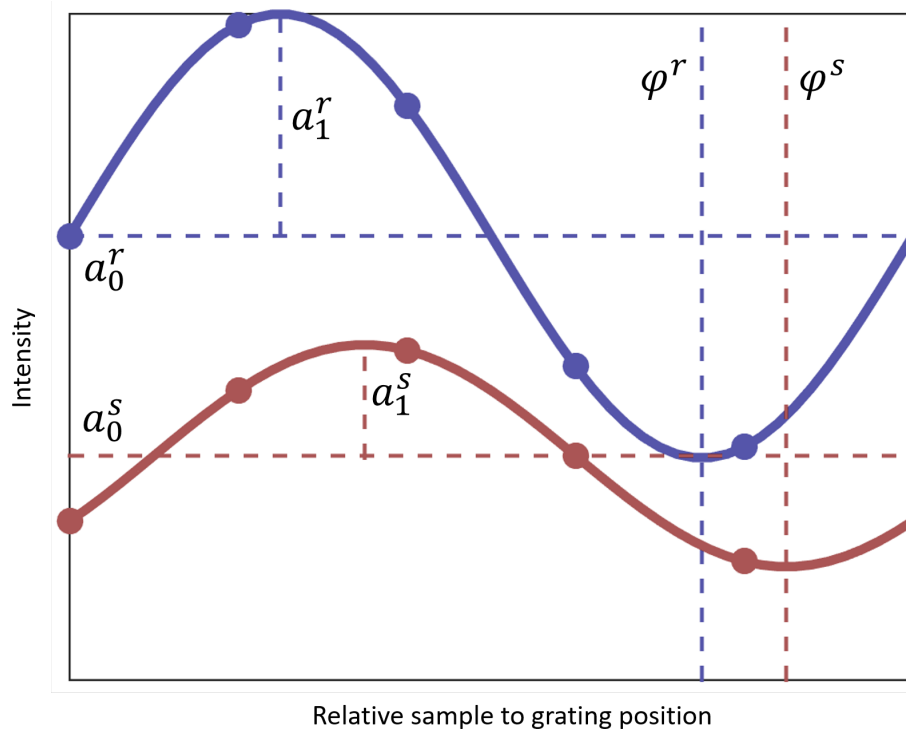
Figure 4.2: The intensity (also known as, stepping) curve, with (red) and without (blue), the sample.

where the superscript s refers to the parameter calculated with the sample in the beam and the superscript r refers to the parameters without the sample. A least squares fitting approach is used to extract the parameters in all the data presented in this thesis.

The three contrast modes reveal information about the three modes of interaction of X-ray with the sample, namely absorption, refraction and scattering (Chapter 2). As evident in Figure 4.2 and 4.3, the dip in the mean intensity is caused due to the absorption of a fraction of the incoming flux, the shift in the position of the peak is caused by refraction from macro-sized interfaces while scattering from micron sized structures leads to a loss of visibility. These three contrast mechanisms are illustrated in Figure 4.3, alongwith the corresponding images of a Cherry. We can see in Figure 4.3 that attenuation contrast does not reveal any details of the inside of the cherry since the difference in the attenuation coefficient between the cherry and the seed is not significant for the X-ray energy used. On the other hand, the differential phase contrast is able to delineate nicely the boundary of the seed from the inside of the cherry. Most importantly, the dark-field contrast reveals fibrillated structures which are not visible in either of the other two modalities. In conclusion, the three contrast mechanisms, obtained simultaneously, provide complementary information about the sample.

(a) Absorption Contrast

(b) Differential Phase Contrast

(c) Dark-field Contrast
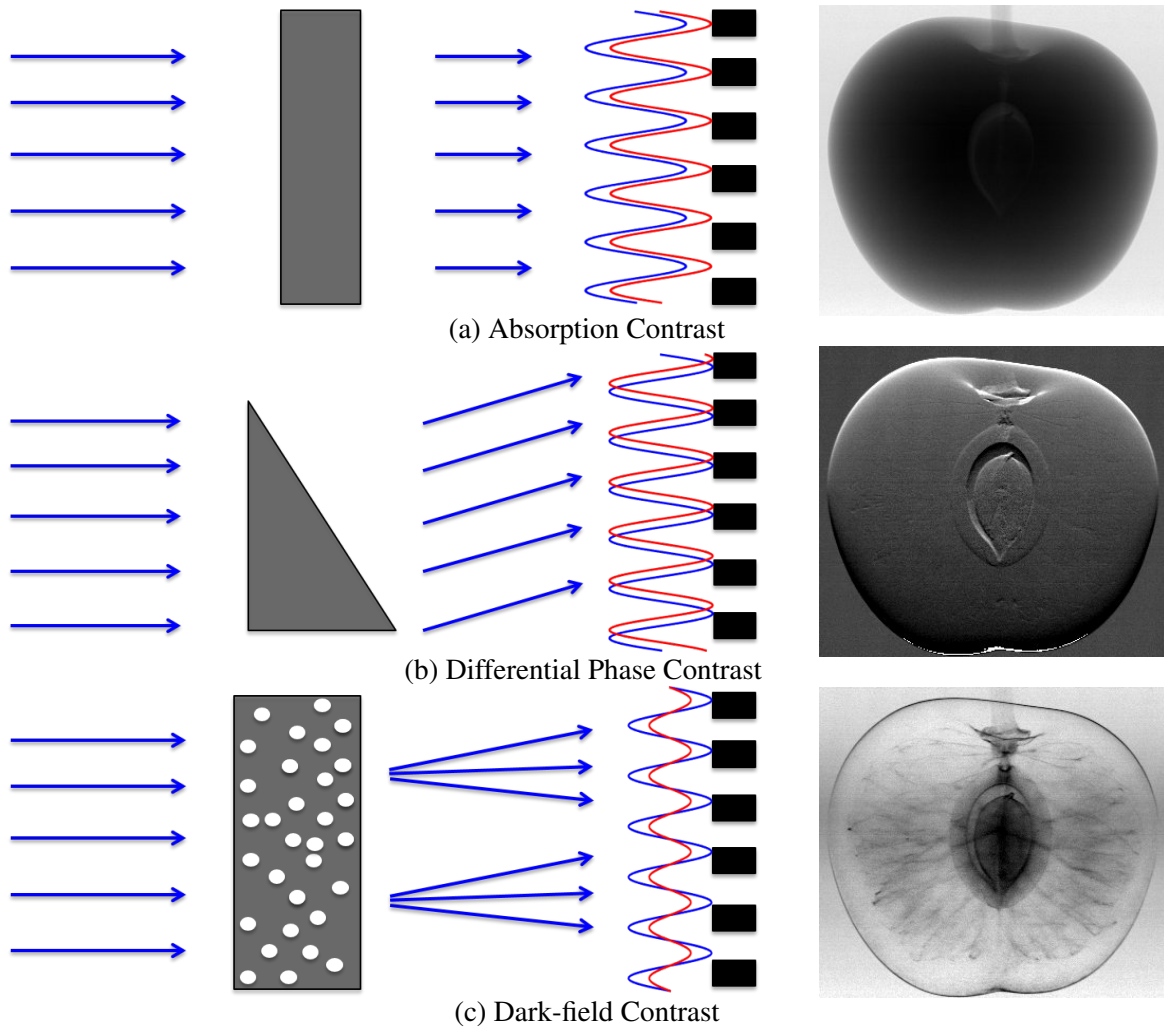
Figure 4.3: Schematic showing the three contrast mechanisms obtained in an XGI setup and the corresponding images of a cherry.

4.3 Acquisition and Image Extraction

The first step to obtaining the three contrasts in an XGI setup shown in Figure 4.1 is to sample the intensity curve (Eq. 4.3). Below, we briefly discuss the approaches available to do this.

1. High resolution detector:

   With the availability of a high resolution detector, the moire fringes can be directly resolved and we can sample the intensity curve by binning the measured moire pattern into coarser resolution or using fourier analysis [Takeda et al. (1982)]. This allows for a single shot measurement of the three contrast mechanisms and is, hence, suitable for 4D applications as demonstrated by Yashiro et al. (2017). However, it is limited by the requirement of high flux and is implemented, almost exclusively, at synchrotron X-ray sources. Moreover, limited field-of-view poses significant limitation to the practical applications of this approach.
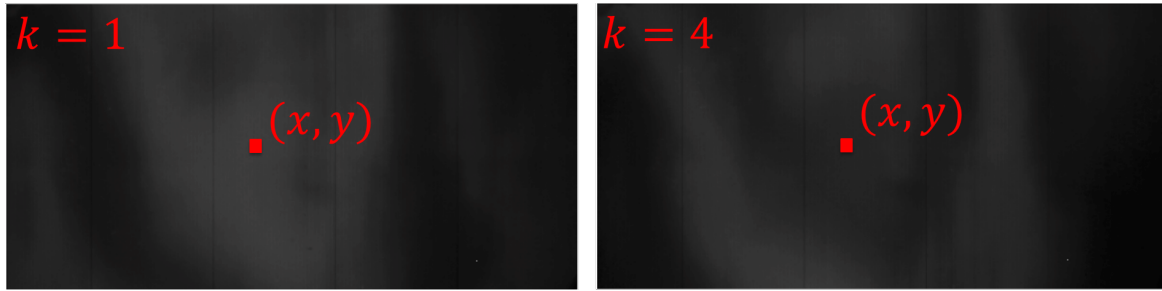
Figure 4.4: A typical field of view for a nicely aligned grating interferometry system with 3 gratings. A point (x, y) on the sample *sees* different points (k in Eq. 4.3) of the intensity curve as one of the gratings is stepped to different positions over one period.

2. Phase Stepping:

   A more practical approach to sample the intensity curve is to step one of the gratings to several positions over one period. This approach approach was used by Momose et al. (2003) and still remains the most commonly used approach, hence, the curve in Figure 4.2 is often known as the stepping curve. This approach involves a step and shoot mechanism and, therefore. suffers from excessive dose and poor temporal resolution.

3. Phase Scanning:

   The phase stepping approach suffers from poor temporal resolution and lack of repeatability in the process of grating stepping. Hence, an alternate approach was proposed for the first time by Kottler et al. (2007). In this approach, the optical system is static, instead the linear position of the sample is changed with respect to the moire fringes in order to sample the stepping curve. A slit-scanning approach [Koehler et al. (2015)] also uses the same principle, with the difference that the gratings are moved (not stepped) with respect to a static sample. It is currently the most investigated technique for medical applications.

4. Electro-mechanical deflection of the X-ray focal spot:

   This approach was introduced recently where in the focal spot in a laboratory X-ray source is deflected to induce a relative shift between the point being investigated and the moire pattern. Miao et al. (2014) demonstrated that this results in the same effect as moving one of the grating or the sample.

In this thesis, we only use the phase stepping and phase scanning methods to obtain dark-field images. We elaborate on these two approaches below.

4.3.1   Phase Stepping

The basic principle of this approach is to change the phase of the moire pattern seen by a given point (x, y) in the sample. This is done by keeping the sample stationary and moving one of the grating in
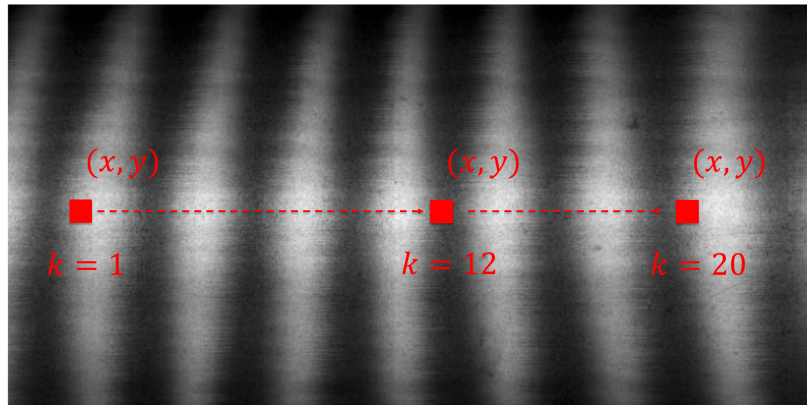
Figure 4.5: A typical field of view for the phase scanning method. A point (x,y) on the sample *sees* different points (k in Eq. 4.3) of the intensity curve as it moves linearly through the FOV.

steps, hence, it is often known as the phase stepping method [Creath (1988)]. First, we try to align the gratings perfectly so as to ensure that there are no moire fringes in the FOV. An example of FOV in an aligned setup is shown in Figure 4.4. In principle, the method also works with moire fringes, however, then we have an even lesser tolerance for imperfection in grating stepping. One of the three gratings (most commonly G1) is mounted on a precision stepper motor and stepped to n position over one period of the respective grating. The grating positions are given by $x_g = \dfrac{d}{n}$ where d is the period of the grating that is being stepped. For every pixel (x,y) on the detector plane, we obtain the intensity I_k corresponding to the kth grating position. We repeat this process for n positions of the grating using a step-and-shoot approach. By using this stepping approach, we obtain k points on the Intensity curve and calculate the parameters a_0^s, a_1^s, ϕ^s and a_0^r, a_1^r, ϕ^r, with and without the sample, respectively. We illustrate this process in Figure 4.4, where the pixel (x,y) on the sample remains stationary while the phase of the moire pattern at this point is changed by stepping the grating G1. We use this approach throughout Chapters 7 and 8.

4.3.2 Phase Scanning

The phase stepping approach suffers from serious drawbacks owing to stringent requirements of stability and repeatability during the stepping process. Although, algorithmic improvements presented recently [Teuffenbach et al. (2017)] try to overcome this limitation, it still remains one of the major concerns to the practical application of such systems. In order to obviate the need of grating stepping, Kottler et al. (2007) introduced a phase scanning approach. In this approach, the intensity modulation in every pixel is recorded by moving the sample linearly through the detector field-of-view (FOV) that encodes spatially varying phase information in the form of intensity i.e. moire fringes. Several works [Arboleda et al. (2014), Marschner et al. (2016)] using this approach have been reported in recent years. All of them require a very precise and uniform arrangement of moire fringes in the FOV, or in other words, assume a well-defined and homogeneous grating structure. However, owing to
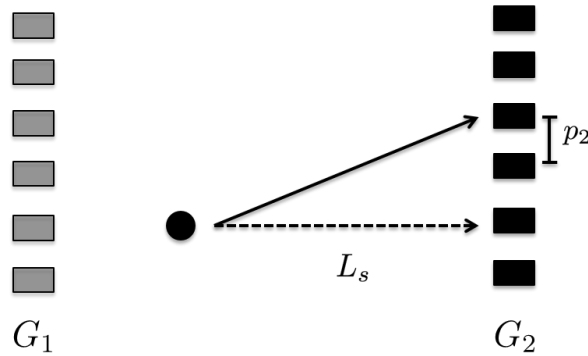
Figure 4.6: Relation between dark-field signal and setup parameters.

the imperfections in the fabrication process, it is almost impossible to guarantee homogeneity of the grating structure. To overcome this limitation, Bachche et al. (2017) recently proposed a robust phase scanning method that works with irregular and varying moire patterns. We illustrate this approach in Figure 4.5, where the intensity curve (different values of k in Eq. 4.3) is sampled by moving the pixel (x,y) across the FOV with moire fringes. We use this method in Chapter 6.

4.4 Origin of the Dark-field Signal

So far, we learnt that an XGI setup provides a complimentary contrast, namely, the dark-field contrast. We saw in the last section, that this contrast modality is obtained by indirectly separating X-ray scattering from absorption and refraction. Owing to this reason, the main contribution to the dark-field contrast comes from small and ultra small angle scattering of X-rays from micron and sub-micron sized structures. Obviously, the same quantity is measured directly in other X-ray modalities, for example, SAXS where we block the main beam and directly measure the scattered part of radiation. In these techniques, we measure the entire diffraction pattern at one point and use raster scanning approach to perform SAXS imaging [Guinier and Fournet (1955), Schaff et al. (2015)]. XDF provides the unique ability to obtain scattering information with the spatial resolution of an imaging system.

However, there is a need to establish the relationship between these two methods in order to better understand the origin of the dark-field contrast. Several efforts have been made recently in this direction [Yashiro et al. (2011), Yashiro et al. (2010), Yang and Tang (2012), Lynch et al. (2011), Wolf et al. (2015)]. One of the most notable description was presented by Strobl (2014), which was later demonstrated experimentally by Prade et al. (2015). Schaff (2017) used the approach of Strobl (2014) and provided a detailed analysis of the relationship between XDF and SAXS by employing a back and forth combination of real and reciprocal space projection/slicing operation. In this section, we explain very briefly the relation between the measured dark-field signal to the size of the structures in the sample, namely the correlation length.

We saw in Eq. 2.6, that we measure the fourier transform of the three dimensional autocorrelation function in a SAXS measurement. In SAXS, we measure an integral through the three dimensional

function onto a 2D plane in the fourier space. In the case of XDF, we directly measure the autocorrelation function in the real space. Moreover, the three dimensional function is sliced along the $x - z$ plane (see Figure 4.1) due to the unidirectional sensitivity of the setup. Next, we integrate this function over the z axis and probe it at a certain point on the x axis, resulting in a scalar value:

$$G(\zeta_{GI}) = \int \gamma(x = \zeta_{GI}, 0, z) dz, \tag{4.6}$$

where ζ_{GI} is the correlation length of the XGI setup and is given by:

$$\zeta_{GI} = \frac{\lambda L_s}{p_2}, \tag{4.7}$$

L_s is the distance between the sample and G2 when the sample is placed between G1 and G2 (see Figure 4.6), λ is the wavelength of the incident beam and p_2 is the period of G2. This means that we can probe different auto-correlation lengths by moving the sample within the setup, or by changing its design energy. This has, recently, been demonstrated by Kagias et al. (2017).

4.5   Anisotropic Property

We saw in section 4.4 that the uni-directional specificity of the gratings leads to a 2D projection of the 3D auto correlation function on the sensitivity axis of the grating interferometer. This implies that the projected value of the correlation function varies with the relative orientation of the scattering function and the sensitivity axis. This leads to a very interesting property of the dark-field signal known as anisotropy [Jensen et al. (2010), Revol et al. (2012), Revol et al. (2013), Bayer et al. (2013), Lauridsen et al. (2014)]. To demonstrate this property, we show attenuation and dark-field images obtained for a sample made of three toothpicks, as it is rotated around the beam propagation direction (z axis in Figure 4.1). We can see in the top row of Figure 4.7 that the attenuation signal does not change with the pose of the sample, which is expected since the sample is always projected in the same direction, or in other words, the line integrals of the attenuation coefficients (Eq. 2.11) remains invariant under rotation around the beam propagation axis. On the other hand, we see that the value of the dark-field signal changes as the toothpicks are rotated around the z axis. This change is due to the anisotropic property of the dark-field signal. As the relative orientation of the scatterers changes with respect to the sensitivity axis, the measured dark-field signal also changes.

While anisotropy of the dark-field signal is an interesting property, it also implies that a single dark-field image is not sufficient to obtain the complete dark-field information inside a sample. Moreover, standard radiography or tomographic methods are not sufficient for X-ray dark-field imaging. This led to the development of Anisotropic X-ray Dark-field (AXDF) imaging. In the next section, we present a two dimensional AXDF imaging method.
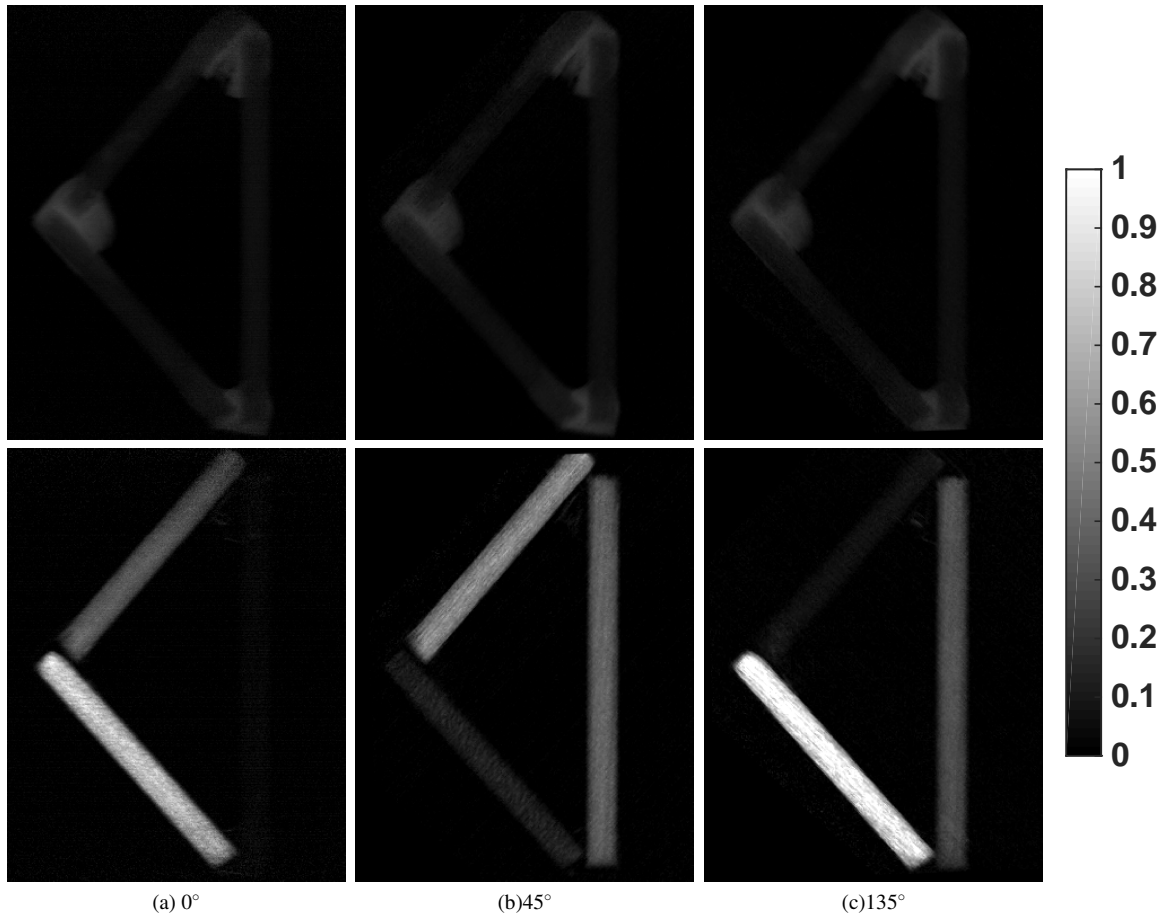
Figure 4.7: Attenuation vs. dark-field signal of a phantom made of three toothpicks. Top row shows X-ray attenuation and bottom row shows the corresponding dark-field image in three different orientations of the sample with respect to the grating bars (angle of the phantom with respect to the grating bars is indicated below the images). We can see that the attenuation images remain same while the dark-field changes with the orientation of the sample.

4.5.1   X-ray Vector Radiography

As the name suggests, X-ray Vector Radiography (XVR) [Jensen et al. (2010), Revol et al. (2012), Schaff et al. (2014), Potdevin et al. (2012), Prade et al. (2016)] is a two-dimensional imaging technique. It is aimed at the reconstruction of the orientation of sub-pixel sized structures without the need of resolving them. Several dark-field images are obtained by rotating the sample around the beam propagation direction such as the ones shown in Figure 4.7. This leads to a modulation of the dark-field signal as shown in Figure 4.7. This variation can be modeled as a sinusoid [Schaff et al. (2014)], with its phase representing the main structure orientation in every pixel. Figure 4.8 shows the orientations of wood fibres inside the toothpicks calculated by fitting a sinusoidal model to the visibility modulation. We can see that XVR reveals the orientations of wood fibres inside the toothpicks which are not directly resolvable at the resolution of the imaging system. It has been shown useful for analyzing
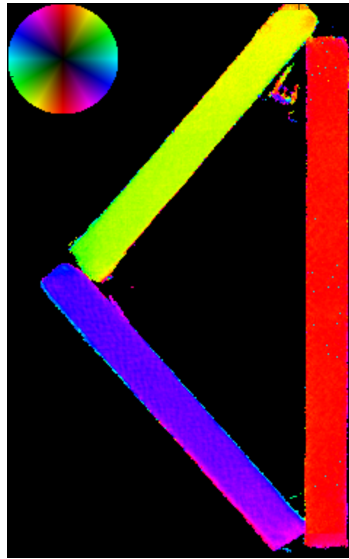
Figure 4.8: XVR result for the toothpick sample shown in Figure. 4.7.

the micro-structure of composite materials [Revol et al. (2012), Prade et al. (2016)] and biological specimen [Jensen et al. (2010), Potdevin et al. (2012), Schaff et al. (2014)].

Recently, Kagias et al. (2016) presented a novel design of circular gratings which can be used to probe all the directions of this anisotropic signal in a single shot. The circular gratings consist of a two dimensional arrangement of circular cells, each cell containing grating bars like the spokes of a wheel. Hence, each cell is able to record the component of scattering in several directions. Later, by considering each cell as a point on the object, we can directly recover the complete scattering information in this point. Such gratings, however, have been uses only with bright synchrotron sources and a high resolution detector. Practicality of such gratings with a lab source has not been reported yet. In this thesis, we will restrict our discussion to the most commonly used linear gratings.

Chapter 5

X-ray Dark-field Tomography

In the previous chapter, we discussed a two-dimensional directional dark-field imaging modality, namely X-ray Vector Radiography (XVR). We saw that it is a very convenient method to visualize the orientations of structures with sizes below the resolution of the imaging system. However, XVR suffers from two major drawbacks:

1. No 3D information in the reciprocal space i.e. XVR reveals only two-dimensional structure orientations projected onto the plane orthogonal to the beam propagation direction.

2. No real space 3D information i.e. the structure orientations are averaged throughout the thickness of the sample.

While the above two assumptions are useful for thin samples as has been demonstrated in literature, they become a serious hurdle for thick samples with multi-layered oriented structures. To overcome these limitations, we move to Anisotropic X-ray Dark-field (AXDF) tomographic modalities.

One of the early attempts in this direction was made by Bayer et al. (2014). They attempted to reconstruct the orientations by independently resolving scattering along two orthogonal directions and fitting a vector to the result. Another approach was recently presented by Schaff et al. (2017), which again involves the independent reconstruction of scattering along several directions and fits an ellipsoid to the result. Interestingly, their method works with Filtered back projection (section 3.2.1) and is, hence, computationally very cheap. Both the above methods involve manual alignment of the sample atleast two times within the setup.

The aim of the tomographic modalities discussed in this chapter is to reconstruct the reciprocal space scattering function inside every three-dimensional voxel using a single reconstruction model. One of the first efforts in this direction was made by Malecki et al. (2014) using a tensor model to approximate the scattering function which was later refined by Vogel et al. (2015). Recently, Wieczorek et al. (2016) presented a robust approach that enables the reconstruction of the spherical scattering function using spherical harmonics. We will present details of these two approaches in this chapter.

5.1   X-ray Tensor Tomography (XTT)

X-ray Tensor Tomography, as the name suggests, uses a tensor appoximation to model the scattering function. The goal of XTT reconstruction is to reconstruct a tensor $T(r) \in \mathbb{R}_+^{3 \times 3}$ in every voxel r. Malecki et al. (2014) divided this problem into two steps. In the first step, we calculate the scattering strength along certain pre-defined directions $\varepsilon \in \mathbb{S}^2$. In the second step, we used this information to fit a 3×3 tensor in every voxel. The smallest semi axis of the tensor represents the structure orientation. Below, we present details of the method.

5.1.1   Forward Model

The first requirement for any tomographic modality is a mathematical model for the physical process. Recall that the beer lambert law forms the basis of the model for standard computed tomography in Chapter 2. The Beer Lambert law is obviously not sufficient for dark-field tomography, owing to the directional dependence of the dark-field signal. Malecki et al. (2014) incorporated this directionality using weight functions and derived a modified beer lambert law as:

$$d(x) \approx exp \left[- \int_{t(x)} \sum_k w(\varepsilon_k, x) \cdot \zeta_k(r)^2 dr \right], \tag{5.1}$$

where $d(x)$ is the dark-field measurement integrated along the tomographic axis $t(x)$, $\varepsilon_k \in \mathbb{S}^2$, $k = 1, \cdots, K$ are predefined orientations and $\zeta_k(r) \in \mathbb{R}$ is the scattering strength in the voxel r along the orientation ε_k. $w(\varepsilon_k, x)$ is a weight factor that determines the strength of scattering along the orientation ε_k which will be measured at the sample pose x. We usually use a set of 13 directions as shown in Figure 5.1(a).

Recall from the previous chapter, that the logarithm of the dark-field signal obtained at a certain orientation with respect to grating bars can be modeled by a sinusoid. Malecki et al. (2013) extended this dependence to thick samples by using the superposition principle and derived the weight factor as:

$$w(\varepsilon_k, x) = \left(|\varepsilon_k \times t(x)| \, \langle \varepsilon_k, s(x) \rangle \right)^2, \tag{5.2}$$

where $t(x)$ and $s(x)$ are the tomographic and sensitivity axes at the pose x. They are given by:

$$\begin{aligned} t(x) &= R(x) \cdot T, \\ s(x) &= R(x) \cdot S, \end{aligned} \tag{5.3}$$

where $T \in \mathbb{S}^2$ and $S \in \mathbb{S}^2$ are the directions of the beam propagation and setup sensitivity, respectively.

5.1.2 Reconstruction

Malecki et al. (2014) proposed a modified SART approach for the reconstruction. Later, Vogel et al. (2015) established a generic formulation of the linear problem similar to the one in Eq. 3.13. Below, we briefly describe the approach of Vogel et al. (2015).

Re-writing Equation 5.1 with $\beta_k(r) = \zeta_k(r)^2$ results in:

$$
\begin{aligned}
-\ln(d(x)) &\approx \int_{t(x)} \sum_k w(\varepsilon_k, x) \cdot \beta_k(r) dr, \\
&= \sum_k w(\varepsilon_k, x) \int_{t(x)} \beta_k(r) dr.
\end{aligned}
\tag{5.4}
$$

By using one of the standard discretization methods for line integrals of $m = -\ln(d(x))$ over the rays $t(x)$ yielding a system matrix P, we arrive at:

$$
\begin{aligned}
m &= W_1 P \beta_1 + W_1 P \beta_1 + \cdots + W_k P \beta_k = \sum_k W_k P \beta_k, \\
&= \underbrace{\left(W_1 P \cdots W_k P \right)}_{= A_{XTT}} \begin{pmatrix} \beta_0 \\ \vdots \\ \beta_K \end{pmatrix},
\end{aligned}
\tag{5.5}
$$

where A_{XTT} is the full system matrix for XTT. We can see that Eq. 5.5 is a linear problem similar to conventional CT. The major difference is that the system matrix A_{XTT} is K times the size of the standard CT system matrix P. Writing the XTT problem in this way, provides the advantage that standard solvers can be used it. Vogel et al. (2015) proposed an interleaved approach to simultaneously solve the K linear systems, where in a single iteration of the whole system comprises of approximately solving K modified linear systems. In this work, we use the Conjugate Gradients (CG) solver to calculate $\beta_k(r)$, however, other solvers can be used as well. At last, we extract the scattering strengths:

$$
\zeta_k(r) = \sqrt{|\beta_k(r)|}.
\tag{5.6}
$$

5.1.3 Ellipsoid Fitting

In the previous section, we calculated the scattering strengths along K pre-defined orientations on the unit sphere. In figure 5.1(b), we can see 13 orientations from 5.1(a), scaled with their respective scattering strengths. We use Principal Component Analysis [Hotelling (1933)] (PCA) to approximate a 3×3 tensor in every voxel. For every voxel, we form a matrix M:

$$
M(r) := \{ \pm \zeta_1(r) \cdot \varepsilon_1, \pm \zeta_2(r) \cdot \varepsilon_2, \cdots \}.
\tag{5.7}
$$
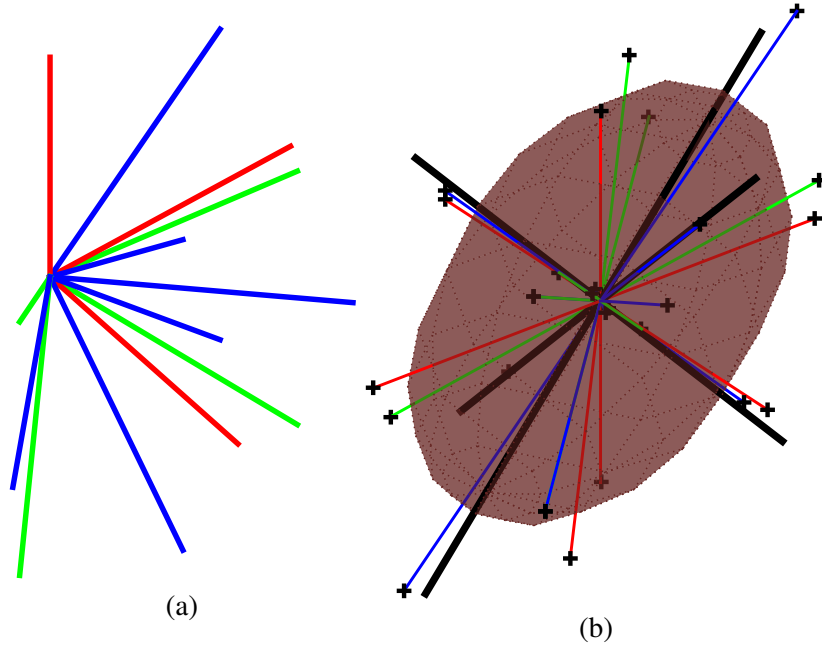
Figure 5.1: (a) Pre-defined scattering orientations ε_k, $k = 1 \cdots 13$ used for XTT reconstruction. These directions correspond to the three sides (red), face diagonals (green) and body diagonals (blue) of a cube. (b) The orientations in (a) scaled with their corresponding scattering strength. We fit an ellipsoid to the scaled orientations as shown, the three semi axis of the ellipsoid are also shown in black bold color. Smallest half axis corresponds to the orientation of the scattering structure.

Next, we perform an eigen decomposition of this matrix to obtain:

$$V \cdot \Lambda = C \cdot V \tag{5.8}$$

where $C \in \mathbb{R}^{3 \times 3}$ is the covariance matrix of M, $\Lambda \in \mathbb{R}^{3 \times 3}$ is a diagonal matrix containing the three eigen values $\lambda_1, \lambda_2, \lambda_3$ and $V \in \mathbb{R}^{3 \times 3}$ contains the corresponding eigen vectors v_1, v_2, v_3 which are mutually orthonormal. We define a scaling factor in every voxel as:

$$\sigma := \frac{\sum_k |\beta_k|}{K} \left/ \left(\frac{|\lambda_1| + |\lambda_2| + |\lambda_3|}{3} \right) \right. . \tag{5.9}$$

Finally, we define the scattering tensor in every voxel by the half axis lengths $r_1 = \sqrt{\sigma \lambda_1}, r_2 = \sqrt{\sigma \lambda_2}, r_3 = \sqrt{\sigma \lambda_3}$ corresponding to the half axis v_1, v_2, v_3. The tensor thus obtained is shown in Figure 5.1(b), alongwith the three semi axes. Since oriented structures scatter primarily in the orthogonal direction, the smallest half axis v_3 represents the main structure orientation in every voxel.

5.2 Anisotropic X-ray Dark-Field Tomography (AXDT)

In the previous section, we presented the reconstruction method for X-ray Tensor Tomography (XTT). XTT uses a tensor approximation for the scattering function and the smallest half axis of the tensor is considered as the main orientaition of the scattering structures. This model has a major disadvantage that it only assumes a single scattering structure inside every volume element. This assumption is not valid, especially, since directional dark-field imaging reveals structures with size much smaller than the spatial resolution of the system. In order to overcome this limitation, Wieczorek et al. (2016) modeled the scattering function as a spherical function using the basis of spherical harmonics. Such a formulation provides a more generic description of the scattering function and allows for the reconstruction of multiple scattering structures in a single real space voxel. Below, we present the details of the AXDT reconstruction approach.

5.2.1 Reconstruction

Recall the XTT forward model from Eq. 5.1:

$$d(x) = exp\left[-\int_{t(x)} \sum_k w(\varepsilon_k, x) \cdot \zeta_k(r)^2 dr \right], \tag{5.10}$$

The model involves a representation of the scattering function as a summation of scattering magnitudes evaluated at discrete scattering orientations. The first step to a continuous model is replacing the summation with an integral. By replacing the discrete weighting function $w(\varepsilon_k, x)$ with $h : \mathbb{S}^2 \times \mathbb{S}^2 \times \mathbb{S}^2 \to \mathbb{R}$ and representing the field of scattering functions as $\eta : \mathbb{S}^2 \times \mathbb{R}^3 \to \mathbb{R}$, we get:

$$d(x) = exp\left[-\int_{T(x)} \int_{\mathbb{S}^2} h(u,x)\eta(u,r)\frac{d\Omega(u)}{4\pi} dr \right], \tag{5.11}$$

where $d\Omega(u)$ denotes the standard solid angle. $h(u,x)$ models the relationship between the sensitivity vector $s(x)$ and tomographic vector $t(x)$ for every pose x, as before:

$$h(u,x) = \left(\left| u \times t(x) \right| \left\langle u, s(x) \right\rangle \right)^2. \tag{5.12}$$

We use the orthonormal basis of spherical harmonics to discretize the spherical functions. A square integrable function $f \in \mathbb{L}^2(\mathbb{S}^2)$ can be decomposed using this basis as:

$$f = \sum_{k=0}^{\infty} \sum_{m=-k}^{k} f_k^m V_k^m, \tag{5.13}$$

where $\left\{ V_k^m \right\}_{k=0,\cdots,\infty; m=-k,\cdots,k}$ is the set of real-valued coefficients; index k is called the degree and m is called the order of the spherical harmonic.
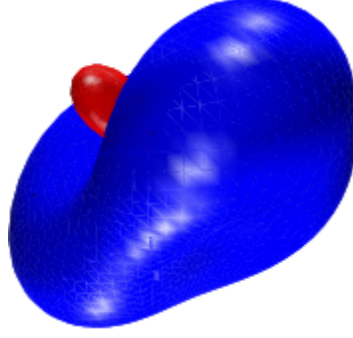
Figure 5.2: Scattering function in a single voxel reconstructed using the AXDT method.

Using spherical harmonics to discretize the inner integral, we get:

$$d(x) = exp\left[-\frac{1}{4\pi}\int_{t(x)}\sum_{k=0}^{\infty}\sum_{m=-k}^{k}h_k^m(x)\eta_k^m(r)dr\right], \tag{5.14}$$

where the scattering function as well as the weighting function are expressed in terms of real-valued spherical harmonics with their coefficients denoted as η_k^m and h_k^m, respectively. By swapping summation and integration and using a truncation degree K for the spherical harmonics, we get:

$$d(x) \approx \exp\left(-\frac{1}{4\pi}\sum_{k=0}^{K}\sum_{m=-k}^{k}h_k^m(x)\int_{t(x)}n_k^m(r)dr\right). \tag{5.15}$$

Spherical harmonics of degree 4 are sufficient to describe the spherical function completely with the weighting function that is used [Wieczorek (2017)].

Again, by using one of the standard discretization methods for line integrals of $m = (-\ln(d(x)))$ over the rays $t(x)$ yielding a system matrix P and by forming weighting matrices W_k^m according to $h_k^m(s(x), t(x))$, the reconstruction of the spherical harmonics coefficients of the field of scattering profiles reduces to solving the following linear equation system:

$$m = \sum_{k=0}^{K}\sum_{m=-k}^{m=k}W_k^m P\eta_k^m = \underbrace{\left(W_0^0 P \quad \cdots \quad W_K^{-K}P \quad \cdots \quad W_K^K P\right)}_{= A_{AXDT}}\begin{pmatrix}\eta_0^0 \\ \vdots \\ \eta_K^{-K} \\ \vdots \\ \eta_K^K\end{pmatrix}, \tag{5.16}$$

where we call A_{AXDT} as the full system matrix.

We solve this system using the conjugate gradient method with $K = 4$. An instance of scattering function reconstructed using the described method in a single voxel is shown in Figure 5.2.

5.2.2 Micro-structure extraction

As discussed in the case of XTT, the micro-structure orientation is orthogonal to the direction of maximum scattering. This means that the structure orientation can be found in the greater circles $C(u) := \{u' \in \mathbb{S}^2,\ \langle u', u \rangle = 0\}$ orthogonal to the maximum scattering direction u. Therefore, for a reconstruction $\eta(u, r)$, we compute the Funk-Radon transform [Funk (1913)] in every volume element:

$$\hat{\eta}(u, r) := \int_{C(u)} \eta(u', r) ds(u'). \tag{5.17}$$

This can be again computed easily using the basis of spherical hamonics as:

$$\hat{\eta}_k^m(r) = L_k(0) \eta_k^m(r), \tag{5.18}$$

L_k denotes the Legendre polynomials:

$$\begin{aligned} L_{2k+1}(0) &= 0, \\ L_{2k} &= (-1)^k \frac{1 \cdot 3 \cdot 5 \cdots 2k - 1}{2 \cdot 4 \cdot 6 \cdots 2k}. \end{aligned} \tag{5.19}$$

The peaks in $\hat{\eta}_k^m(u, r)$ correspond to the main structure orientation in the volume element r.

Part III

Acquisition Methods for Anisotropic X-ray Dark-field Imaging Modalities

Chapter 6

Trochoidal X-ray Vector Radiography

We discussed the method of X-ray Vector Radiography in section 4.5.1. XVR is a novel X-ray imaging modality that reveals the orientations of sub-pixel sized structures within a specimen. XVR finds applications in many industrial and clinical environments. In this chapter, we provide a detailed analysis of the conventional XVR imaging method and its limitations and present a new approach to overcome some of these limitations.

We begin by explaining, in detail, a standard acquisition scheme for XVR. Lets us now assume an acquisition scheme comprising of N poses:

$$X(N) := \left\{ x = (\theta); \ \theta \in \left\{ 0, \frac{180°}{N}, \ldots, 180° - \frac{180°}{N} \right\}, N \in \mathbb{N} \right\}. \tag{6.1}$$

We note that the definition of the rotation matrix $R(x)$ in this case is different from the one defined in Eq. 3.19. Since θ is the angle of rotation around the z axis, the rotation matrix is defined as:

$$R(x) = R_z(\theta) = \begin{bmatrix} \cos\theta & -\sin\theta & 0 \\ \sin\theta & \cos\theta & 0 \\ 0 & 0 & 1 \end{bmatrix}. \tag{6.2}$$

An XGI setup with linear gratings has a preferred sensitivity direction. We refer to this direction as the sensitivity axis. The sensitivity axis at a sample pose x is defined as the direction orthogonal to the alignment of grating bars and lying in the plane of the grating. Similar, to the previous definition of the optical axis, the sensitivity axis can be defined as:

$$s(x) = R(x) \cdot S, \tag{6.3}$$

<table>
<tr><td>(a)</td><td>(b)</td></tr>
</table>
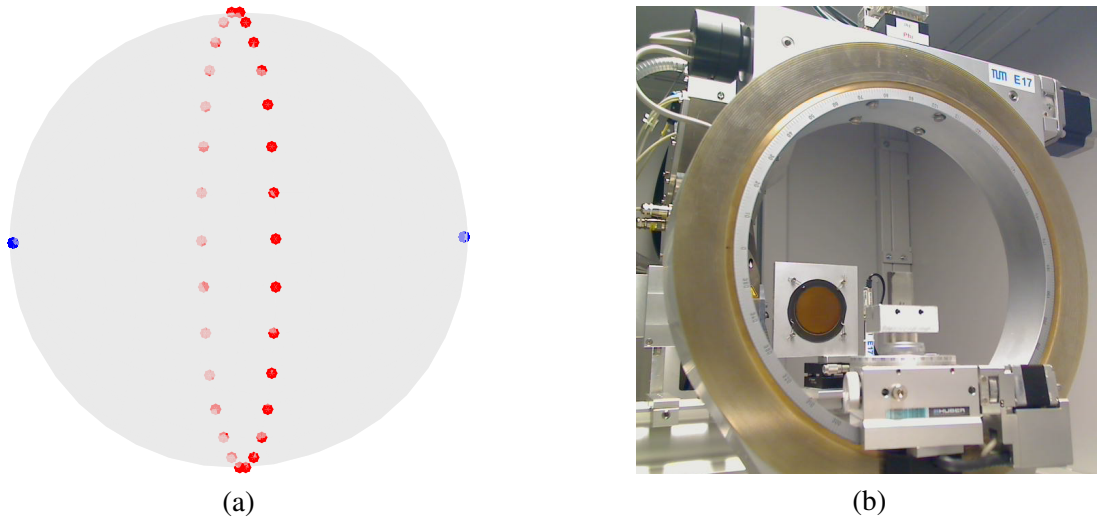
Figure 6.1: (a)Spherical representation of XVR acquisition. The blue and red points denote the unit vectors $\pm t(x)$ and$\pm s(x)$ for all $x \in X(16)$ (Eq. 6.1) (b) Eulerian cradle that is typically used to realize the acquisition scheme shown in (a).

where S is the sensitivity direction of the setup.

We extend the spherical representation presented in section 3.3.1 to the case of XVR. We plot the tomographic and the sensitivity axes for the acquisition scheme $X(N)$ in Figure 6.1(a). Red points represent the trajectory of the sensitivity axis while the blue points denote the optical axis. We can see that for the acquisition scheme $X(N)$, different sensitivity directions are probed for the same optical direction. This means, that while we do not have any tomographic information about the sample, we are probing the scattering information over the circular trajectory orthogonal to the beam propagation direction.

Typically, this is done by mounting the sample on an eulerian cradle as shown in Figure 6.1(b). The typical steps of a XVR measurement include:

1. Select the number of poses N and mount the sample on an eulerian cradle in an XGI setup.

2. For every $x \in X(N)$:

   (a) Rotate the sample to the pose x.

   (b) Perform a standard phase stepping procedure to obtain the dark-field image $V(x)$.

3. Register the images $V(x)$, $x \in X(N)$.

4. Use a sinusoidal model for visibility modulation to extract the main structure orientation.

While, step 2(a) is needed to probe different points on the visibility curve; step 2(b) samples the intensity curve (Figure 4.2) to get a single point on the visibility curve.

The XVR method discussed above requires a stepwise method involving rotation of the sample to several poses and a phase-stepping procedure for every pose. Translation of gratings with period in

Grating	G0	G1	G2
Type	absorption	$\pi/2$ phase-shift	absorption
Lamellae	Gold	Nickel	Gold
Period(µm)	8.09	4.12	8.4
Duty Cycle	0.5	0.5	0.5
Material Height(µm)	115	5.21	136

Table 6.1: Gratings used for the TXVR setup shown in Figure 6.2.

the order of a few micrometers induces additional chances of vibration and instabilities leading to erroneous results in a conventional XGI setup. Moreover, the eulerian cradle is a bulky component posing a significant challenge to the commercialization of this technology. To overcome these limitations we present a method that does not require any grating translation during the measurement, works with laboratory X-ray sources and is suitable for fast scanning of continuously moving samples placed on a commonly used industrial stage. The key idea of our new method is to combine step 2 of the XVR procedure described above into a single step. This is done by combining both the phase stepping and the visibility sampling into the sample motion. Owing to the sample trajectory used, we name our method as Trochoidal X-ray Vector Radiography (TXVR). Below, we present the details of TXVR.

6.1   Setup

We use a vertical XGI setup presented by Bachche et al. (2017), designed with the aim of scanning fast moving samples in an industrial setting, for example, on a conveyor belt. The X-ray source is a tungsten rotating anode source (UltraX 18, Rigaku, Japan). The focus size on the anode is 0.3 mm x 3 mm. With a take off angles of $6°$, the effective spot size is 0.3 mm x 0.3 mm. It is placed at the bottom of the setup and emits X-rays vertically in the upward direction to the detector. The detector is a photon counting detector with a FOV of 77.5 mm x 38.5 mm and a pixel size of 100×100 µm. The detector has a fast count rate and readout speed of upto 174 fps.

Three gratings are placed between the source and the detector. G0 has a period of 8.09 µm, $\pi/2$ phase grating G1 has a period of 4.12 µm, and G2 has period of 8.4 µm. The gratings are arranged in the first talbot configuration with distances of 397 mm and 417 mm between G0-G1and G1-G2, respectively. The heights of the three gratings are 115 µm, 5.21 µm and 136 µm respectively. Grating specifications are provided in Table 6.1.

A linear sample stage is mounted in between G1 and G2. In addition, a rotational motor is mounted on the linear stage with a hole in the middle to allow X-rays to pass through. An acyrlic plastic is mounted on the center (hole) of the rotation stage for placing the sample.

HyPix 3000
Pixel size: 100 x 100 μm^2

G2 : Absorption grating
Period: 8.4 μm

Trochoidal Sample
Trajectory

G1 : Phase grating
Period: 4.12 μm

G0 : Source grating
Period: 8.09 μm

X-ray Source
40 kV, 70 mA

417 mm

397 mm

207 mm
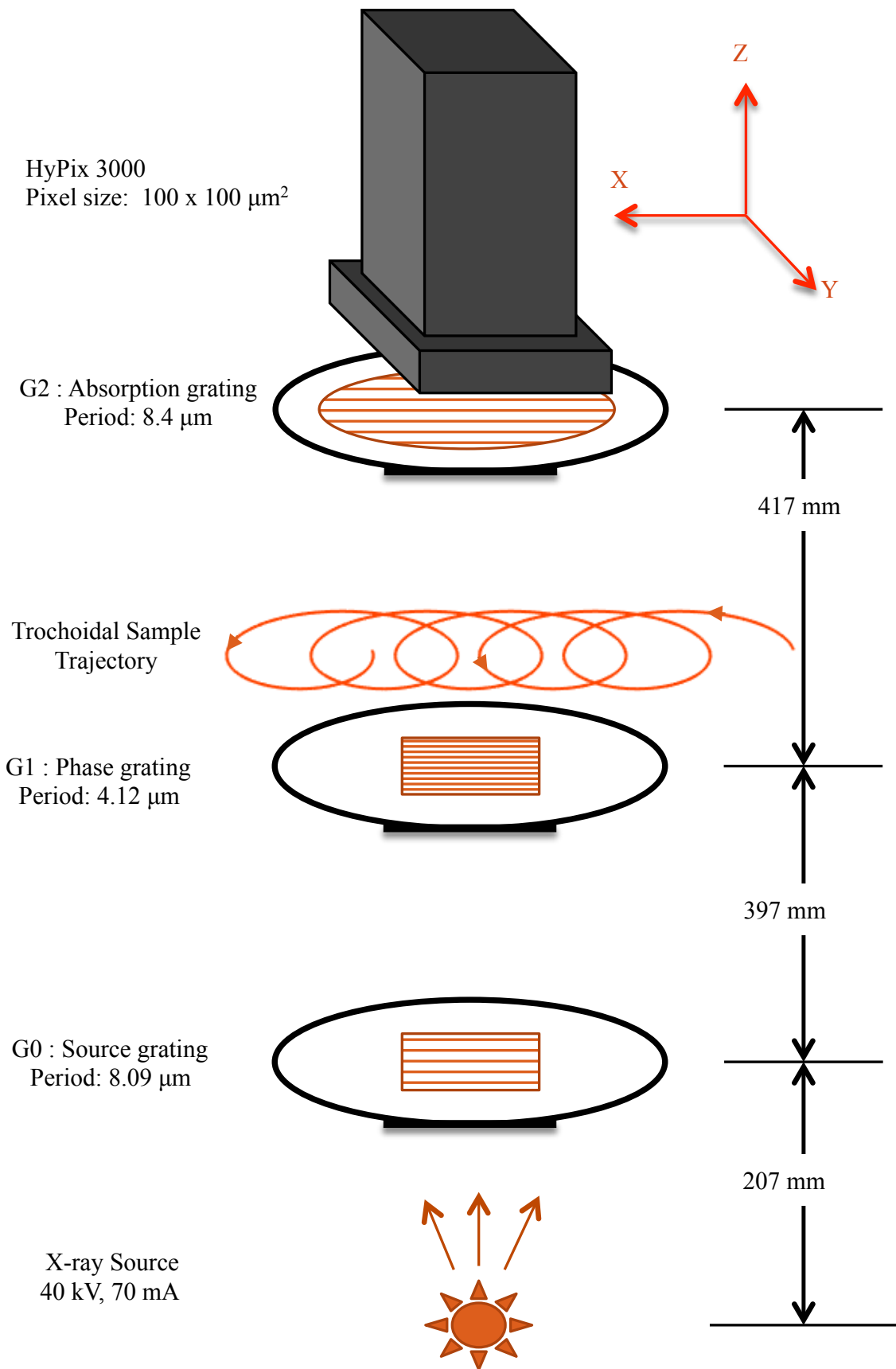
Figure 6.2: Schematic of a vertical grating interferometer setup used for Trochoidal X-ray Vector Radiography (TXVR). Figure by Sharma et al. (2018) is licensed under CC BY 4.0.

6.2   Measurement

In this section, we present a method to perform XVR with two main advantages:

1. no grating stepping, and

2. continuous movement of sample

during the measurement. Below, we describe how this is achieved in the setup shown in Figure 6.2.

The setup described in the previous section enables simultaneous linear and rotational motion of a sample placed on the rotational stage. Let us consider a point on the sample which is located at a distance r from the centre of rotation and makes a counterclockwise angle α with the positive x axis at time $t = 0$, such that its cartesian coordinates in the sample frame can be written as (see Figure 6.3):

$$
\begin{aligned}
p &= r\cos(\alpha), \\
q &= r\sin(\alpha).
\end{aligned}
\tag{6.4}
$$

The motion of this point on the detector plane, with (x, y) denoting the coordinates of a detector pixel, can be written as:

$$
\begin{aligned}
x &= rM\cos(\omega t + \alpha) + ut, \\
y &= rM\sin(\omega t + \alpha),
\end{aligned}
\tag{6.5}
$$

where ω is the angular speed of the sample rotation, M is the magnification of the system and u is the linear speed of the sample on the detector plane with unit of $pixels/s$. u is related to the speed of the linear stage v by:

$$
u = \frac{v \cdot M}{d}
\tag{6.6}
$$

where d is the detector pixel size. Let:

$$
H(p, q, t) = \left(H_x(p, q, t), H_y(p, q, t) \right),
\tag{6.7}
$$

where $H_x(p, q, t)$ and $H_y(p, q, t)$ are functions that relate the detector coordinates x and y, respectively, to the sample coordinates (p, q) at time t. $H_x(p, q, t)$ and $H_y(p, q, t)$ can be easily derived from Equations 6.4 and 6.5. The motion described by Eq. 6.5 falls under one of the three special cases of a trochoid namely cycloid, curtate cycloid or prolate cycloid, depending on the ratio of the linear speed and the tangential speed at the distance r from the centre of rotation. Therefore, we use trochoid as the generic term to describe the motion of the sample and term our method as Trochoidal X-ray Vector Radiography (TXVR).

Prior to the measurement, we need to establish a field of moire pattern in the detector FOV. This is done by rotationally misaligning the gratings G1 and G2 slightly, resulting in moire fringes as seen in Figure 6.3. We can see in Figure 6.3 that the fringes are not uniform due to slight inhomogeneities in the grating structure. Next, we perform a standard phase stepping procedure by displacing G2 in
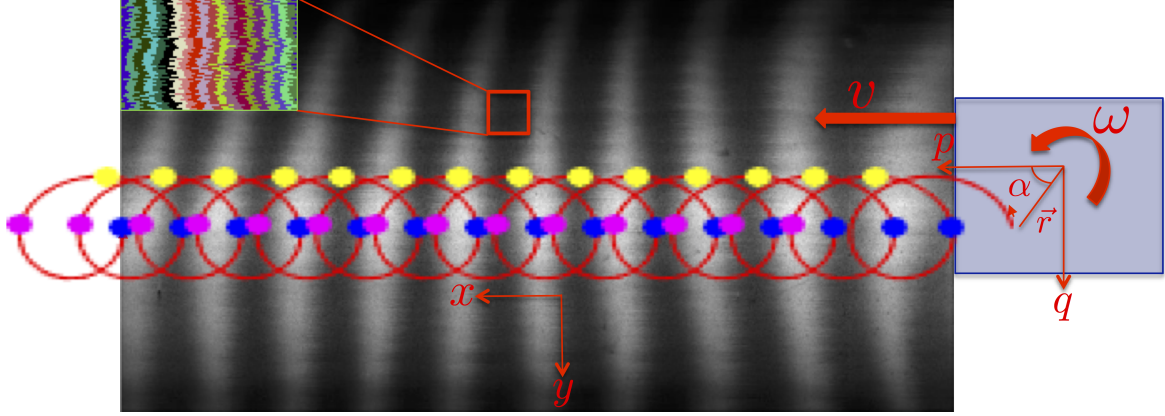
Figure 6.3: Detector FOV with 775 x 385 pixels (top view from Figure 6.2). We can see moire fringes introduced by slightly rotating the gratings G1 and G2 with respect to each other. The phase image without the sample is discretized into n bins as shown in the zoomed inset (Eq. 6.8), this is used for the algorithm of image formation (Eq. 6.12). The trajectory of a point (p,q) on the sample (Eq. 6.5) is shown in red. Blue, yellow and magenta points show the position of this point at times T_θ for three different values of θ (Eq. 6.11).

steps over one period and calculate the background absorption $A_0(x,y)$, differential phase $\phi_0(x,y)$ and visibility $V_0(x,y)$ images, where (x,y) denotes the coordinates of pixels in the detector plane. Sometimes it is required to tune the grating alignment in order to ensure that the values of ϕ_0 span the range $[-\pi, \pi]$ along the x direction for every row y in the FOV. Once this is achieved, we discretize the 2D moire field into K regions represented by indicator matrices F_k:

$$F_k(x,y) = \begin{cases} 1, & \text{if } -\pi + \frac{2\pi(k-1)}{n} < \phi_0(x,y) \le -\pi + \frac{2\pi k}{n} \\ 0, & \text{otherwise} \end{cases},$$

$$k = 1, 2, \cdots, K.$$

(6.8)

The number of pixels in every row y in each indicator matrix is stored in the vector $N_k(y)$.

We acquire movie frames $I_t(x,y)$ at time $t \in T$, where:

$$T = \left\{ 0, \frac{1}{f}, \frac{2}{f}, \cdots, \frac{N_F}{f} \right\},$$

(6.9)

f is the detector frame rate and N_F is the total number of frames recorded as the sample moves in a trochoidal trajectory (given by Eq. 6.5) across the FOV.

6.3   Algorithm

The measurement described in the previous section, provides a set of frames I_t, $t \in T$. The processing algorithm consists of two major steps:

1. Trochoidal Phase Scanning to calculate the N dark-field images at poses $x \in X(N)$.

2. Standard XVR processing to calculate structure orientations from the N dark-field images.

6.3.1 Trochoidal Phase Scanning

In this step, we obtain N attenuation ($A(\theta)$) and dark-field images ($V(\theta)$) at the pose $\theta \in \Theta$, with respect to the pose at $t = 0$, where Θ is:

$$\Theta = \left\{ 0, \frac{360°}{N}, \ldots, 360° - \frac{360°}{N}; N \in \mathbb{N} \right\} \tag{6.10}$$

These N images are equivalent to those obtained using the acquisition scheme $X(N)$ in Eq. 6.1.

In order to to do, first we decouple the linear and rotational motion. This is done by selecting frames $I_t, t \in T_\theta$, such that:

$$T_\theta = \left\{ t \in T : t = \frac{\theta + 2\pi j}{\omega} \text{ for } j \in \mathbb{N} \right\}. \tag{6.11}$$

The set of frames, acquired at the positions denoted by blue points on the trochoidal trajectory shown in Figure 6.3, represents a linear motion of the point (p, q) at a pose θ with respect to the pose at $t = 0$.

From this linear movie, we calculate $J_k(\theta, p, q)$ utilizing the algorithm described by Bachche et al. (2017):

$$J_k(\theta, p, q) = \sum_{t \in T_\theta} \frac{I_t(H(p, q, t)) \cdot F_k(H(p, q, t))}{A_0(H(p, q, t)) \cdot N_k(H_y(p, q, t))}. \tag{6.12}$$

$J_k(\theta, p, q)$ is the stepping curve for every angular position θ of the sample such as the one that would be obtained by the conventional phase stepping approach. It encodes the information about the change in the background phase map caused by the point (p, q) in the sample as it crosses the FOV in the orientation θ. Next, we fit a sinusoid to the stepping curve for every θ:

$$J_k(\theta, p, q) \approx a_0(\theta, p, q) + a_1(\theta, p, q) \cos \left[\frac{2\pi}{n} k - \phi(\theta, p, q) \right]. \tag{6.13}$$

We perform the trochoidal phase scanning procedure described above with the sample in the FOV to obtain the parameters $a_0^s(\theta, p, q), a_1^s(\theta, p, q)$ and $\phi^s(\theta, p, q)$ for the sample and without the sample to obtain $a_0^b(\theta, p, q), a_1^b(\theta, p, q)$ and $\phi^b(\theta, p, q)$ for the background. We can, thus, calculate the absorption and dark-field (visibility) image as explained in section 4.2:

$$A(\theta, p, q) = \frac{a_0^s(\theta, p, q)}{a_0^b(\theta, p, q)},$$
$$V(\theta, p, q) = \frac{a_1^s(\theta, p, q) \cdot a_0^b(\theta, p, q)}{a_1^b(\theta, p, q) \cdot a_0^s(\theta, p, q)}. \tag{6.14}$$

From now on, we use the short notations A_i and V_i to denote the attenuation and visibility images obtained at the pose $\theta = \dfrac{i \cdot 360°}{N}$ with respect to the pose at $t = 0$. We choose an odd number for N to allow for interlaced sampling over $[0, 2\pi]$.

6.3.2   XVR Processing

Registration

We register the attenuation images A_i to the image A_0 using rotation and translation, and use the resulting transformation matrices to register the corresponding visibility images. Post registration, we define the mean attenuation image as:

$$A_{mean} = \sum_{i=0}^{N-1} \frac{-\ln(A_i)}{N} \qquad (6.15)$$

Model Fitting

So far, we obtained the dark-field values V_i corresponding to $\theta = \dfrac{i \cdot 360°}{N}$. Next, we use these images to calculate the main structure orientation in every pixel. V_i encodes the variation in the dark-field signal as the orientation θ of the scattering structure with respect to the grating bars is varied over $[0, 2\pi]$. We model this variation as a sinusoid as proposed by Schaff et al. (2014):

$$-\ln(V_i)) \approx b_0 + b_1 \cos\left[2\left(\frac{2i\pi}{N} - \gamma \right) \right]. \qquad (6.16)$$

Finally, we define three quantities as:

1. b_0 - Mean dark-field

2. b_1/b_0- Anisotropy

3. γ- Main structure orientation

6.4   Experiments

First, we obtain the background phase map $F_k, k = 1, \cdots, K$, where $K = 20$ using the phase stepping procedure described in section 6.2. Note that the value of $K = 20$ is obtained empirically, any $K \geq 3$ can be used. Next, we set the parameters for trochoidal scanning. One of the most important factors to tune is the rotation speed and the number of rotations within the FOV. We use 100 full rotations of the sample in the FOV to obtain 100 images for calculating $J_k(\theta)$ for every pose θ (Eq. 6.12). Again, we note that 100 full rotations are only required for good statistics. Theoretically, 3 rotations are enough.

We determine the scanning distance as the total distance for the entire sample to cross the FOV from left to right. This turns out to be 80 mm for the size of the samples used. We use the maximum

(a)   (b)   (c)
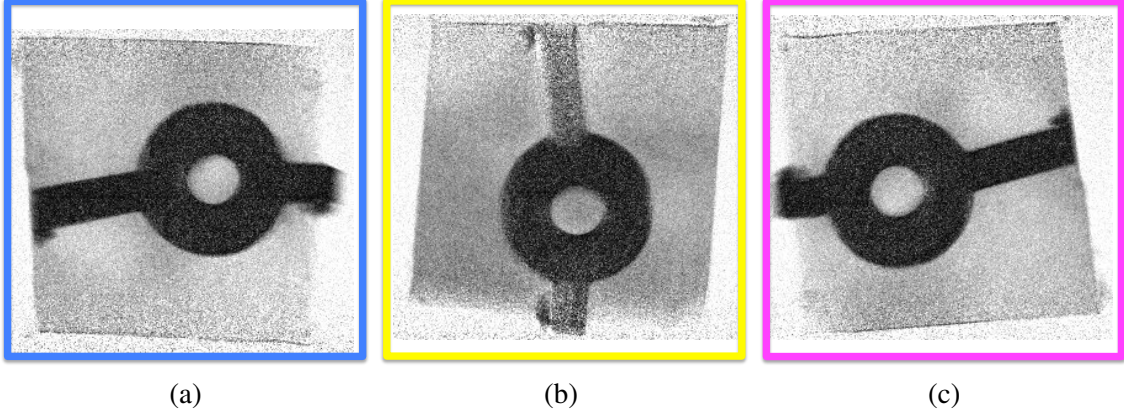
Figure 6.4: The visibility images $V_i, i = 0, 7, 15$ for $N = 31$ obtained using the trochoidal phase scanning algorithm described in section 6.3.1. The outline colors correlate roughly to the colored points in Figure 6.3 representing the decoupled linear trajectories for each of the three images.

Rotation Speed ω	30 deg/sec
Number of Rotations	100
Scanning Distance	80 mm
Linear Speed v	0.0752 mm/sec
Total Scan Time	20 mins
Frame rate	66.67 fps
Total frames	80000

Table 6.2: Settings used for TXVR.

rotation speed of the motor i.e. 30 deg/sec. Therefore, we can calculate the speed of the linear motor such that 100 rotations are possible in a distance of 80 mm. Another important factor is to ensure that the ratio of the rotation speed in deg/sec to the exposure time is an integer. Here, we set an exposure time of 15 ms, which is just enough to obtain good statistics. We perform trochoidal scanning with the settings shown in Table 6.2 with and without the sample in the FOV.

We measure a total of 80000 frames in a total scan time of 20 mins. We use $N = 31$ (Eq. 6.1) for the phase scanning algorithm (section 6.3.1) i.e. we obtain images A_i and V_i for $i = 0, \cdots, 30$. Finally, we calculate the mean attenuation as given by Eq. 6.15, the mean dark-field, anisotropy and vector images according to Eq. 6.16.

6.5   Results

We show results for 3 samples measured using TXVR. The first sample is a small specimen cut out of polypropylene reinforced with glass fibres manufactured using injection molding process. We show three dark-field images V_0, V_7, V_{15} obtained using the trochoidal phase scanning procedure (section 6.3.1) for this sample in Figure 6.4. We can see that these three images correspond to $\theta = 0°, 81.3°, 174.2°$ with respect to the pose at $t = 0$.

(a) Mean attenuation   (b) Mean dark-field   (c) Anisotropy (masked)
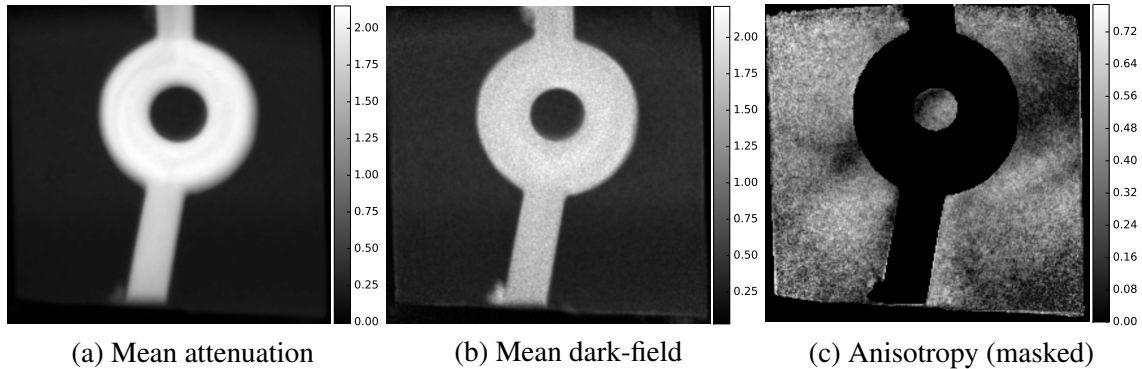
Figure 6.5: TXVR result for a glass fibre composite material. The bright part in (a) is a thick screwhole extending out of the plane. We mask it out for the anisotropy image in (c).

Finally, we show the mean attenuation image and mean dark-field images in Figure 6.5(a) and (b), respectively. The bright part in the middle is a thick screw hole (female screw) extending out of the plane with a thin plate at the bottom. Since the screw hole is too thick for the X-ray energy used, we mask it out and show the TXVR result only for the bottom plate. We show the masked anisotropy in Figure 6.5(c). We can see that anisotropy provides more information than the mean dark-field image and suggests the presence of oriented structures i.e. the glass fibres. We show the vector image in Figure 6.6(a). The colored bars represent the orientations of the glass fibres resulting from the molding process that is used for manufacturing. The orientations of the glass fibres with diameters in the range of a few microns can be determined in this image, which has a pixel size of approximately 70 μm.

We show results for a sample with known orientations in Figures 6.7 and 6.8(a). It is a rubber pipe reinforced with a crossed arrangement of nylon fibres. We can see in Figure 6.8(a) that the orientation of the nylon fibres can be determined using TXVR. Moreover, we see in Figure 6.7 that the anisotropy image provides a better distinction of the fibres inside the matrix. The third sample shown in Figure 6.8(b) is the cap of a species of mushroom found in East Asia (Hypsizygus tessellatus). There are hundreds of flat, vertical partitions radiating out like spokes of a wheel from the centre of the cap known as gills. Here, we can see the radial orientations of these gills beneath the mushroom cap. The colored bars represent the orientations of the gills calculated using TXVR.

6.5.1   Comparison of XVR and TXVR

We also performed a conventional XVR measurement of the sample shown in Figure 6.6(a). Figure 6.6(b) shows the result of conventional X-ray Vector Radiography (XVR) with phase stepping using a setup and method described by Prade et al. (2016). The setup used for the XVR measurement comprises of a micro-focus X-ray tube (operated at voltage 60 kV and power 40 W) and a Varian PaxScan 2520DX detector (pixel size 127 μm). The three gratings with periods of 10 μm, 5 μm, and 10 μm, respectively, were arranged in the first fractional Talbot configuration. The effective pixel size of the data was approximately 55 μm and the total exposure time was 231 s. The sample holder can
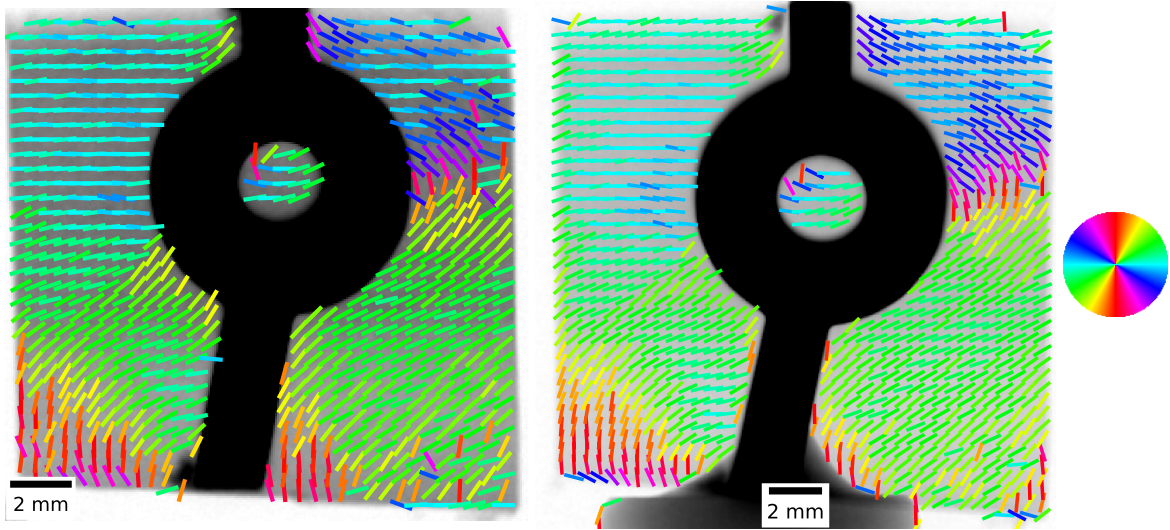
Figure 6.6: Vector images obtained using (a) TXVR (b) Conventional XVR. Two dimensional orientations $\gamma(p,q)$ (Eq. 6.16) are displayed as color coded unit vectors overlaid on the corresponding gray-scale attenuation image. Coloring is obtained by converting the value of $\gamma(p,q)$ to HSV (Hue, Saturation & Value) by setting hue equal to $\gamma(p,q)$, and saturation and value equal to 1 for all pixels; the colorwheel on the right should be used for interpreting the colors. The grayscale values are set between $[0.6, 1]$ for (a) and $[0.7, 1]$ for (b). The central part is a thick screw hole, hence, we mask it out for displaying the orientations of the glass fibres in the thin plate at the bottom of the screw hole. We show every 7th pixel in (a) and every 9th pixel in (b).

be seen at the bottom of Figure 6.6(b), which was required in order to place the sample vertically in a horizontal setup.

To further quantify the similarity, we register the mean attenuation data (A_{mean}) of XVR to that of TXVR. We should note that the TXVR data has a lower resolution than the corresponding XVR measurement. Therefore, we register the high resolution XVR data to the low resolution TXVR data. We use scale, rotation and translation to register the corresponding attenuation images. We then apply the transformation matrix obtained to transform the XVR result. We calculate pairwise dot product of unit vectors obtained using the two methods. Figure 6.9(a) shows the dot product between unit vectors obtained using TXVR and TXVR. Bright pixels imply that the angular deviation is small. We show the histogram of the angular deviation inside the roi (marked with a red rectangle) in Figure 6.9(b).

We can see from Figure 6.9 that the results obtained using the two methods are consistent. Small deviations can be attributed to imperfect registration owing to the difference in sample mounting (vertical vs. horizontal). The presence of sample holder in XVR data makes registration particularly difficult. Moreover, both the measurements were made on different setups leading to major differences in several parameters such a source size, detector resolution, magnification etc. An objective study of TXVR and XVR with equivalent data is part of future work.

(a) Mean attenuation   (b) Mean dark-field   (c) Anisotropy (masked)
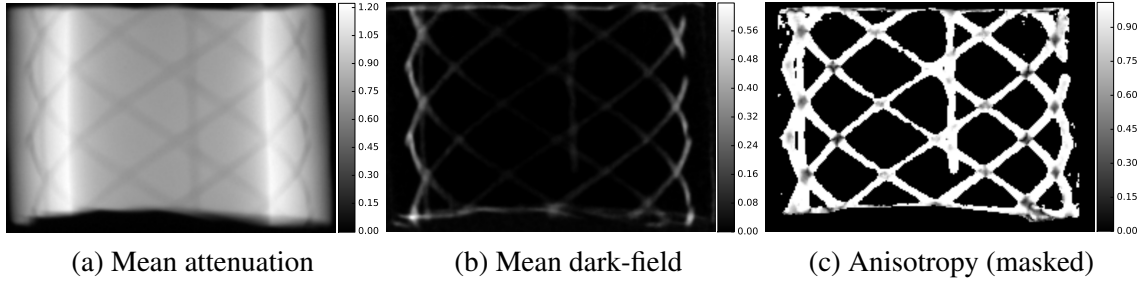
Figure 6.7: TXVR result for a known sample made of nylon fibres. We can see that anisotropy image (masked using the attenuation image) provides a much better definition of the fibres than mean attenuation or mean dark-field.

6.6 Limitation

We note that owing to the trochoidal trajectory, the tangential velocity varies with the distance from the centre of rotation. This implies that the effective linear velocity used for phase scanning (Eq. 6.12) is different for different points inside the sample. Theoretically, this will lead to a blurring in the images. However, owing to the processing on digital images, this does not happen as long as this variation is less than 1 pixel/frame. We define:

$$r_{max} = \frac{d \cdot f}{\omega \cdot M} \tag{6.17}$$

as the maximum distance from the centre of rotation where this condition is satisfied. Therefore, we do not induce any additional blurring as long as the sample fits inside a circle of diameter $2r_{max}$ around the center of rotation. $r_{max} \approx 1$ cm for the settings used in this work which is sufficient for the size of the samples used. For bigger samples, we need to decrease the rotation speed or increase the detector pixel size to ensure that this condition is satisfied.

6.7 Summary and Outlook

X-ray Vector Radiography is a novel imaging method to reveal the orientations of micro-structures inside a specimen. In this chapter, we use a novel method to perform XVR of a continuously moving sample without the need to step gratings during the acquisition process. This provides several advantages in terms of stability and repeatability, making this kind of system easily adaptable for industrial applications. While TXVR is a promising approach to translate XVR into industrial applications, we need several algorithmic improvements to increase the measurement speed.

We observed that only 3100 frames out of the 80000 recorded were used to obtain the results shown in this chapter. This implies that we can measure much faster by using a faster rotation motor. However, this would impose further restrictions on the camera frame rate and the maximum size of the sample that can be measured without inducing motion blur. Most of these issues can be addressed by improving the processing algorithm.

(a)　　　　　　　　　　　(b)
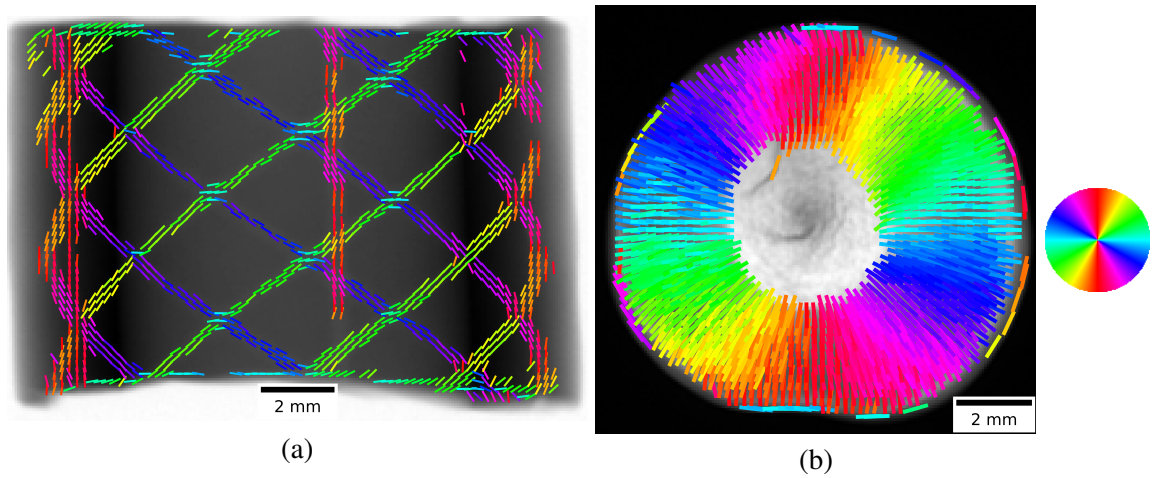
Figure 6.8: Examples of results obtained using TXVR. Two dimensional orientations $\gamma(p,q)$ (Eq. 6.16) are displayed as color coded unit vectors overlaid on the corresponding gray-scale attenuation image. Coloring is obtained by converting the value of $\gamma(p,q)$ to HSV (Hue, Saturation & Value) by setting hue equal to $\gamma(p,q)$, and saturation and value equal to 1 for all pixels; the colorwheel on the right should be used for interpreting the colors. (a) Orientations of nylon fibres embedded in a rubber pipe (half cut) calculated using TXVR. The grayscale for the attenuation image is set to $[0.29,1]$ and the orientation is shown in every 3rd pixel. (b) The orientations of gills inside the cap of a species of mushrooms found in East Asia overlaid on the attenuation image (grayscale values between $[0.06,1]$). Vectors in every 3rd pixel are shown.

(a)　　　　　　　　　　　(b)
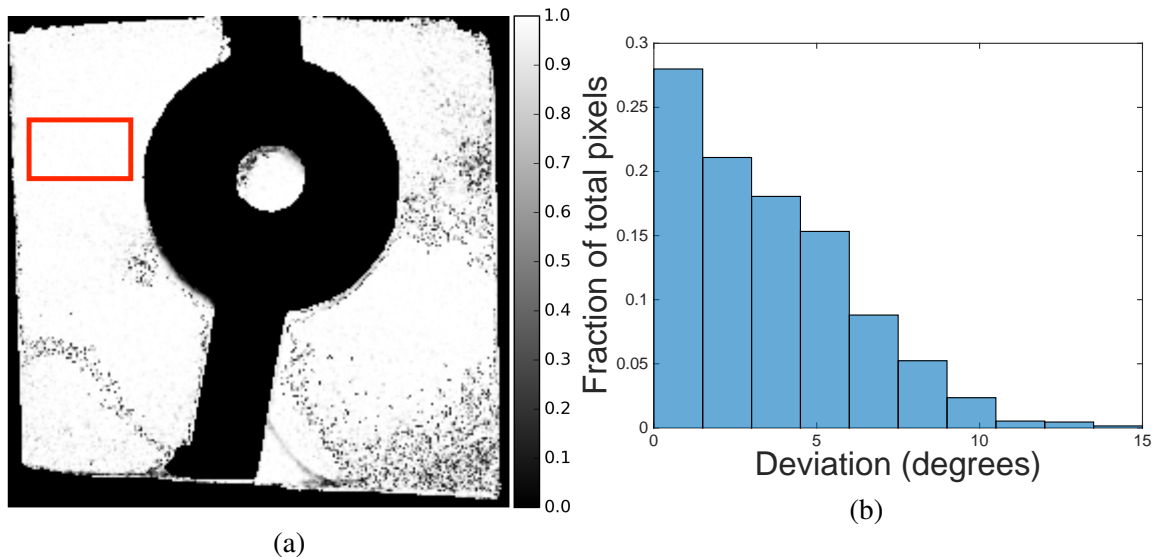
Figure 6.9: (a) Pair-wise dot product of the unit vectors in Figure 6.6(a) and (b). Brighter color implies the orientations calculated using TXVR and XVR are identical (b) Histogram of angular deviation between TXVR and XVR result inside a region of interest.

<div align="center">(a)   (b)</div>
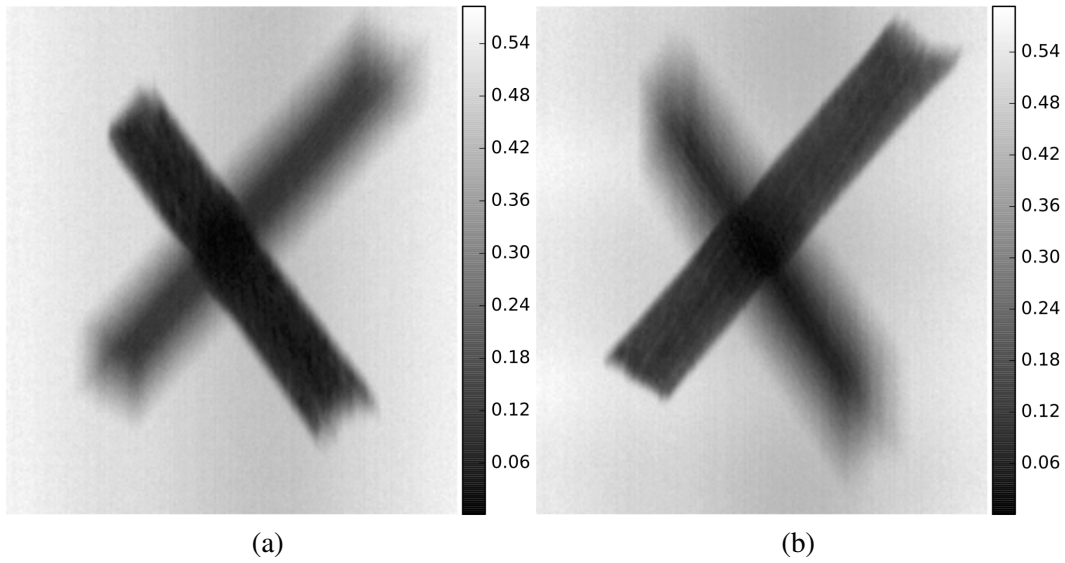
Figure 6.10: A sample consisting of two toothpicks separated in depth by approximately 7 cm. Dark-field images of the sample are obtained using the same data (only linear motion) but with two different velocities in the phase scanning step. We observe that we can focus on different planes inside the sample by selecting different velocities for phase scanning.

In this work, we took a significant step forward in simplifying the acquisition protocol for XVR by combining the conventional stepwise procedure into a continuous sample motion. Similarly, we can combine the two step algorithm in sections 6.3.1 and 6.3.2 to obtain a more robust algorithm. Moreover, we can incorporate the position dependent velocity variation discussed in section 6.6 in this model. This combined model can potentially result in significant improvements in the measurement speed. In addition, below we discuss a preliminary idea for potentially extending TXVR into the third dimension i.e. depth.

6.7.1   Towards Multi-slice TXVR

As an addition to this chapter, we also want to present some future possibilities with the setup shown in Figure 6.2. It can be seen in Eq. 6.12, 6.7 and 6.6 that the linear velocity of the sample is an important variable in the phase scanning step. The linear velocity u of the sample on the detector plane is further dependant on the magnification M. This implies that for the same set of parameters, moving the sample up and down in the vertical setup changes the value of u used for phase scanning. Or in other words, by selecting different values of u, we can focus on different heights inside the sample and obtain an effect similar to Depth-of-focus reconstruction in microscopy [Kang et al. (2015)].

We demonstrate this effect using a sample consisting of two wooden toothpicks, separated in height by approximately 7 cm. We measure this sample using only linear motion and perform phase scanning to obtain the dark-field images. We observe that by processing the same linear movie with two different velocities, we can focus on one of the the two toothpicks as shown in Figure 6.10. This principle of depth-of-focus scanning exists in other fields such as microscopy and computer

vision. Advanced algorithms [Nayar and Nakagawa (1994)] can be used to deconvolve the focussed objects from the out-of-focus regions of the image. We believe that combining this depth-of-focus approach with TXVR may allow us to perform a multi-slice TXVR where in we can resolve structure orientations in multiple slices within the sample. This method could be especially useful for composite materials comprising of multi-layered arrangements of fibres.

Chapter 7

Coverage Metric and Sparse Acquisition Schemes

Parts of this chapter have been published as:
Sharma, Y., Wieczorek, M., Schaff, F., Seyyedi, S., Prade, F., Pfeiffer, F., and Lasser, T. (2016).
Six dimensional x-ray tensor tomography with a compact laboratory setup. Applied Physics
Letters, 109(13):134102.

We reviewed two methods for Anisotropic X-ray Dark-field (AXDF) tomography in Chapter 5, namely X-ray Tensor Tomograhy (XTT) and Anisotropic X-ray Dark-field Tomography (AXDT). We saw that owing to the directional dependence of the dark-field signal, the forward model (Eq. 5.1) for dark-field tomography comprises of a pose-dependent weight factor (Eq. 5.2). Because of these additional weights in the forward model, conventional CT acquisitions schemes are not sufficient for dark-field tomography. Malecki et al. (2014) extended the idea of circular trajectory in CT (section 3.3.1) to dark-field tomography by employing additional circular trajectories resulting in an acquisition scheme spread over a sphere instead of a circle. Figure 7.1 shows the basic idea of such a scheme, wherein we sample the unit sphere of orientations instead of a circle.

In order to reach the poses depicted in Figure 7.1, we require three rotation axes. This is achieved by placing the sample on an eulerian cradle, same as the one used for XVR (Figure 6.1(b)). Schematic of a grating interferometry setup with an eulerian cradle is shown in Figure 7.3. Requirement of large number of poses and rotation around three axes to reach every pose results in a long acquisition time for AXDF tomography. The requirement of the cradle and long acquisition time are significant hurdles for the practical applications of dark-field tomography. It is, therefore, necessary to design sparse acquisition schemes for these methods, which is the goal of this chapter.

In order to acheive the aforementioned objective, we first begin with visualizing XTT acquisition schemes in section 7.1. While the visualization method helps us better understand the schemes, it is not enough to quantify them. In section 7.2, we present a numerical method to predict the efficacy of XTT acquisition schemes. Next, we combine this predictive measure with an experimental measure

of performance in section 7.3, in order to validate the applicability of the numerical method. Finally, we test different acquisition schemes using the two metrics with the goal of reducing the time and hardware complexity of XTT acquisition. We present experimental results for two samples in section 7.4 and draw conclusions in section 7.5.

7.1 Acquisition Schemes for XTT

In order to sample the unit sphere as shown in Figue 7.1, we require three axes of rotation shown in Figure 7.3. Defining the world coordinates as x, y, z and the sample coordinate system as x', y', z', the three angles of rotation are defined as:

1. ψ - rotation around the y axis

2. θ - rotation around the z' axis

3. ψ - rotation around the y' axis

A sample pose $x := (\psi, \theta, \phi)$ is defined by rotating around the corresponding axes in the order-ψ, θ, ϕ. The resulting rotation matrix (see Appendix A) is:

$$R(x) = R_y(\psi) \cdot R_z(\theta) \cdot R_y(\phi) =$$

$$\begin{bmatrix} \cos\psi\cos\theta\cos\phi - \sin\psi\sin\phi & -\cos\psi\sin\theta & \cos\psi\cos\theta\sin\phi + \sin\psi\cos\phi \\ \sin\theta\cos\phi & \cos\theta & \sin\theta\sin\phi \\ -\sin\psi\cos\theta\cos\phi - \cos\psi\sin\phi & \sin\psi\sin\theta & -\sin\psi\cos\theta\sin\phi + \cos\psi\cos\phi. \end{bmatrix} \quad (7.1)$$

The weight factor (Eq.5.2) models the anisotropic property of the dark-field signal in terms of the tomographic and sensitivity axes. Therefore, in order to understand the acquisition schemes, it is essential to look at the trajectories of these two axes. We have done this before, in the case of conventional CT in Figure 3.5 and for the case of XVR in Figure 6.1. In the former case, sensitivity axis plays no role. In the latter case, we sample several sensitivity points, however, the optical axes remains invariant since we do not perform tomography. In the case of XTT, both the axes play an important role as we will discuss in this section.

Let us begin with an example tomographic trajectory rotating about y' as a function of ψ and θ:

$$A(\psi, \theta) := \left\{ x := (\psi, \theta, \phi); \ \phi \in [0°, 18.95°, \ldots, 360°] \right\}.$$

A common sparse acquisition scheme for conventional CT using 20 equally spaced projection angles is then expressed as $A(0°, 0°)$. In other words, the sample is rotated around the fixed y axis and line integrals through the sample along z, also known as the optical axis, are recorded. For visualization, we plot $\pm t(x)$ on a unit sphere, assuming that the sample is fixed at the center of the sphere. The points $\pm t(x)$ for $A(0°, 0°)$ are shown in blue in Figure 7.2(a). We have $S = y$ when the grating bars are horizontal. Assuming again that the sample is fixed at the center of a sphere, we also plot $\pm s(x)$ on the
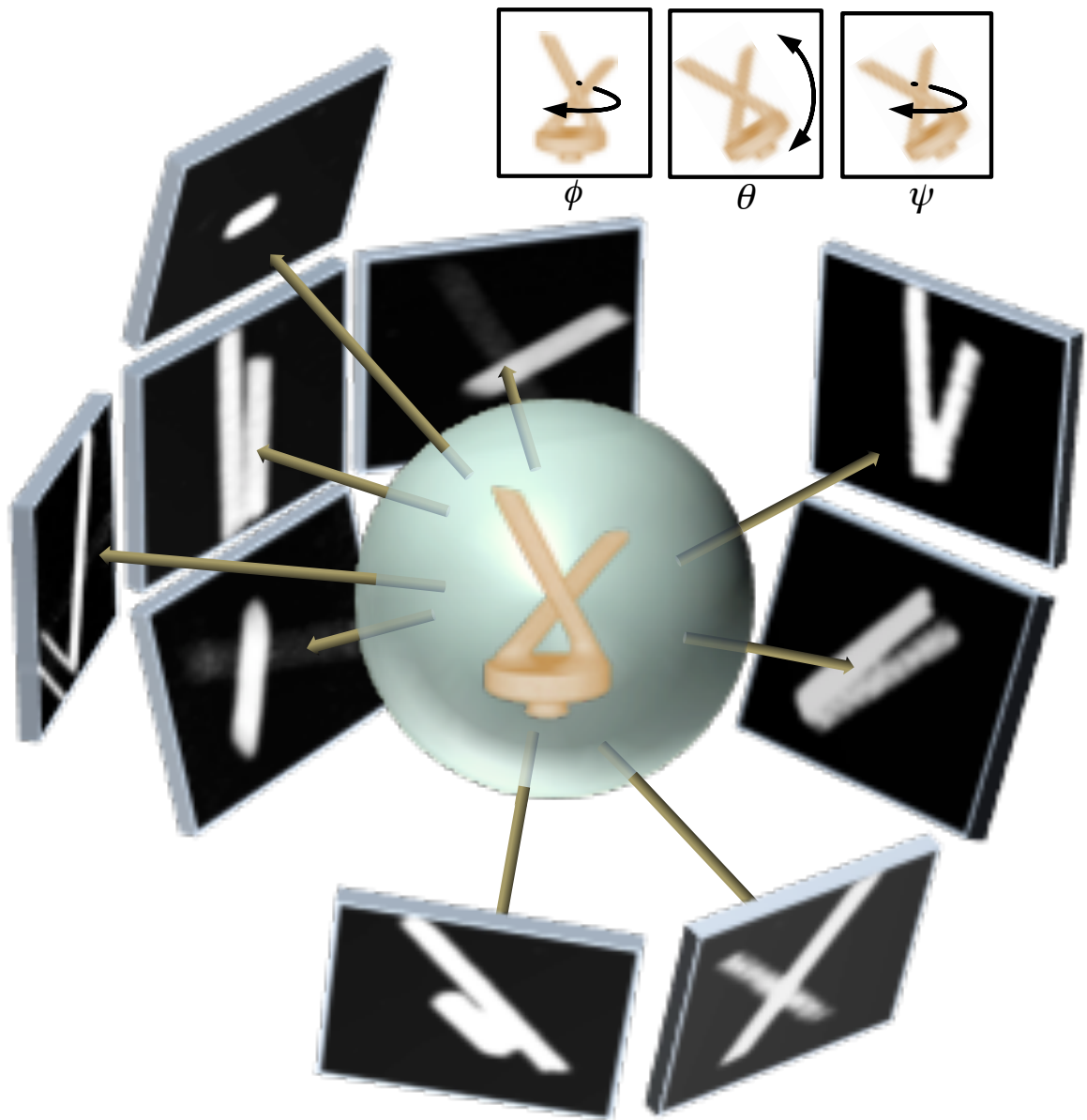
Figure 7.1: XTT acquisition scheme spread over the unit sphere. Figure by Sharma et al. (2016) is licensed under CC BY 4.0.

(a) $A(0°,0°)$ (b) $A(20°,45°)$ (c) $A(40°,45°)$ (d) $A(40°,90°)$
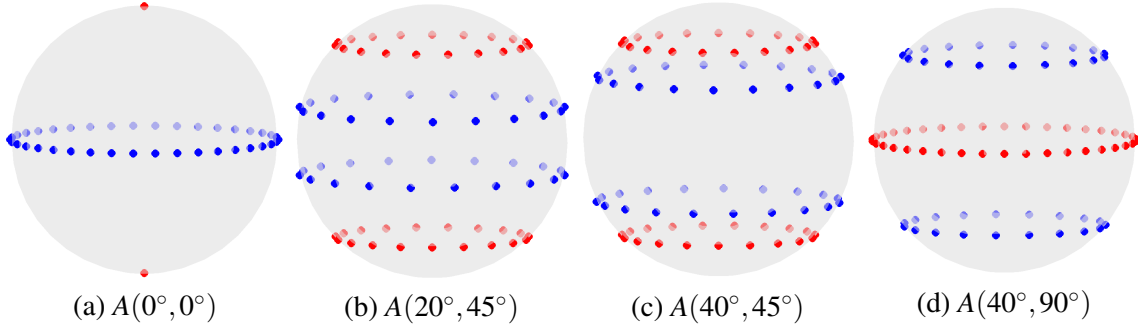
Figure 7.2: Spherical representation of acquisition scheme $A(\psi,\theta)$ for different combinations of ψ and θ. On each sphere, blue points represent the trajectories of the optical axis $\pm t(x)$ and red points represent the trajectories of the sensitivity axis $\pm s(x)$ assuming that the sample is fixed at the center of the sphere. Figure by Sharma et al. (2016) is licensed under CC BY 4.0.

unit sphere. The points $\pm s(x)$ for $A(0°,0°)$ are shown in red in Figure 7.2(a). It can be seen that only one direction of scattering can be measured with $A(0°,0°)$. This means that a standard CT acquisition trajectory is not sufficient for an XTT measurement. Therefore, additional tomographic trajectories for XTT (as shown in Figure 7.2) are obtained by rotating y' using ψ and θ. The visualization of the trajectories of the optical axis $t(x)$ and sensitivity axis $s(x)$ shown in Figure 7.2 gives a qualitative understanding of the orientations that are measured with a given acquisition scheme. In the next section, we present a method for the quantification of such acquisition schemes.

7.2   Coverage Metric (CM)

Let Σ and $\mathscr{T}$ be two sets of evenly distributed points chosen from a hemisphere:

$$\Sigma = \{\sigma_k,\ k = 1,2,\dots,N\},$$
$$\mathscr{T} = \{\tau_j,\ j = 1,2,\dots,N\},$$

where $N = 4843$. The mean vector of Σ is given by:

$$m_\Sigma = \frac{1}{N}\sum_{k=1}^{N}\sigma_k.$$

Let X be an acquisition scheme using n different acquisition poses x_i:

$$X := \{x_i := (\psi_i,\theta_i,\phi_i);\ i = 1,\dots,n\}.$$

The objective is to define a quantity, $Coverage(X,k)$ that represents how well the orientation $\sigma_k \in \Sigma$ is measured by X. Our proposed procedure for computing $Coverage(X,k)$ is outlined in the following.

1. Define $X_k \subset X$ as the set of poses that measure the orientation $\sigma_k \in \Sigma$:

$$X_k := \left\{ x \in X; \ w(\sigma_k, x) > T_c \right\},$$

where $w(\sigma_k, x)$ is the weight factor that specifies how well the orientation σ_k is measured by the acquisition pose x, and $T_c = 0.7$ is an arbitrarily chosen threshold. It was already defined in Eq. 5.2. Below, we reiterate the definition of $w(\sigma_k, x)$:

$$w(\sigma_k, x) = \left(\left| \sigma_k \times t(x) \right| \left\langle \sigma_k, s(x) \right\rangle \right)^2, \tag{7.2}$$

where $| \cdot \times \cdot |$ denotes the magnitude of the cross product and $\langle \cdot, \cdot \rangle$ denotes the standard scalar product.

2. R_k is the mean resulting length of the vectors $t(x)$ for all $x \in X_k$,

$$R_k = \left\| \frac{1}{|X_k|} \sum_{x \in X_k} t(x) \right\|,$$

where $\| \cdot \|$ denotes the Euclidean length of a vector.

3. $\mathscr{T}_k \subset \mathscr{T}$ is the set of points that are measured by X_k, assuming that each vector $t(x)$ contributes to the measurement of points lying within a cone of opening angle $5°$ around it:

$$\mathscr{T}_k := \left\{ \tau \in \mathscr{T}; \ \langle \tau, t(x) \rangle > \cos(2.5°) \ \forall x \in X_k \right\}.$$

4. The $Coverage(X, k)$ is then defined as:

$$Coverage(X, k) := 2 \times (1 - R_k) \times \frac{|\mathscr{T}_k|}{N}.$$

The quantity $2 \times (1 - R_k)$ is the spherical variance [Mardia and Jupp (2008)], while $|\mathscr{T}_k|/N$ is related to the cumulative solid angle spanned by the $t(x)$, $x \in X_k$. Thus, a higher value of $Coverage(X, k)$ is achieved when the $t(x)$ are distributed widely over the unit sphere.

Next, we scale the unit vectors $\sigma_k \in \Sigma$ with the values of $Coverage(X, k)$ for all values of k resulting in:

$$\Gamma(X) := \left\{ \gamma_k := \sigma_k \times Coverage(X, k), \ k = 1, \dots, N \right\},$$

and its mean:

$$m_{\Gamma(X)} = \frac{1}{N} \sum_{k=1}^{N} \gamma_k.$$

The angular deviation of the normalized mean vector $\widehat{m}_{\Gamma(X)}$ from the normalized mean vector $\widehat{m}_{\Sigma}$ is a measure of the non-uniformity of the Coverage Sphere. Finally, we can now introduce the Coverage

Metric $CM(X)$ as:

$$CM(X) := \langle \widehat{m}_{\Gamma(X)}, \widehat{m}_{\Sigma} \rangle \times \frac{1}{N} \sum_{k=1}^{N} Coverage(X,k).$$

$CM(X) \in [0,1]$ is a measure of the efficiency of the acquisition protocol X. Higher values of CM imply a more comprehensive and uniform measurement of all orientations on the unit sphere.

7.3 Performance Metric (PM)

In the last section, we derived a numerical method to quantify the efficacy of an XTT acquisition scheme. In order to correlate this metric with experimental results, we define an experimental metric and call it the Performance Metric (PM). The goal of this metric is to quantify the result of a scheme X with respect to a standard scheme S. Hence, we need a metric to quantify the difference in the result, which in this case is a tensor.

Riemannian manifold Sym_3^+, i.e. the manifold of positive-definite symmetric matrices, provides us tools for comparison on tensors. One such tool is a Riemannian metric [Pennec et al. (2006)] or the distance $d : \mathrm{Sym}_3^+ \times \mathrm{Sym}_3^+ \to \mathbb{R}_+$ between two tensors $T_1, T_2 \in \mathrm{Sym}_3^+$ on this manifold. It is computed as:

$$d(T_1, T_2) = \sqrt{\sum_{i=1}^{3} \log(\lambda_i)^2},$$

where λ_i denotes the i-th eigenvalue of the matrix $T_1^{-\frac{1}{2}} T_2 T_1^{-\frac{1}{2}}$. We refer the reader to Wieczorek (2017) for a detailed description of this metric.

Let us consider a XTT volume consisting of I voxels r_i, $i = 1 \cdots I$. We reconstruct it using two different acquisition schemes X and S and obtain corresponding tensors $T_X(r_i)$ and $T_S(r_i)$ in the ith voxel. These two tensors are considered to be correlated if $d(T_X(r_i), T_S(r_i))$ is less than a certain threshold T_p. Based on this, we introduce a Performance Metric $PM(X)$, which determines how well the acquisition scheme X performs with respect to S:

$$PM(X) = \frac{\left| \{ r_i;\, d(T_X(r_i), T_S(r_i)) < T_p,\, i = 1, \ldots, I \} \right|}{I},$$

where $T_p = 0.4$ and $|\cdot|$ is the number of elements in a set.

7.4 Experiments and Results

In this section, we use the two metrics described above to assess the time and hardware complexity of different acquisition schemes. We measure two fibre composite samples using the setup described in the next section and perform XTT reconstruction using the algorithm described in section 5.1. We use an oversampled acquisition scheme S to measure the samples and obtain a baseline standard reconstruction. Next, we perform reconstructions with different downsampled versions of the acquisition
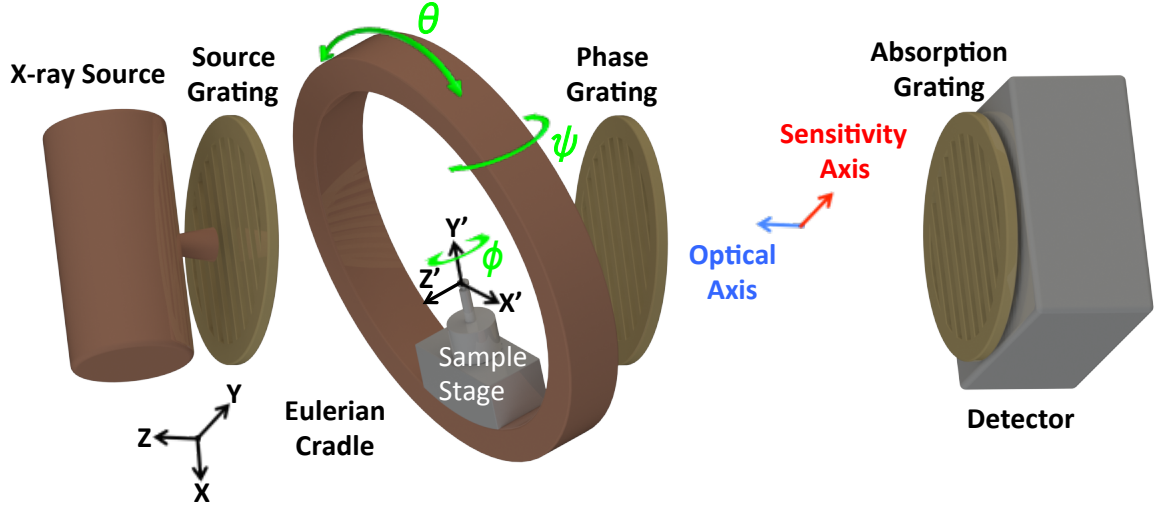
Figure 7.3: Setup used for AXDF tomography. Figure by Sharma et al. (2016) is licensed under CC BY 4.0.

Grating	G0	G1	G2
Type	absorption	$\pi/2$ phase-shift	absorption
Lamellae	Gold	Nickel	Gold
Period(μm)	10	5	10
Duty Cycle	0.5	0.5	0.5
Material Height(μm)	160-170	8	160-170

Table 7.1: Gratings used for the XTT setup shown in Figure 7.3.

schemes and compare the results to the standard result using the Performance Metric described in section 7.3. Separately, we calculate the coverage metric (section 7.2) for the downsampled schemes. By demonstrating an agreement between the numerical and experimental metric, we establish the validity of our proposed coverage metric. Finally, we use CM to design optimal acquisition schemes in order to reduce the time and hardware complexity of XTT setups. We discuss the acquisition schemes and corresponding results for both the samples in separate subsections.

7.4.1 Setup

We use the setup shown in Figure 7.3. It consists of a X-ray tube XWT-160-SE from X-ray Worx Gmbh, with acceleration voltages between 10-160 kV, maximum power of 300 W and a tungsten anode. It is a microfocus X-ray tube with a spot size which increases from 4 μm to more than 100 μm when operated at the lowest and the highest power, respectively. The source opening half-angle is $15°$. We use a flat panel PaxScan 2520DX detector from Varian medical systems with a 600 μm thick layer of columnar structured cesium iodide as the scintillator. The physical pixel size is 127×127 μm with a total of 1920×1536 pixels. We usually operate at 1 fps, however, frame rates of 0.5-12.5 fps are
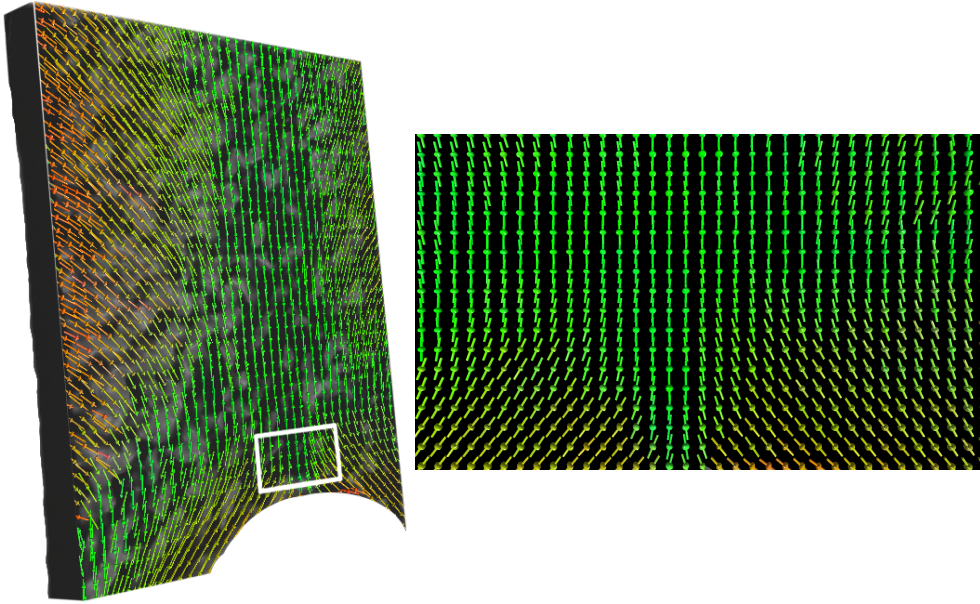
Figure 7.4: XTT reconstruction of a SFRP sample. Tensors and their smallest half axis in a slice is shown overlaid on the corresponding attenuation volume. A region-of-interest is shown on the right.

available. Three gratings, as described in Table 7.4.1, are placed between the source and the detector. We assume a symmetric interferometer in the first fractional Talbot configuration for a design energy of 45 keV, resulting in an Inter-grating distances of 92.7 cm.

7.4.2   Sample 1- Short Fibre Reinforced Polymer (SFRP)

We analyze a Short fibre Reinforced Polymer (SFRP) sample made of glass fibres (18 μm in diameter). SFRPs are widely used in the automotive industry for their improved mechanical properties which depend heavily on the orientation and length distribution of the reinforcing carbon or glass fibres. A very high resolution XCT combined with fibre tracking techniques is commonly used to analyze the fibre orientation distribution of such materials. XTT is a very useful technique for these materials as it directly resolves the orientations of the fibres within a much larger sample size. We measure a SFRP sample (dimensions $10 \times 10 \times 2$ mm) in the setup shown in Figure 7.3.

The sample was measured with a standard XTT acquisition scheme as first introduced by Malecki et al. (2014):

$$
\begin{aligned}
S = \big\{ s := (\psi, \theta, \phi); \; & \psi \in [0°, 20°, 40°], \\
& \theta \in [0°, 30°, 60°, 90°], \\
& \phi \in [0°, 2.01°, \ldots, 360°] \big\}.
\end{aligned}
\tag{7.3}
$$

Scheme S comprising of 2160 poses is shown in Figure 7.6(a). The dark-field signal at every pose $d(x)$ (Eq. 5.10) was measured using 7 phase steps and 3 secs exposure per phase step resulting in a total

$$B(4.2) = S_3, PM = 0.88$$

(a)

$$B(4.2) = S_3 \qquad B(1.6)$$
$$CM = 0.76 \qquad CM = 0.38$$
(b)

$$B(1.6), PM = 0.61$$
(c)
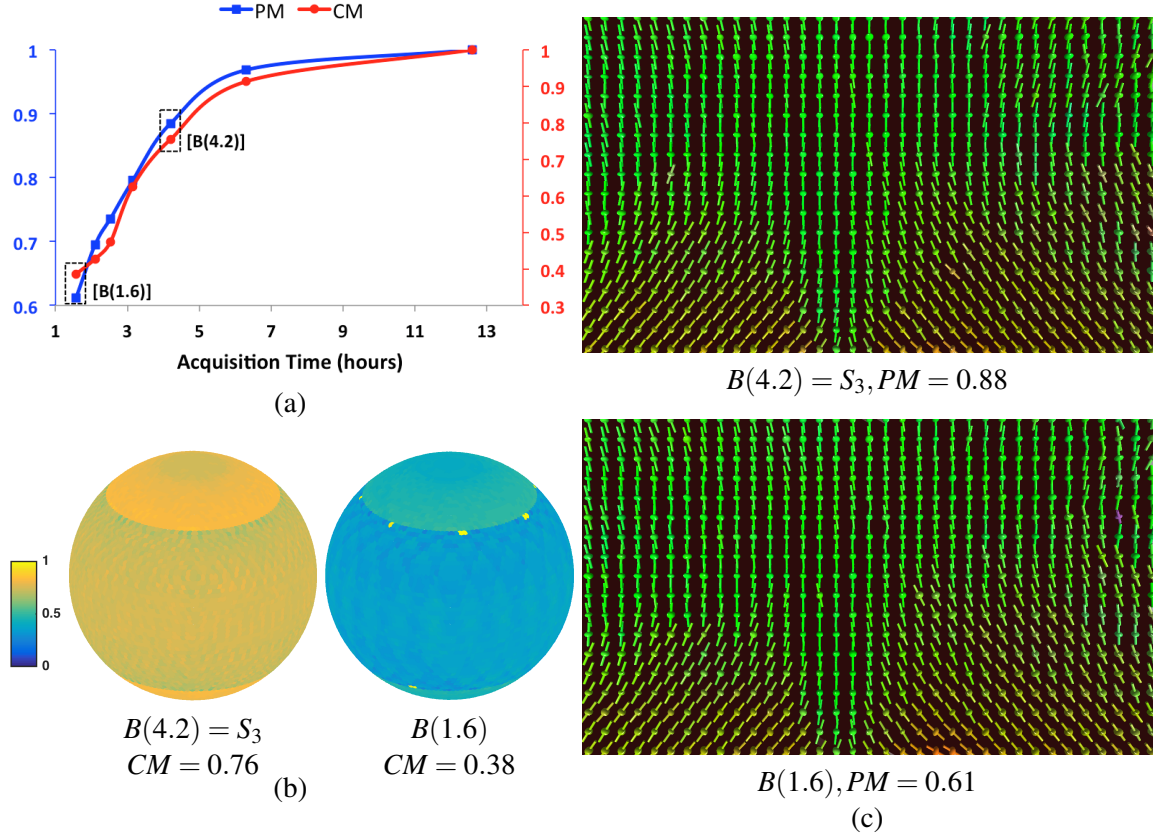
Figure 7.5: Time Complexity Analysis for SFRP sample. (a) Plot of CM and PM versus the acquisition time (b) Coverage Spheres for two acquisition schemes highlighted in (a). (c) XTT reconstruction in the region of interest shown in Figure 7.4 obtained using the two schemes.

acquisition time of approximately 12.6 hours. We calculate scattering tensors $T_S(r_i) \in \mathbb{R}_+^{3 \times 3}$ for voxels r_i, $i = 1, \dots, I$, discretizing the volume of interest (isotropic voxel size 64 μm^3) using the method presented in section 5.1; the subscript (here S) indicates the acquisition protocol used to compute the scattering tensors. Figure 7.4(a) shows the scattering tensors $T_S(r_i)$ along with the corresponding structure orientation, overlaid on the CT volume of the sample. The tensors are color coded with their orientation. It is evident from Figure 7.4(a) that XTT reveals the three dimensional orientations of fibres in this sample. The resulting fibre orientations are comparable qualitatively to the fibre tracking results presented by Hannesschlager et al. (2015), where they used a voxel size of 6.5 μm^3. Below, we study the effect of reducing the time and hardware complexity of the acquisition scheme (Eq. 7.3).

Effect of Time Complexity

We define seven acquisition schemes $B(t)$ by downsampling S to reduce the acquisition time to t hours while using all three axes of rotation:

$$B(t) = \left\{ s_{(k-1) \times \frac{T}{t}}; \ k = 1, 2, \dots, 2160 \times t/T \right\}, \tag{7.4}$$

(a) S (b) S_3 (c) S_2 (d) S_1
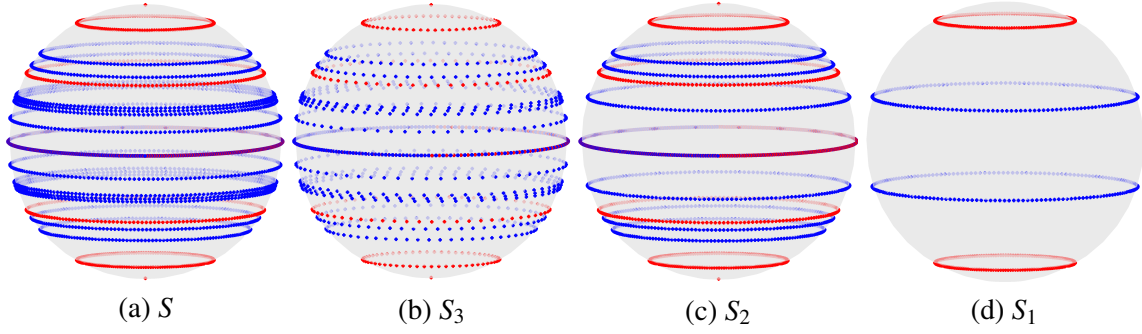
Figure 7.6: (a) Spherical representation for standard scheme XTT scheme S used in this study. (b-d) Downsampled scheme with 3, 2 and 1 axes of rotations, respectively.

where $T = 12.6$ hours is the acquisition time for scheme S. *CM* and *PM* for $B(t)$ are plotted against t in Figure 7.5(a). We pick two points $B(4.2)$ and $B(1.6)$ from Figure 7.5(a) and show the reconstructed result in Figure 7.5(c) and corresponding Coverage Spheres in Figure 7.5(b). It can be seen that $B(4.2)$ provides a uniform Coverage Sphere comprised of high values, thus leading to a good quality of the result.

Effect of Hardware Complexity

Hardware complexity is induced by the Eulerian cradle, which is required to provide the two additional axes of rotation (ψ and θ). Therefore, in this study, we begin with the acquisition scheme $B(4.2)$ as representative of a complex setup employing 3 rotation axes and rename it S_3, the subscript here indicating the number of rotation axes. Next, we remove rotation axes in steps to obtain the schemes S_2 and S_1. The four schemes S, S_3, S_2 and S_1 are shown in Figure 7.6. Scheme S_2 represents a medium complexity setup employing two rotation axes with fixed ψ (optimally chosen using *CM*), while scheme S_1 represents a simple setup employing only one rotation axis (fixed ψ and θ):

$$S_2 = \big\{(\psi, \theta, \phi); \ \psi = 40°, \theta \in \Theta, \phi \in \Phi\big\},$$
$$S_1 = \big\{(\psi, \theta, \phi); \ \psi = 40°, \theta = 30°, \phi \in \Phi\big\}.$$

The Coverage Spheres for S_2 and S_1 are shown in Figure 7.7(b) and the reconstructed tensors are shown in Figure 7.7(c). The plot of *CM* and *PM* versus the number of rotation axes is shown in Figure 7.7(a). It can be seen that the quality of the reconstruction deteriorates slightly but not enough to affect their interpretation in an application when only a single value of ψ is used (i.e. a medium complexity setup using two rotation axes). However, using a simple setup with just one rotation axis and fixed ψ, θ (scheme S_1), markedly deteriorates the quality of the reconstructions.

7.4.3 Sample 2 - Carbon Fibre Reinforced Polymer (CFRP)

In this section, we present similar results as before, but for a Carbon fibre Reinforced Polymer (CFRP) specimen. This sample has sharp discontinuities in structure orientation, making it more challenging
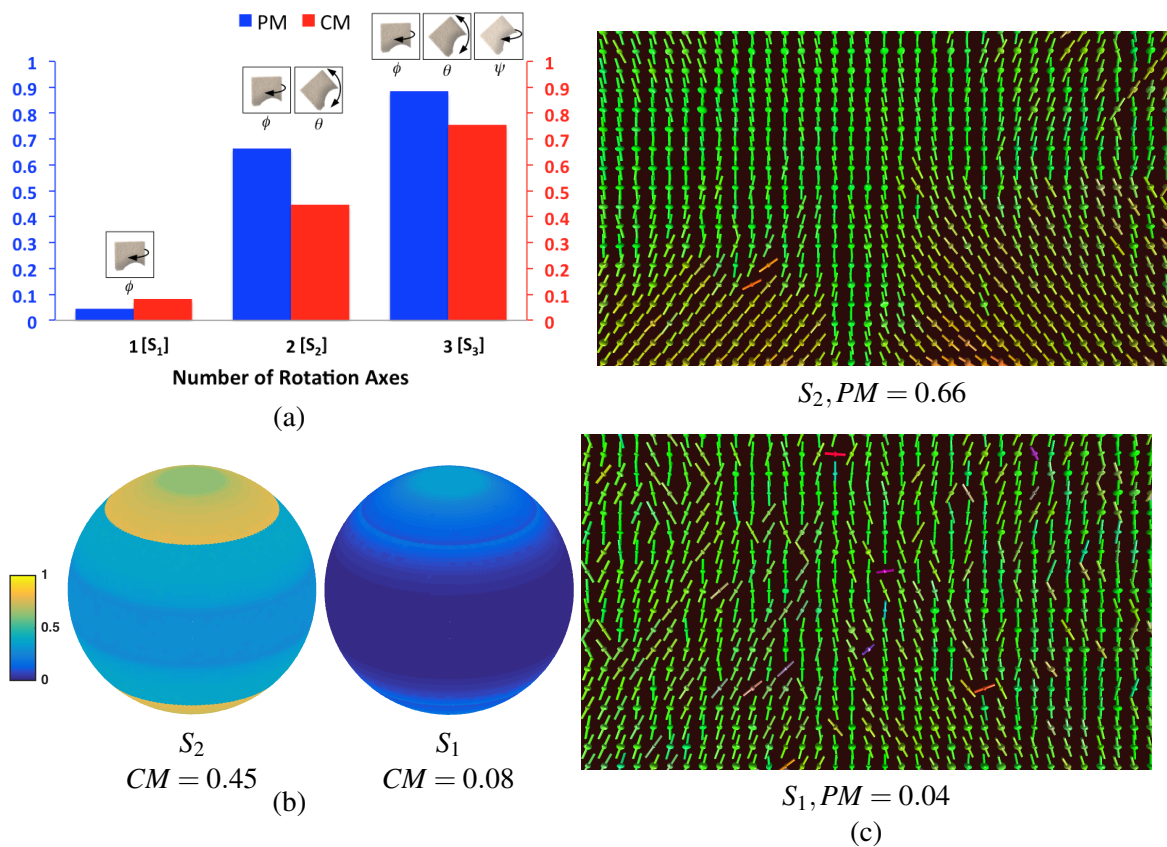
Figure 7.7: Effect of Hardware Complexity for the SFRP sample (a) Plot of PM and CM versus acquisition schemes with 3,2 and 1 axes of rotations. (b) Coverage Spheres for S_2 and S_1, S_3 is shown in Figure 7.5(b). (c) Corresponding XTT reconstruction results in a region of interest.
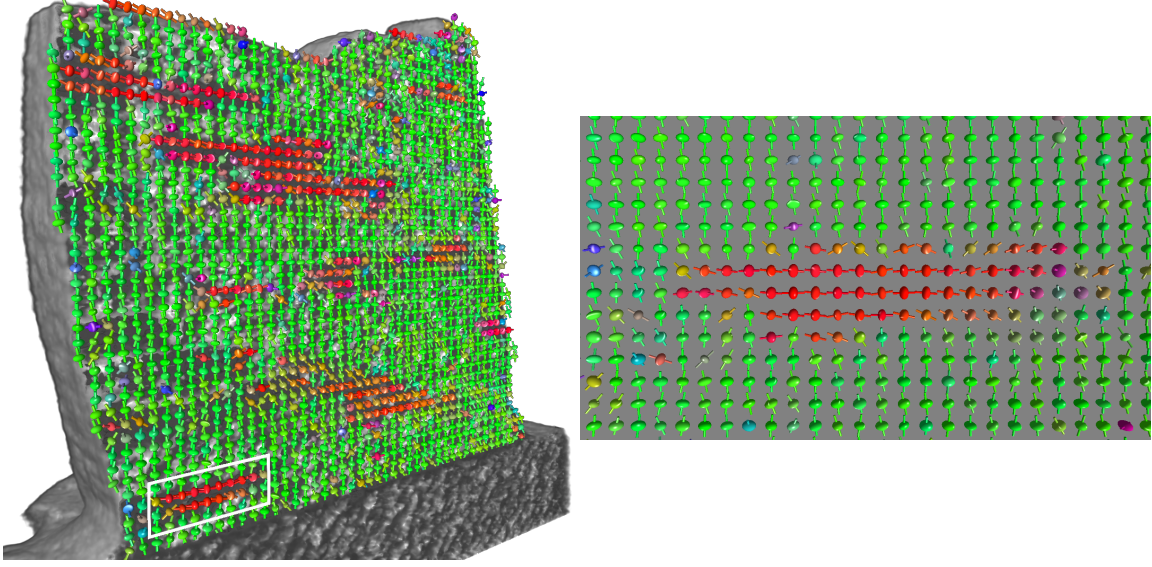
Figure 7.8: XTT result for the CFRP sample. Tensors and their smallest half-axes in one slice are overlaid on the attenuation volume. A region-of-interest is shown on the right.

compared to the previous sample, which has a smooth arrangement of fibres due to the injection molding process. We perform a XTT measurement using a densely sampled acquisition protocol S with 2700 poses,

$$S = \big\{ s := (\psi, \theta, \phi); \; \psi \in [0°, 20°, 40°],$$
$$\theta \in [0°, 11.25°, \dots, 90°],$$
$$\phi \in [0°, 3.636°, \dots, 360°] \big\}$$

in a continuous measurement spanning 30 hours, with 8 phase steps and $5s$ exposure per step.

Figure 7.8(a) shows the scattering tensors $T_S(r_i)$ along with the corresponding structure orientation, overlaid on the X-ray absorption volume. Region of Interest is shown in 7.8(b). The tensors are color coded using their orientation. It can be seen that XTT is able to successfully reconstruct the orientations of the carbon fibres in this sample comprising of uni-directional laminates (green) joined together with pieces of orthogonal connecting fibres (red).

Effect of Time Complexity

Several acquisition schemes $B(t)$ are defined by downsampling S to achieve an acquisition time of t hours:

$$B(t) = \big\{ b_{(k-1)\cdot\frac{T}{t}}; \; k = 1, 2, \dots, 2700 \cdot t/T \big\},$$

where $T = 30$ hours is the acquisition time required for scheme S. *CM* and *PM* for $B(t)$ are plotted against t in Figure 7.9(a). We pick two points $B(10)$ and $B(2)$ from Figure 7.9(a) and show the reconstructed result in Figure 7.9(c) and the corresponding Coverage Spheres in Figure 7.9(b). It can
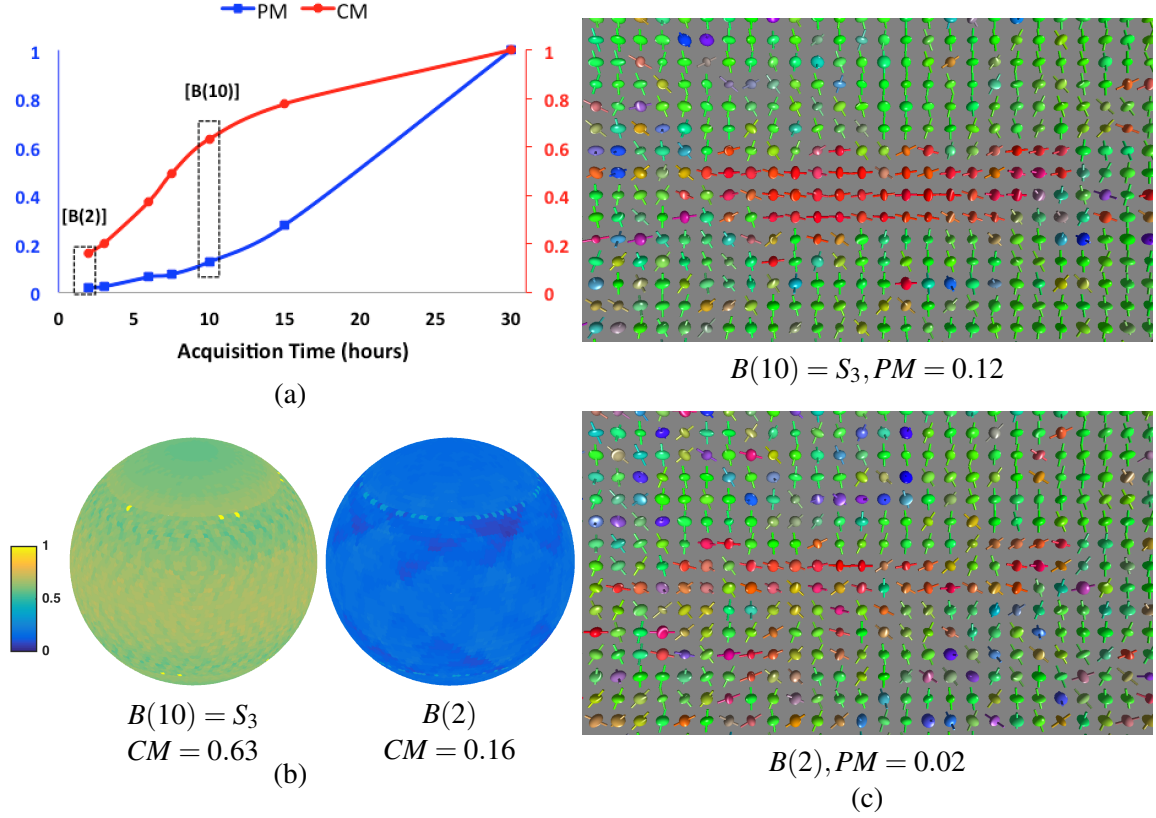
Figure 7.9: Time Complexity Analysis for CFRP sample. (a) Plot of CM and PM versus the acquisition time (b) Coverage Spheres for two acquisition schemes highlighted in (a). (c) XTT reconstruction in the region of interest shown in Figure 7.8 obtained using the two schemes.

be seen that acquisition time has a significant detrimental effect on both the *CM* and *PM* which is also evident in the ROIs shown in Figure 7.9(c).

Effect of Hardware Complexity

We begin with the acquisition scheme $B(10)$ as representative of a complex setup employing 3 rotation axes and rename it S_3, the subscript here indicating the number of rotation axes. Next, we remove rotation axes in steps to obtain the schemes S_2 and S_1. Scheme S_2 represents a medium complexity setup employing two rotation axes with fixed ψ (optimally chosen using *CM*), while scheme S_1 represents a simple setup employing only one rotation axis (fixed ψ and θ):

$$S_2 = \{(\psi, \theta, \phi); \ \psi = 40°, \theta \in \Theta, \phi \in \Phi\},$$
$$S_1 = \{(\psi, \theta, \phi); \ \psi = 40°, \theta = 45°, \phi \in [0°, 0.4°, \dots, 360°]\},$$

The Coverage Spheres for S_2 and S_1 are shown in Figure 7.10(b) and the reconstructed tensors are shown in Figure 7.10(c). The plot of *CM* and *PM* versus the number of rotation axes is shown in Figure 7.10(a). It can be seen that the quality of the reconstruction for S_2 (scheme using 2 axes

(a)

(b)

S_2
$CM = 0.48$

S_1
$CM = 0.03$

$S_2, PM = 0.06$

$S_1, PM = 0.01$

(c)
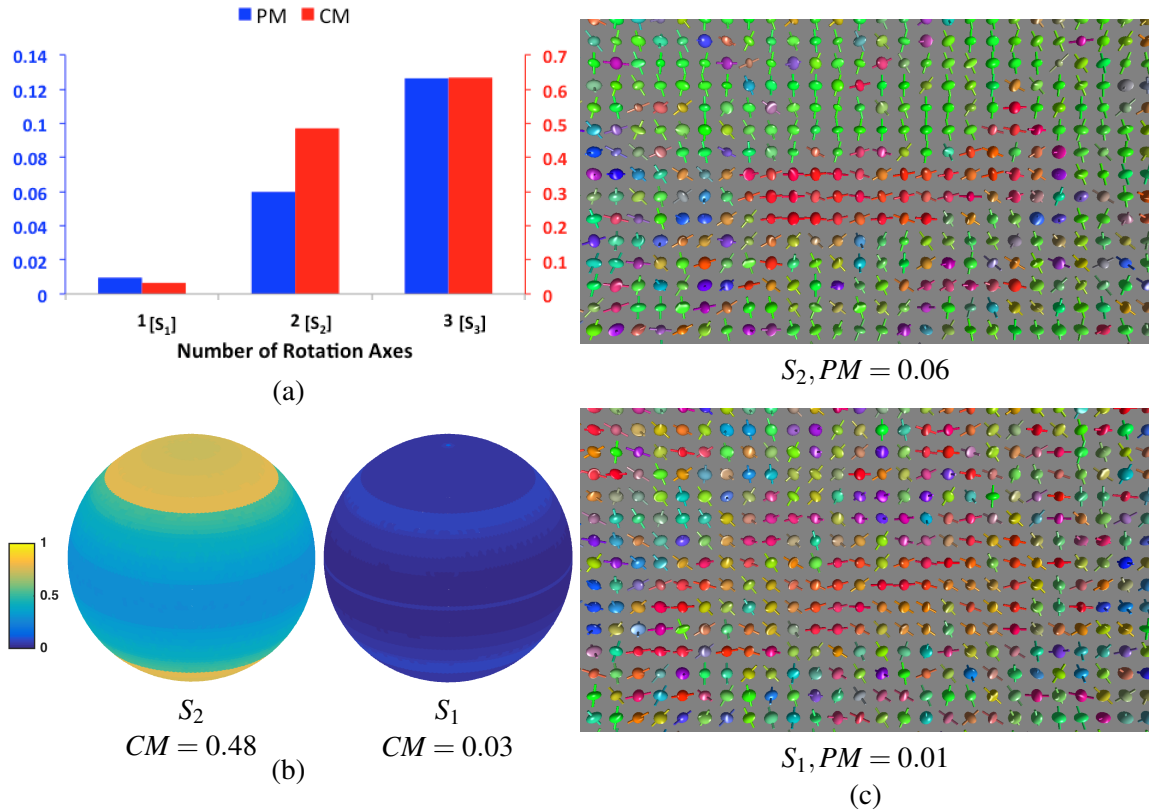
Figure 7.10: Effect of Hardware Complexity for the CFRP sample (a) Plot of PM and CM versus acquisition schemes with 3,2 and 1 axes of rotations. (b) Coverage Spheres for S_2 and S_1, S_3 is shown in Figure 7.9(b). (c) Corresponding XTT reconstruction results in a region of interest.

of rotation) is a reasonable compromise when compared to $S_3 = B(10)$ (scheme using 3 axes of rotations).

7.5   Discussion

So far, we presented a detailed description of XTT acquisition schemes and evaluated several schemes numerically and experimentally. We compared sparse acquisition schemes to oversampled schemes for two different samples. Since the first sample is manufactured using injection molding, the resulting orientation of glass fibres is smooth as can be seen in Figure 7.7. On the other hand, the second sample consists of a layered structure of uni-directional carbon fibres with orthogonal connecting fibres. Clearly, this kind of structure is more challenging for XTT because of the discontinuities and higher density of carbon fibres. While the oversampled scheme is able to resolve the complicated structure of the second sample, we start loosing quality as soon as we start downsampling. For both studies of time and hardware complexity on both samples, we observe a strong correlation between the numerical and experimental metrics. This implies that the coverage metric is a valid criterion

to design and assess XTT acquisition schemes. Below, we discuss the effect of time and hardware complexity for both the samples.

7.5.1   Effect of Time Complexity

In order to observe the effect of acquisition time on the result of XTT reconstruction, we compared several schemes with decreasing acquisition time while maintaining the same hardware complexity. From Figures 7.5 and 7.9, we observe that reduction in the acquisition time has a detrimental effect on the reconstruction quality. However, for both the samples, reduction in acquisition time by a factor of 3 does not harm the interpretation of the results. Further reduction in time is, however, not desirable. While we start loosing accuracy in the SFRP sample with an acquisition time of 1.6 hrs, the result for the CFRP sample is almost unusable at an acquisition time of 2 hours. The deterioration rate is also evident in the corresponding trends of *CM*. This implies that the *CM* can be used in the future to decide the minimum acquisition time required for task-specific XTT measurements.

7.5.2   Effect of Hardware Complexity

The bulky Eulerian cradle (Figure 7.3) required for the additional axes of rotation poses significant challenges for practical applications of XTT. Moreover, the time for motor movements, specifically the ψ and θ motors adds significant overhead to the total measurement time. Therefore, it is essential to reduce the number of rotation axes for practical applications of XTT. We studied the effect of the number of rotation axes for XTT. Specifically, we designed three acquisition schemes with similar measurement time, but decreasing number of rotation axes required to implement these schemes.

We observe, in both the samples, that decreasing the number of rotation axes leads to deterioration in the quality of the result, as evidenced from the corresponding values of *CM* and *PM*. However, we note that the results obtained using the scheme S_2 is reasonable comparable to the results obtained with the scheme S_3. Feature specific interpretation of the result does not change significantly between the two cases. However, reducing the axes of rotation to a single axis results in a complete loss of information. This is expected, because in this case we are essentially measuring only two circular trajectories as can be seen in Figure 7.6(d).

Owing to these observations, we conclude that a XTT setup with only two axes of rotation is viable, especially for commercial applications. Further advancements in the processing algorithms might help increase the quality of the result in comparison to those obtained with 3 rotation axes.

7.6   Summary

X-ray Tensor Tomography is a novel imaging modality with potential applications in material science and medicine. We had provided a detailed overview of the XTT reconstruction methodology, which was developed primarily by Malecki et al. (2014) and Vogel et al. (2015) in Chapter 5. In this chapter, we provided a detailed visual, numerical and experimental understanding of the XTT

acquisition schemes. The spherical representation of acquisition schemes provides a very useful tool to comprehend such schemes. However, this is not enough for a quantitative estimation of these schemes. Therefore, we presented a numerical metric to predict the quality of a given acquisition scheme. We demonstrated the validity and applicability of this metric by comparing it to an experimental metric that. The coverage sphere is a potentially valuable tool for designing task-specific acquisition schemes. By using this representation, we can selectively design acquisition schemes targetting the desired section on the unit sphere. We elaborate more on this idea in the next chapter.

Next, we used the two metrics to study two major aspects that contribute to the complexity of XTT acquisition schemes- time and rotation axes. We conclude that the coverage metric is a valid tool to optimize acquisition time for task-specific XTT measurements. More importantly, we conclude that it is possible to perform a full six-dimensional X-ray Tensor Tomography with at most two axes of sample rotation. Therefore, by adding only one additional rotation axis to a conventional X-ray Computed Tomography device, it is possible to obtain compact XTT setups for industrial and potential medical applications.

Chapter 8

Design of Acquisition Schemes and Setup Geometry

In Chapter 7, we presented a method to assess the efficacy of a given acquisition scheme for X-ray Dark-field Tomography. The Coverage Metric (section 7.2) was based on the fundamental idea that in order to measure a sensitivity point, we need to measure it from several tomographic points spread evenly on a circular trajectory. Sensitivity points that satisfy this condition for the given scheme were assigned a high value of coverage and vice-versa.

Motivated by the results in Chapter 7, we extend the same concept to design acquisition schemes in this chapter. We design acquisition schemes such that the aforementioned criteria is satisfied for a uniformly distributed set of orientations on the unit sphere. In simple words, the method works in two steps:

1. Choose a set of uniformly distributed points on the unit sphere,

2. Design a full tomographic trajectory corresponding to every point.

Using the above two steps, we formulate an approach to design acquisition schemes for directional dark-field tomography. Next, we use the AXDT reconstruction method (5.2) and null space analysis (3.3.2) to establish the validity of the proposed method.

We can see in Figure 7.3 that the cradle blocks the X-ray beam for higher values of ψ. This restricts the availability of measurable poses to $|\psi| \leq \psi_{max}$ and is a hurdle to the implementation of the acquisition schemes. Although detrimental, we can work around this limitation by optimizing the orientation of the grating bars. We study this effect extensively and conclude that certain grating

orientations provide significant advantage over others. Finally, we show experimental results to demonstrate the effectiveness of the new schemes as well as the effect of grating orientation.

This chapter is organized as follows. We present the method to design acquisition schemes in section 8.1 and study the effect of grating alignment on the experimental realization of the schemes in section 8.2. In section 8.3.2, we use null space analysis to demonstrate that the schemes work well with both the AXDT and XTT reconstruction approaches as we expect from conventional tomography. Finally, we demonstrate experimental results for all of the above analysis in section 8.4 and provide a comprehensive discussion in the following section.

8.1   Design of Acquisition Schemes

In conventional tomography, we acquire line integrals through a three-dimensional object onto a 2D detector and use analytic or iterative methods to reconstruct the 3D volume from several 2D images acquired at different poses of the sample (Chapter 3). The pre-requisite for recovering the 3D spatial information from 2D projections is that the total measured signal in any projection is constant, that is, the measured quantity (such as X-ray attenuation coefficient) is invariant under rotation. This is, however, not true for the dark-field signal. Due to its anisotropic nature, the dark-field signal varies as the object is rotated around an axis. However, it is possible to define an axis of rotation such that a certain component of the scattering function (q) is invariant under rotation of the object around this particular axis [Feldkamp et al. (2009)]. We use this concept to design an acquisition trajectory that comprises of several poses for which a unique component of the dark-field signal remains invariant, thus allowing for a full tomographic reconstruction of this particular component. In the following, we explain how such an acquisition trajectory can be designed for any scattering orientation $q \in \mathbb{S}^2$.

Recall that we defined the sensitivity vector $s(x) \in \mathbb{S}^2$ and the tomographic vector $t(x) \in \mathbb{S}^2$ for every acquisition pose $x = (\psi, \theta, \phi)$ as:

$$
\begin{aligned}
s(x) &= R(x) \cdot S, \\
t(x) &= R(x) \cdot T,
\end{aligned}
\tag{8.1}
$$

where $R(x) \in \mathbb{R}^{3 \times 3}$ is the Euler rotation matrix for the pose x, $S \in \mathbb{S}^2$ is the setup sensitivity, $T \in \mathbb{S}^2$ is the direction of beam propagation ($[0, 0, 1]^T$ in the setup shown in Fig, 7.3) and $\cdot$ denotes standard matrix-vector multiplication. S is the direction in which the phase shift is measured by the grating interferometer setup; it is orthogonal to the grating bars in the plane of the gratings ($[0, 1, 0]^T$ in the setup shown in Fig. 7.3). Evidently, the sensitivity vector denotes the scattering orientation that is probed at the acquisition pose x while the tomographic vector represents the direction along which the signal is integrated.

Let us define an acquisition scheme as:

$$
A(\psi, \theta, N) := \left\{ x = (\psi, \theta, \phi); \ \phi \in \left\{ 0°, \frac{180°}{N}, \ldots, 180° - \frac{180°}{N} \right\}; \ N \in \mathbb{N} \right\}.
\tag{8.2}
$$
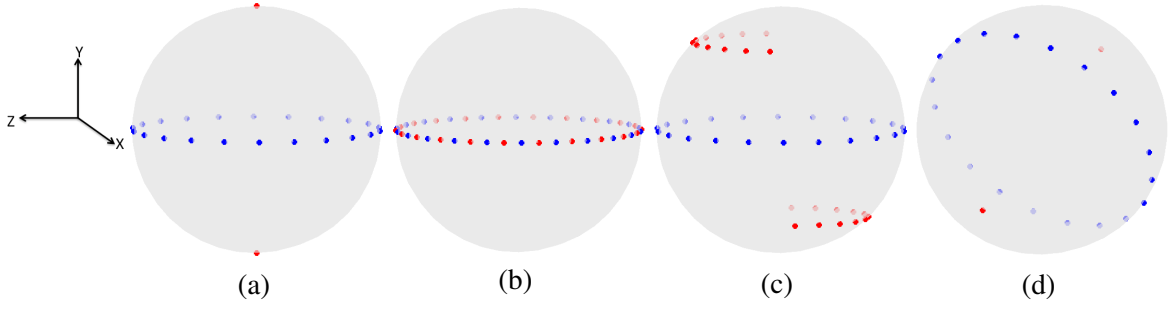
Figure 8.1: Spherical representation of acquisition schemes. Please note that in all these images, the sample can be imagined as being stationary at the center of the sphere while the setup rotates around it. Blue points represent the vectors $\pm t(x)$ and red points represent $\pm s(x)$ for all $x \in A(0,0,11)$ with (a) horizontal grating alignment, (b) vertical grating alignment, and (c) diagonal grating alignment. (d) The vectors $\pm t(y)$ and $\pm s(y)$ for all y in an exemplary acquisition scheme $Y(q, [0.7071, -0.7071, 0]^T, 10)$ obtained using the method explained in Algorithm 1. Figure by Sharma et al. (2017) is licensed under CC BY 4.0.

A conventional X-ray CT acquisition scheme in this notation can be expressed as $A(0,0,N)$. The points $\pm t(x)$ for $x \in A(0,0,11)$ are shown as blue dots in Figure 8.1(a). Such a circular measurement trajectory with sufficiently large value of N is desired for analytic reconstruction in X-ray CT (Chapter 3). Note that $A(0,0,N)$ is similar to the scheme $(X(0,180,N)$ in section 3.3.1. However, the sensitivity vector has no significance in X-ray CT since the measured quantity is invariant under rotation. In the case of dark-field signal, we also compute $\pm s(x)$ for $x \in A(0,0,11)$ assuming horizontally $(S = [0,1,0]^T)$, vertically $(S = [1,0,0]^T)$ and diagonally $(S = [0.7071, -0.7071, 0]^T)$ oriented gratings which are shown as red points in Figure 8.1(a-c).

Using the concept of rotational invariance, we postulate that a scattering orientation $q \in \mathbb{S}^2$ can be recovered for a three-dimensional volume by measuring it from N poses x_i, $i = 1, 2, \ldots, N$, such that $s(x_i) = q$ and the vectors $t(x_i)$ consist of N points equally spaced on a circular trajectory. It can be seen that this condition is satisfied for $q = [0,1,0]^T$ in Fig. 8.1(a). On the other hand, each of the 11 points of scheme $A(0,0,11)$ measure a separate sensitivity vector when gratings are placed vertically (Figure 8.1(b)) or diagonally (Figure 8.1(c)). However, we can obtain the same blue and red points as Fig. 8.1(a) for vertical and diagonal gratings with the schemes $A(0,90,11)$ and $A(0,45,11)$, respectively. More generally, we can obtain an acquisition scheme $Y(q,S,N) := \{y_i(q,S) := (\psi, \theta, \phi), i = 1, \ldots, N\}$ that fully measures the orientation q for the setup sensitivity S. In other words, $s(y_i(q,S)) = q$ for all i. To obtain a scheme $Y(q,S,N)$, we transform $x_i \in A(0,0,N)$ to $y_i(q,S)$. Note from Fig. 8.1(a) that $A(0,0,N) = Y([0,1,0]^T, [0,1,0]^T, N)$. The method to calculate $Y(q,S,N)$ from $A(0,0,N)$ is given in Algorithm 1.

Figure 8.1(d) shows an orientation vector $\pm q$ in red and the vectors $\pm t(y)$ in blue for all $y \in Y(q, [0.7071, -0.7071, 0]^T, 10)$. Using the procedure described above, we can design an acquisition scheme $Z(S,N)$ that measures L scattering orientations fully and comprises of $L * N$ poses for the

given setup sensitivity S:

$$Z(S,N) = \left\{ Y(q_l, S, N); l = 1, \ldots, L \right\}. \tag{8.3}$$

Algorithm 1: Calculate $Y(q, S, N)$ from $A(0, 0, N)$

For every $x \in A(0, 0, N)$

1. Calculate Euler rotation matrix $R(x)$.

2. Calculate $R_{intermediate}(x, q)$ such that $R_{intermediate}(x, q) \cdot [0, 1, 0]^T = q$:

$$R_{intermediate}(x, q) = R(x) \cdot M([0, 1, 0]^T, q), \tag{8.4}$$

   where $M(v_1, v_2) \in \mathbb{R}^{3 \times 3}$ is a matrix such that $v_2 = M(v_1, v_2) \cdot v_1$ for all $v_1, v_2 \in \mathbb{S}^2$.

3. Estimate the orientation $u(x, q, S) \in \mathbb{S}^2$ measured by the rotation matrix $R_{intermediate}(x, q)$ given the setup sensitivity S:

$$u(x, q, S) = R_{intermediate}(x, q) \cdot S. \tag{8.5}$$

4. Rotate $u(x, q, S)$ to q:

$$R_{final}(x, q, S) = R_{intermediate}(x, q) \cdot M(u(x, q, S), q). \tag{8.6}$$

5. Compute the pose $y(q, S) = (\psi, \theta, \phi)$ from the matrix $R_{final}(x, q, S)$ such that the absolute value of ψ in $y(q, S)$ is minimized. For calculation of pose (ψ, θ, ϕ) from the rotation matrix, please refer to Appendix B.

8.2 Acquisition Schemes and Setup Geometry

In the previous section, we presented a method to design an acquisition scheme $Z(S, N)$ that fully measures several sensitivity orientations on the unit sphere. The first step for designing such a scheme is to choose a set of orientations that we wish to measure. In order to reconstruct the spherical function using AXDT, it is required to choose orientations that are uniformly distributed on the unit sphere. One example of such sets of orientations are the t-designs presented by Hardin and Sloane (1996). We use these designs as they are a good choice for selecting uniformly distributed points on the sphere. However, any uniform distribution of points on the sphere can be used. We begin with a symmetric t-design consisting of 56 directions spread over the unit sphere as shown in Figure 8.2(a). Since the AXDT model is symmetric around the origin, we use only 28 directions of this t-design spread over one half of the unit sphere.

Next, we generate an acquisition scheme:

$$Z([0.7071, -0.7071, 0]^T, 100) = \left\{ Y(q_i, [0.7071, -0.7071, 0]^T, 100), \ i = 1, \ldots, 28 \right\}, \tag{8.7}$$
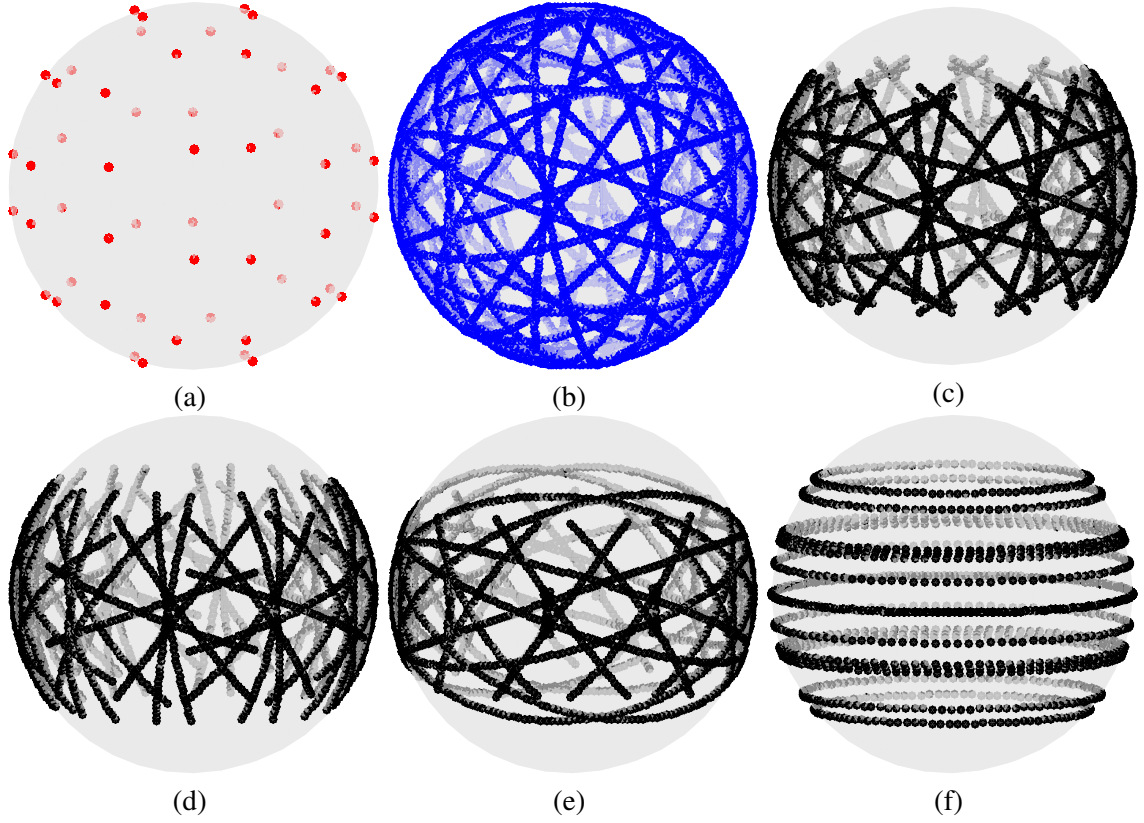
Figure 8.2: (a) A t-design with 56 uniformly distributed points. We aim to design trajectories that fully measure all of these scattering orientations. (b) Acquisition scheme $Z([0.7071, -0.7071, 0]^T, 100)$ with 2800 poses. Acquisition schemes (c) $Z_D(100)$ with 1676 poses, (d) $Z_H(100)$ with 1256 poses, (e) $Z_V(100)$ with 1284 poses, which measure all the points in (a) within the practical limitations of the setup with diagonally, horizontally and vertically aligned grating bars respectively. (f) acquisition scheme $W(100)$. Figure by Sharma et al. (2017) is licensed under CC BY 4.0.

consisting of 2800 poses. The vectors $\pm t(x)$ for all $x \in Z([0.7071, -0.7071, 0]^T, 100)$ are shown in Figure 8.2(b). This acquisition scheme fully measures the 56 points shown in Figure 8.2(a). However, it can be seen in Figure 7.3 that the Eulerian cradle intercepts the beam for high values of ψ, hence, the setup is limited to $-40 \leq \psi \leq 40$. Therefore, all of the 2800 poses for the scheme $Z(S, 100)$ cannot be measured. Figure 8.2(c) shows the points of Figure 8.2(b) that can be measured with the condition $|\psi| \leq 40°$.

The ratio of the points that can be measured (Figure 8.2(c)) to the total number of desired points (Figure 8.2(b)) is a function of the maximum reachable value of ψ and the setup sensitivity. Therefore, to study this effect, we calculate $Z(S, N)$ for 91 values of S such that:

$$\langle S, [1,0,0] \rangle = \cos(\alpha); \; \alpha \in [0°, 1°, 2°, \dots, 90°], \tag{8.8}$$

where $\langle \cdot, \cdot \rangle$ denotes the inner product. Figure 8.3(a) shows a 2D plot of the relative fraction of measurable poses (out of 2800) for the acquisition scheme $Z(S, 100)$ for different values of reach-
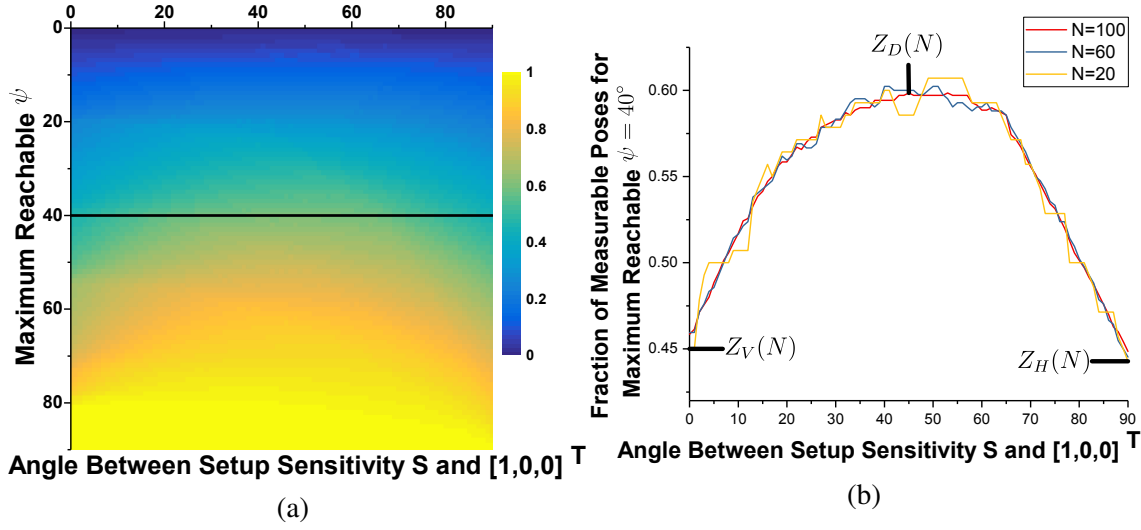
Figure 8.3: (a) 2D plot of the fraction of poses that can be measured with different grating arrangements and different ψ angle limitation. (b) Fraction of poses that can be measured with maximum reachable $\psi = 40°$ for acquisition schemes $Z(S,N)$. Red curve corresponds to the black line marked in (a). We study three points on these curves corresponding to vertical, diagonal and horizontal grating alignment denoted by $Z_V(N)$, $Z_D(N)$ and $Z_H(N)$ respectively. Figure by Sharma et al. (2017) is licensed under CC BY 4.0.

able $\psi \in [0°, 1°, 2°, \dots, 90°]$. A line of this 2D plot for the maximum reachable ψ limit of 40° is shown in Figure 8.3(b) (red curve). The point of maximum of this line plot corresponds to $Z([0.7071, -0.7071, 0]^T, 100)$, that is, when the grating bars are placed diagonally. In addition, similar line plots for acquisition schemes $Z(S,N), N = 60, 20$ are shown. We observe that the line plots for lower values of N have step-like artifacts arising from round-off errors which can be circumvented by using large number of sampling orientations. As it is difficult to actually align gratings at precise angles in most of the currently available setups, we only study the three extreme points marked in Figure 8.3(b). We define the notation $Z_D(N)$, $Z_H(N)$ and $Z_V(N)$ to denote acquisition schemes with diagonal, horizontal and vertical arrangement of grating bars respectively. Figure 8.2(c-e) shows the vectors $\pm t(x)$ for the measurable poses of acquisition schemes $Z_D(100)$, $Z_H(100)$, and $Z_V(100)$, respectively, assuming that poses with $|\psi| > 40°$ cannot be measured. It is evident from these results that the maximum amount of poses can be probed by placing the gratings such that the grating lines are aligned diagonally. From now on, we will assume that all acquisition schemes $Z(S,N)$ are truncated at $|\psi| = 40°$, since this is the practical limit of our setup.

8.3   Null Space Analysis

Recall that we provided a brief overview of null space analysis as a tool to assess acquisition schemes for CT in section 3.3.2. By looking at the null space of the system matrix P of a linear problem (such as the one in Eq. 3.14), we can assess the nature of the linear system, and in turn of the acquisition

scheme used to obtain the system. We already saw that the system matrix of the standard tomographic problem is typically too large to store in the memory of currently available computing devices and, hence, it is not possible to analytically calculate the null space of the matrix. Instead, we calculate one component of the null space v by iteratively solving for $Av = 0$. Below, we extend the same concept to calculate the null space for the XTT and AXDT system matrices.

8.3.1 Methods

Null space of A_{AXDT}

The full system matrix A_{AXDT} (see Eq. 5.16) for AXDT is larger than that of CT by an additional factor of $2^K - 1$ where K is the highest degree of spherical harmonic ($K = 4$ for our case). Therefore, we reconstruct one vector spanning a subspace of the nullspace of A_{AXDT} by iteratively solving $A_{AXDT}\eta = 0$ for η. Different vectors $\eta \in \ker(A_{AXDT})$ can be computed by starting from different initial guesses for η. We compute one component of the null space by starting with an initial guess of η such that:

$$\eta = \left\{ \eta_k^m; \; \eta_k^m = 0 \text{ for } k \neq 0 \; , \; \eta_k^m = \begin{pmatrix} 0.01 \\ \vdots \\ 0.01 \end{pmatrix} \text{ for } k = 0 \right\}, \tag{8.9}$$

for all voxels. Since spherical harmonics are equivalent to a fourier series in terms of angular frequency, this initial guess is equivalent to starting with a uniform spherical function which is a good initial guess for clearly visualizing the effect of AXDT acquisition schemes.

Null space of A_{XTT}

Similarly, the system matrix of XTT (see Eq. 5.5) is larger than the CT system matrix P by an additional factor of K, where K is the number of pre-defined scattering orientations (see section 5.1). Therefore, we reconstruct one vector spanning a subspace of the nullspace of A_{XTT} by iteratively solving $A_{XTT}\beta = 0$ for β. Different vectors $\beta \in \ker(A_{XTT})$ can be computed by starting from different initial guesses for β. We compute one component of the null space by starting with an initial guess of β such that:

$$\beta = \left\{ \beta_k; \; \beta_k = \begin{pmatrix} 0.01 \\ \vdots \\ 0.01 \end{pmatrix} \right\}. \tag{8.10}$$

This initial guess is equivalent to the initial guess η for AXDT i.e. a uniform unit sphere.

For computing the null space in both the cases above, we set the reconstruction volume size to $50 \times 50 \times 50$, the detector size to 100×100 to limit computation times and use a parallel geometry assumption in order to eliminate errors at the edges due to forward and back-projection.

8.3.2   Results

It was outlined above that the acquisition trajectories are truncated due to the physical limitations of the setup. This means that we cannot measure the full tomographic trajectory $Y(q_i, S, N)$ for all the orientations q_i, $i = 1, \ldots, 28$. The missing angles lead to circular trajectories with missing wedges similar to the ones in limited angle tomography. In standard tomography, the null space is easily understood in terms of the Fourier Slice theorem as explained in section 3.3.2. However, the Fourier Slice theorem does not carry over to our system due to its sensitivity specificity. Hence, it is not possible to assume that similar limited angle artifacts can also be seen for the case of AXDT. Moreover, all of the poses for $Z(S, N)$ are used for the reconstruction of the spherical harmonic coefficients in AXDT reconstruction, and there is no direct reconstruction of individual components corresponding to each of the truncated trajectory. However, we postulate that our acquisition schemes correlate well to the reconstruction process of AXDT/XTT and, hence, some effect of the limited angle trajectories should be visible in the corresponding spherical function. We check this hypothesis by visualizing the null space of the AXDT and XTT operators.

Correlation of Acquisition Schemes with AXDT

We estimate the null space for the proposed schemes as explained in section 8.3.1. Next, we probe the reconstructed null space (in terms of spherical coefficients) at the specific points $q_i, i = 1, \ldots, 28$, in order to evaluate the effect of the missing wedges for these individual scattering orientations. Figure 8.4 shows the null space components for the scheme $Z_D(100)$. The magenta points show the tomographic trajectory for all components q_i as projected onto the $x - z$ plane. Analogously, the images show the null space averaged over all $x - z$ planes for the corresponding component after the first iteration. The null space artifacts caused by the ψ truncation can be seen explicitly in the individual components reconstructed with AXDT. We also show corresponding figures for $Z_V(100)$ and $Z_H(100)$ in Figures 8.6 and 8.5, respectively.

Correlation of Acquisition Schemes with XTT

We calculate the null space of the XTT operator for the acquisition scheme $Z_D(100)$. For setting up the operator A_{XTT}, we set the pre-defined set of orientations to $q_i, i = 1, \ldots, 28$, same as the one used for designing the acquisition scheme (Eq. 8.3). In Figure 8.7, we show the null space components of the 28 points similar to the Figures 8.4 to 8.6.

   For all the four cases in Figures 8.4 to 8.7, we can see limited angle artifacts for every single point on the sensitivity sphere, as we would expect if we measured them separately. Moreover, we should note that we use all the poses in the reconstruction approaches for both XTT and AXDT as is explained in Chapter 5 and later probe the points separately. This observation is a very strong indication that the proposed method to design acquisition schemes presented in section 8.1 is coherent with both the reconstruction models presented in Chapter 5.
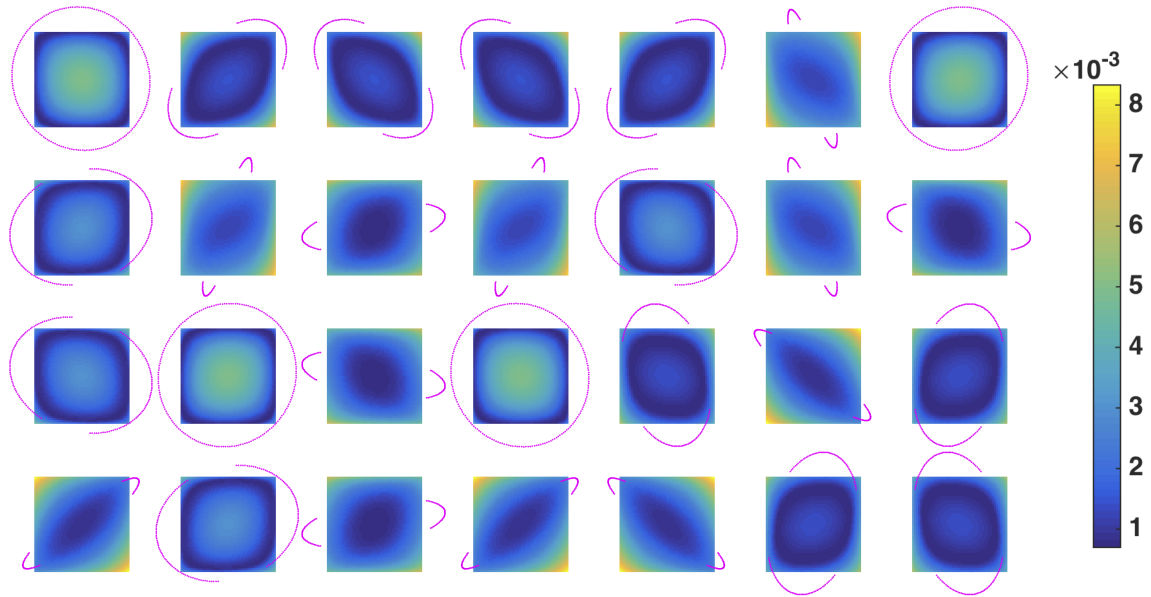
Figure 8.4: Null space components for each of the 28 points in Figure 8.2(a) calculated using the acquisition scheme $Z_D(100)$ (Figure 8.2(c)). The magenta points show the trajectories for each component truncated for maximum reachable $|\psi| = 40°$ and the correponding images show the null space averaged over all $x - z$ planes. Figure by Sharma et al. (2017) is licensed under CC BY 4.0.
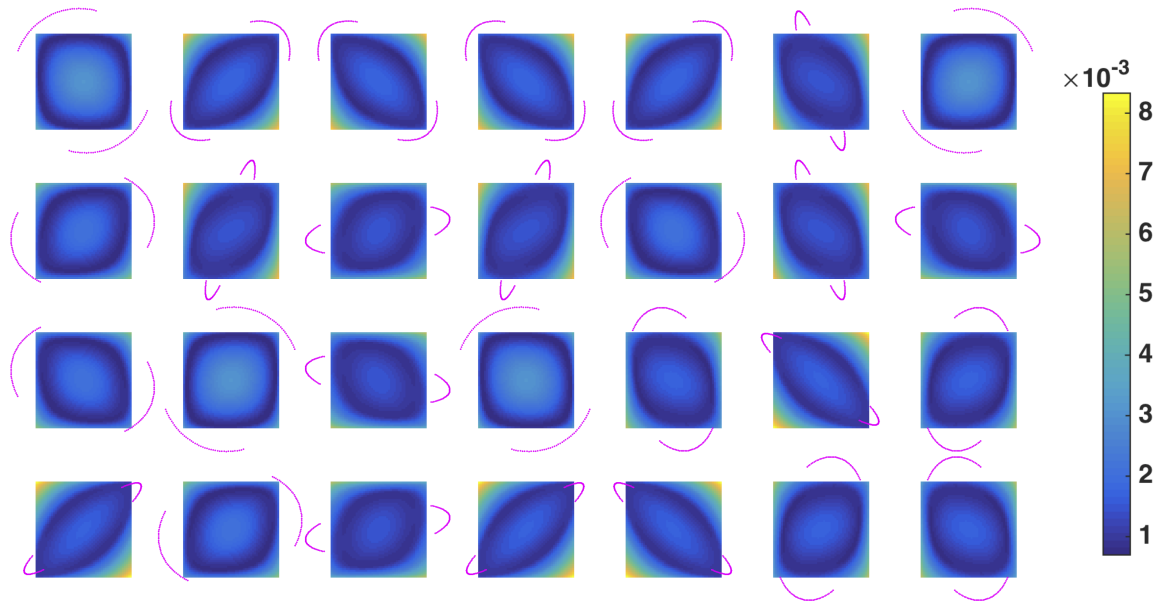
Figure 8.5: Null space components for each of the 28 points in Figure 3(a) in the manuscript calculated using the acquisition scheme $Z_H(100)$ (Figure 3(d) in the manuscript). The magenta points show the trajectories for each component truncated for maximum reachable $|\psi| = 40°$ and the correponding images show the null space averaged over all $x - z$ planes. Figure by Sharma et al. (2017) is licensed under CC BY 4.0.
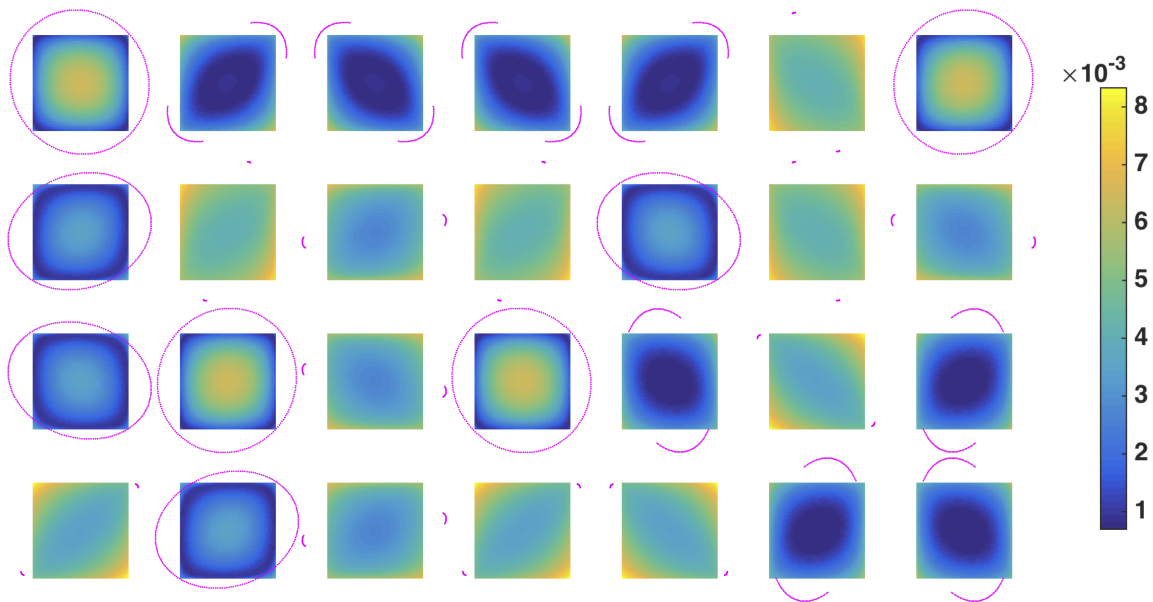
Figure 8.6: Null space components for each of the 28 points in Figure 3(a) in the manuscript calculated using the acquisition scheme $Z_V(100)$ (Figure 3(e) in the manuscript). The magenta points show the trajectories for each component truncated for maximum reachable $|\psi| = 40°$ and the correponding images show the null space averaged over all $x - z$ planes. Figure by Sharma et al. (2017) is licensed under CC BY 4.0.
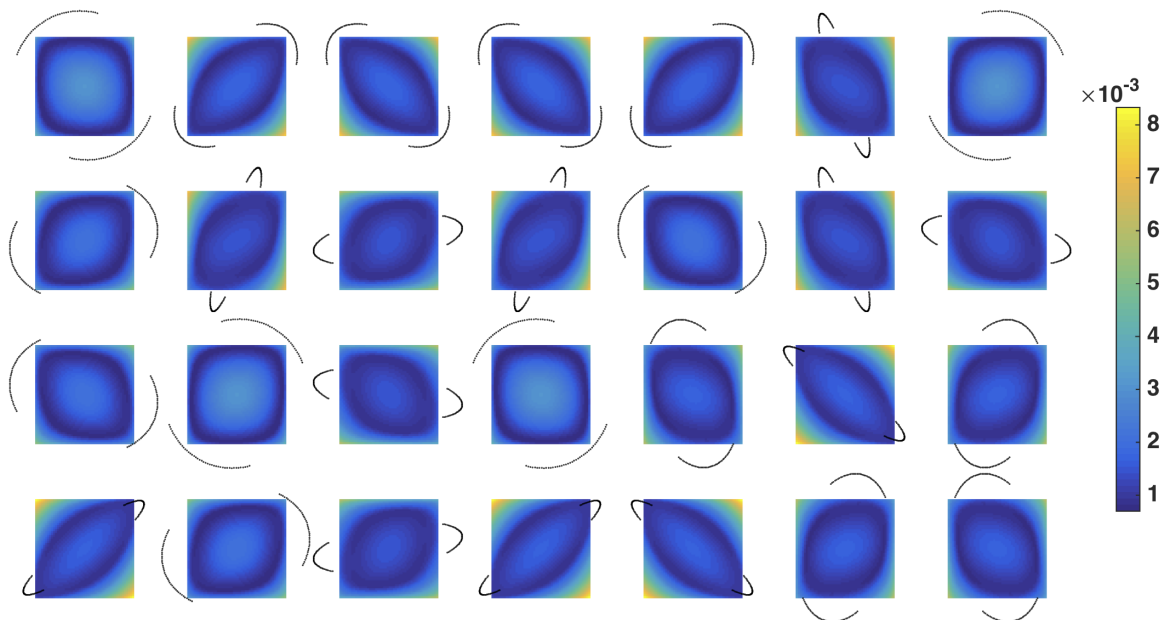
Figure 8.7: Null space components for each of the 28 points in Figure 3(a) in the manuscript calculated using the acquisition scheme $Z_V(100)$ (Figure 3(e) in the manuscript). The magenta points show the trajectories for each component truncated for maximum reachable $|\psi| = 40°$ and the correponding images show the null space averaged over all $x - z$ planes.

<div align="center">(a)   (b)</div>
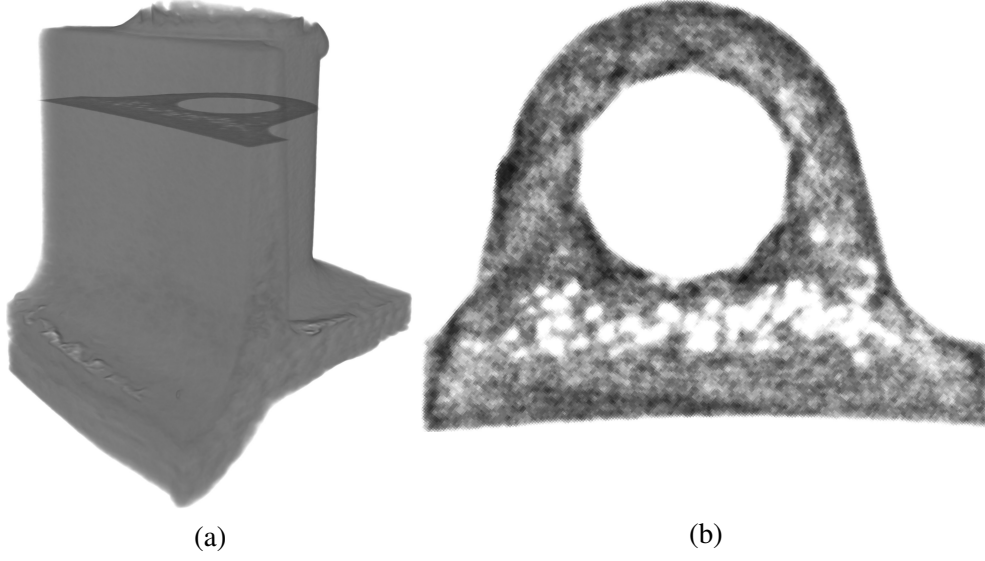
Figure 8.8: Attenuation volume (a) 3D rendering (b) A slice shown of the attenuation volume marked in (a). Porosity is clearly visible in attenuation.

8.4 Experiments

In this section, we present experimental results to support the observations made in sections 8.3.2 and 8.2. We measured a circular thermoplastic short fibre moulding part, composed of fibres that are 7 μm thick and 200 μm long, at a resolution of approximately 80 μm in the setup described in section 7.4.1. We measured the sample with the following acquisition schemes:

1. $Z_D(N)$ - New schemes (section 8.1) with diagonal grating alignment

2. $Z_H(N)$ - New schemes (section 8.1) with horizontal grating alignment

3. $Z_V(N)$ - New schemes (section 8.1) with vertical grating alignment

4. $W(N)$ - Schemes introduced by Malecki et al. (2014) with vertical grating alignment. Such a scheme can be written as:

$$
\begin{aligned}
W(N) = \{w = (\psi, \theta, \phi); \\
\psi \in \{0°, 20°, 40°\}, \\
\theta \in \{0°, 30°, 60°, 90°\}, \\
\phi \in \{0°, \frac{360°}{N}, \dots, 360° - \frac{360°}{N}\}\}.
\end{aligned}
\tag{8.11}
$$

The trajectory $\pm t(w)$ for all $w \in W(100)$ is shown in Figure 8.2(f).

We employed 7 phase steps with 1 sec. exposure per step for obtaining a single dark-field image for all the schemes.

<center>(a)   (b)</center>
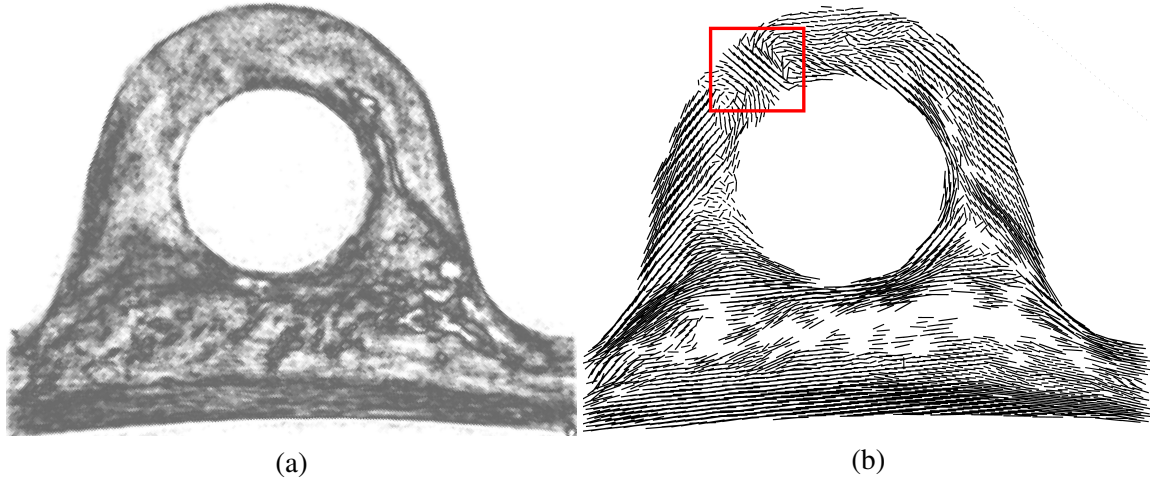
Figure 8.9: A slice of (a) the isotropic scattering component, and (b) the 3D vectors reconstructed using AXDT for a thermoplastic short fibre moulding sample measured at a spatial resolution of approximately 80 μm. The red box marks a feature that cannot be seen in either of (a) or (b). We can see in (a) that porosity cannot be seen in the dark-field image. Therefore, we mask porosity in (b) with the attenuation volume (Figure 8.8)
.

First, we reconstruct the attenuation volume using the scheme $Z_D(100)$ and show its 3D rendering in Figure 8.8(a). A slice of the volume is shown in Figure 8.8(b). Obviously, the imaging resolution is not sufficient to resolve the fibres with a diameter of 7 μm. However, we can resolve the porosity as can be seen.

Next, we perform AXDT reconstruction of the same volume. A slice of η_0^0, which is the isotropic component of the dark-field signal, is shown Figure 8.9(a). Figure 8.9(b) shows the main orientation in every third voxel as extracted from the spherical function. The vectors have been masked with the attenuation signal to avoid the undesired effect of edge-scattering at the pores [Yashiro and Momose (2015), Wolf et al. (2015)]. The red box in Figure 8.9(b) shows a feature in this sample which cannot be seen in either of 8.9(a) or 8.8(b). This is a weld-line and is only revealed by extracting the orientations of the fibres in the region using AXDT. Very high resolution micro CT may be required to directly resolve this structure but then a sample of this dimension ($28 \times 23 \times 21$ mm^3) cannot be measured at once and one would have to resort to multiple tomographies or even to destroying the sample.

We use detectability of the unique feature highlighted in Figure 8.9(b) to compare and contrast the different acquisition schemes. In order to do so, we define an experimental metric similar to the one in section 7.3.

8.4.1 Experimental Metric

We consider the scheme $Z_D(100)$ as a standard, over-sampled scheme with the highest quality result. As was done in section 7.3, we define an Experimental Metric, $EM(X)$, for an acquisition schemes X
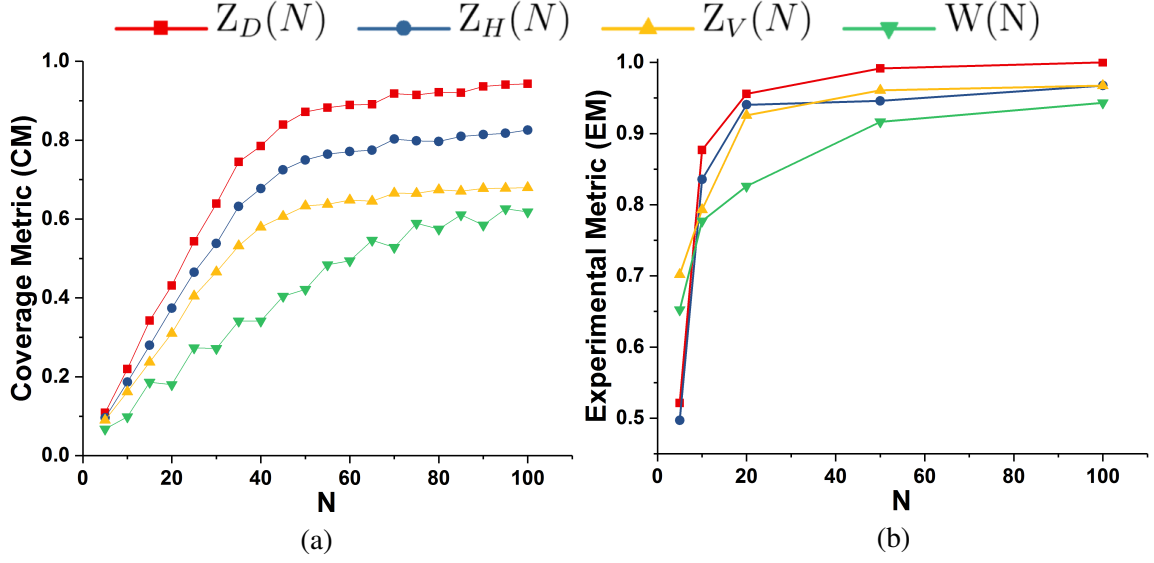
Figure 8.10: (a) Coverage Metric (*CM*) and (b) Experimental Metric (*EM*) as a function of *N* for four different acquisition schemes.

as:

$$EM(X) = \frac{1}{I} \sum_{i=1}^{I} \left| \langle U_i(X), U_i(Z_D(100)) \rangle \right| \tag{8.12}$$

where $\langle \cdot, \cdot \rangle$ is the standard scalar product, $U_i(Z_D(100))$ and $U_i(X)$ denote the structure orientation for the voxel index $i = 1, \ldots, I$ in the region-of-interest (red rectangle in Figure 8.11) calculated using the acquisition scheme $Z_D(100)$ and an arbitrary scheme X, respectively.

8.5 Results

We show the region marked in Figure 8.9(b) for different acquisition schemes in Figure 8.11. The columns in Figure 8.11 correspond to three different values of $N = \{100, 20, 10\}$ for a specific scheme, while the rows show four different schemes for the same value of *N*. The value of the Experimental Metric for different schemes is shown in Figure 8.10(b).

In addition to the experimental metric, we also use the Coverage Metric (*CM*) to compare the schemes. This is a metric which determines the degree up to which an acquisition scheme measures all orientations on the unit sphere or, in other words, $CM(X)$ provides a measure of the efficiency of any acquisition scheme *X*. The usability of *CM* as a valid metric for XTT acquisition schemes was established in Chapter 7. It can be directly applied to AXDT as well, since the two methods only differ in the reconstruction method and the acquisition protocol is identical. Figure 8.10(a) shows the coverage metric for $Z_D(N), Z_H(N), Z_V(N)$, and $W(N)$ for different values of *N*.
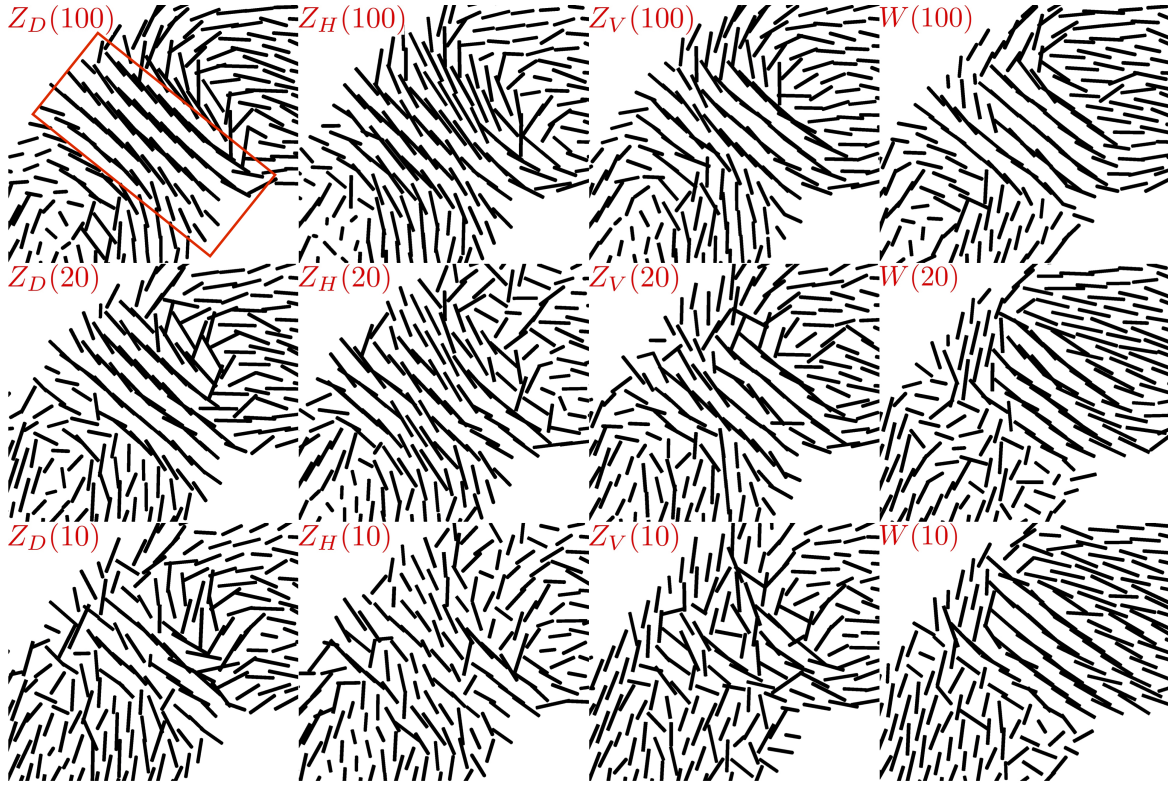
Figure 8.11: Structure orientations calculated using AXDT in the region-of-interest (indicated by the red box in Figure 8.9(c)) for different acquisition schemes. Each column corresponds to acquisition schemes and every row shows the four schemes with the same value of *N*. The red box indicates the region-of-interest used for calculating the Experimental Metric. Figure by Sharma et al. (2017) is licensed under CC BY 4.0.

8.6   Discussion

We present a new technique to design acquisition schemes for directional dark-field tomographic imaging. We use the concept of rotational invariance to design tomographic trajectories that fully measure a unique component of the three dimensional scattering function. However, we show that all of the desired poses cannot be measured in a regular setup. In fact, this is a problem for most of the setup configurations, since it is always difficult to measure along the axis of the sample mount with X-rays. Therefore, we show the fraction of poses that can be measured for different setup configurations in Figure 8.3(a) and (b). We observe that while it is possible to measure all the information with any grating orientation in an ideal setup, the grating orientation starts to play a major role when the setup limitation, that is the availability of the angle ψ only up to a certain value, is enforced. It can be seen that we can optimize the amount of measurable poses by placing the gratings diagonally.

Next, we study the effect of the aforementioned setup limitation by visualizing the null space of the AXDT operator. It can be seen in Figures 8.4 to 8.7 that the ψ limitation leads to missing wedges (magenta points) in the tomographic trajectories for most of the orientations. We note that the effect

of these missing wedges can be directly seen in the null space of the corresponding component. This is an interesting finding because of the fact that even though the AXDT operator uses all of the poses at the same time to reconstruct the spherical function, we are still able to see the effect of the limited angle trajectories at the corresponding sensitivity points on the reconstructed field. More importantly, the null space visualization is proof that the initial concept of calculating tomographic trajectories which provide invariant dark-field signal for certain pre-defined orientation vectors works exactly as we expect it to. Please note that the fact that we only get one component of $\ker(A)$ is not a limitation for our work since we compute this component in the exact same way for all the orientations.

We use the Coverage Metric (CM) (Chapter 7) to compare the new schemes $Z_D(N), Z_H(N), Z_V(N)$ among themselves and to the schemes that have been used by our group in previous works $W(N)$. It can be seen in Figure 8.10(a) that the value of CM decreases with the value of N for all four schemes and that the new schemes outperform the previously used scheme $W(N)$. Moreover, $Z_D(N)$ has the highest value of CM amongst the new schemes. This implies that diagonal grating alignment is the most efficient of the proposed schemes (as also seen in Figure 8.3), followed by horizontal alignment, and vertical grating alignment is the least favorable.

Finally, we show an example of the application of AXDT to an industrially relevant composite material. We show in Figure 8.9(c) that AXDT is able to resolve orientations of fibres with sizes that are much below the resolution of the imaging system. Moreover, the fibre orientations calculated using AXDT reveal a particular feature (weld-line) in the sample which cannot be seen in conventional attenuation or even the isotropic component of the dark-field signal. We compare, qualitatively in Figure 8.11 and quantitatively in Figure 8.10, the new schemes $Z(S,N)$ for three different grating orientations and the old schemes $W(N)$. We can see in Figure 8.11 that although the weld-line is clearly visible in all the schemes with $N = 100$ (first row), the scheme $Z_D(100)$ provides the most comprehensible distinction of the weld-line. More importantly, the quality of this result is maintained for $Z_D(20)$ and $Z_H(20)$, while significant deterioration can be seen for $Z_V(20)$ and $W(20)$. The vectors reconstructed with the schemes $W(N)$ (last column in Figure 8.11) seem to be oriented in certain preferred directions and the variations are lost. This is due to the fact that the schemes $W(N)$ provide an uneven sampling of the unit sphere and the reconstruction is biased towards a partial reconstruction of the most commonly sampled scattering orientations.

In Figure 8.10(b), we compare the performance of the schemes with respect to the scheme $Z_D(100)$, which is assumed as the reference dataset. Here, we can see that the vectors in the region-of-interest deviate most from the reference for the schemes $W(N)$. Also, we observe that the trend of the graph for the four schemes matches the corresponding trend observed in Figure 8.10(a). This observation supports our claim that the new type of acquisition schemes provide better results than the old ones. Moreover, we can also conclude that diagonal grating orientation is the most favorable followed by horizontal and vertical alignment of gratings for the new schemes. It should also be noted that $Z_D(20)$ corresponds to a measurement time of only ~ 2 hours and is still of comparable quality to $Z_D(100)$ which requires ~ 10 hours of measurement. This reduction in acquisition time

is a substantial improvement compared to the long measuring times of ~ 10 hours required for the schemes used previously [Malecki et al. (2014),Vogel et al. (2015),Sharma et al. (2016)].

8.7   Summary

In this work, we present a more efficient method to design acquisition schemes for tomographic imaging of the directional dark-field signal and present results of diagonal grating orientation being the most optimal setup configuration for these schemes. Finally, we also show that the new schemes with diagonal grating alignment allow us to obtain good image quality with only ~ 2 hours of measurement time instead of the ~ 10 hours of measurements that was used previously.

Chapter 9

Summary and Outlook

Anisotropic X-ray Dark-field (AXDF) imaging aims to bridge the gap between industrial demands of resolution and available X-ray technology. By reconstructing the reciprocal space scattering information in every real space voxel, AXDF imaging aims to reveal information about micron and sub-micron sized structures in centimeter sized samples. However, these methods suffer from a long and tedious measurement procedure which is a hurdle to their practical applications in industry and medicine. In this thesis, we presented strategies to simplify the acquisition methods for AXDF imaging in two and three dimensions with the goal of applying these methods to real world applications.

In order to lay the context for understanding the contributions of this work, we briefly explained the basics of conventional X-ray Computed Tomography in Chapter 3. Next, we reviewed recent developments in the field of X-ray dark-field imaging in Chapter 4, and introduced a two dimensional AXDF imaging modality. Chapter 5 covered, in detail, the most recent developments in the field of AXDF tomography. Finally, we addressed the need to simplify measurement methods for AXDF imaging in the following ways.

1. Two dimensional AXDF imaging

   Analogous to conventional radiography, X-ray Vector Radiography is a two dimensional AXDF imaging method. As the name suggests, we reconstruct the orientations of micro structure inside a sample by analyzing the variation in the dark-field signal as the sample is rotated around the beam propagation direction. Conventional XVR measurements require a time consuming stepwise process of sample rotation and grating stepping. We presented a new method, namely Trochoidal X-ray Vector Radiography (TXVR) that overcomes these limitations. We replace the tedious stepwise process with a fast, continuous motion of the sample in a trochoidal trajectory. By doing so, we obviate the need to step gratings during the measurement and enable the fast measurement of continuously moving samples, thus taking a significant step forward towards the commercialization of this method.

2. AXDF Tomography

AXDF tomography aims at the reconstruction of the three dimensional scattering function at every three dimensional location inside the sample. It is, therefore, required to understand the requirements of AXDF tomography with respect to optimal sampling of both the reciprocal and real space information. We approached this problem in two ways:

(a) Reducing the hardware and time complexity of existing schemes:

We introduced and validated a numerical measure to predict the efficacy of existing schemes in section 7.2. We used this measure to design sparse acquisition schemes for XTT. An important conclusion of this study was that we can perform XTT with only two rotation axes instead of three, as initially proposed.

(b) Design of acquisition schemes:

In Chapter 8, we took a step back and laid down the foundations for an optimal sampling protocol. We used ideas from Chapter 7 to develop an approach for designing acquisition schemes for any arbitrary setup configuration. We proved the validity of our approach using knowledge from convention tomography (Chapter 3). Moreover, we discussed optimal setup configuration to implement the new schemes and showed promising results with respect to the schemes used earlier.

9.1   Outlook

AXDF imaging is a new category of X-ray imaging modalities. Owing to the aforementioned obstacles for measurement, the field has not been able to gather as much attention from the scientific community as it deserves. With the results presented in this thesis, we hope to overcome some of the barriers to this and hope to see this field move much faster in the coming years.

Trochoidal X-ray Vector Radiography (TXVR) is a novel and easy way of resolving structure orientations in thin samples. The main focus of this chapter was to demonstrate proof-of-principle of using the trochoidal trajectory for XVR measurement. However, we did not make full use of the trochoidal motion during the processing stage. The speed and accuracy of TXVR can be significantly increased, in future work, by incorporating properties of the trochoid into the processing algorithm.

One of the most important factors for AXDF tomographic acquisition is the number of rotation axes needed for the measurement. We showed, in Chapter 7, that while two rotation axes are sufficient for this, a single rotation axis does not work. However, we did not take into consideration the fact that we do not always need to sample the entire unit sphere of orientations for a given task. We believe that the Coverage Metric (section 7.2) can be used to design task-specific acquisition schemes with much lesser hardware complexity than the schemes presented in this thesis.

Finally, the correlation of the new schemes (Chapter 8) with conventional tomography is a strong indication of the fact that we have been able to successfully relate our methods to conventional tomography. This implies that we can now use decades of knowledge from CT for AXDF tomography and develop this technology at a much faster pace.

Appendix A

Rotation Matrix from Euler Angles

In this appendix, we provide the calculation of the rotation matrix $R(x)$ for the pose $x := (\psi, \theta, \phi)$ in the setup (Figure 7.3) using an eulerian cradle Figure 6.1(b). An eulerian cradle provides the following three rotation axes (see Figure 7.3):

1. ψ- Rotation about y axis

2. θ- Rotation about z' axis

3. ϕ - Rotation about y' axis

In order to reach the pose (ψ, θ, ϕ), first we rotate the sample around the y axis:

$$R_y(\psi) = \begin{bmatrix} \cos\psi & 0 & \sin\psi \\ 0 & 1 & 0 \\ -\sin\psi & 0 & \cos\psi \end{bmatrix} \tag{A.1}$$

Next, we rotate the sample around the z' axis:

$$R_z(\theta) = \begin{bmatrix} \cos\theta & -\sin\theta & 0 \\ \sin\theta & \cos\theta & 0 \\ 0 & 0 & 1 \end{bmatrix} \tag{A.2}$$

Finally, we rotate around the y' axis, which is analogous to standard rotation in CT:

$$R_y(\phi) = \begin{bmatrix} \cos\phi & 0 & \sin\phi \\ 0 & 1 & 0 \\ -\sin\phi & 0 & \cos\phi \end{bmatrix} \tag{A.3}$$

The rotation matrix $R(x)$ for the pose $x := (\psi, \theta, \phi)$ can now be calculated as $R(x) = R_y(\psi) \cdot R_z(\theta) \cdot R_y(\phi)$. Using Equation A.1 and A.2,

$$R_y(\psi) \cdot R_z(\theta) = \begin{bmatrix} \cos\psi\cos\theta & -\cos\psi\sin\theta & \sin\psi \\ \sin\theta & \cos\theta & 0 \\ -\sin\psi\cos\theta & \sin\psi\sin\theta & \cos\psi \end{bmatrix} \tag{A.4}$$

Using Equation A.3 and A.4,

$$R(x) = R_y(\psi) \cdot R_z(\theta) \cdot R_y(\phi) =$$
$$\begin{bmatrix} \cos\psi\cos\theta\cos\phi - \sin\psi\sin\phi & -\cos\psi\sin\theta & \cos\psi\cos\theta\sin\phi + \sin\psi\cos\phi \\ \sin\theta\cos\phi & \cos\theta & \sin\theta\sin\phi \\ -\sin\psi\cos\theta\cos\phi - \cos\psi\sin\phi & \sin\psi\sin\theta & -\sin\psi\cos\theta\sin\phi + \cos\psi\cos\phi \end{bmatrix} \tag{A.5}$$

Appendix B

Euler Angles from Rotation matrix

Calculation of a unique pose $x := (\psi, \theta, \phi)$ from a given rotation matrix $R(x)$ is not trivial. Below, we present details of this calculation used for the last step in Algorithm 1. Let us write a generalised rotation matrix as:

$$\begin{bmatrix} R_{00} & R_{01} & R_{02} \\ R_{10} & R_{11} & R_{12} \\ R_{20} & R_{21} & R_{22} \end{bmatrix} \tag{B.1}$$

Comparing Eq. 6.2 and B.1,

$$R_{11} = \cos\theta. \tag{B.2}$$

Now, we have two cases:

If $|R_{11}| \neq 1$

Values of θ

Keeping in mind that $\cos\theta = \cos(-\theta)$, there are actually two values for θ that satisfy Eq. B.2 for $R_{11} \neq \pm 1$ (we will handle this case in the next section):

$$\begin{aligned} \theta_1 &= \arccos(R_{11}) \\ \theta_2 &= -\arccos(R_{11}) \end{aligned} \tag{B.3}$$

Values of ψ

Using Eqs. A.5 and B.1,

$$\frac{R_{21}}{-R_{01}} = \tan\psi \tag{B.4}$$

We use this equation to solve for ψ as:

$$\psi = \arctan2(R_{21}, -R_{01}), \tag{B.5}$$

where $\arctan2(y, x)$ is arc tangent of the two variables x and y. It is similar to calculating the arc tangent of y/x, except that the signs of both arguments are used to determine the quadrant of the result, which lies in the range $[-\pi, \pi]$. One must be careful in interpreting Equation B.5. If $\sin\theta > 0$, then $\psi = \arctan2(R_{21}, -R_{01})$. However, when $\sin(\theta) < 0$, $\psi = \arctan2(-R_{21}, R_{01})$. A simple way to handle this is to use the equation B.6 to compute ψ:

$$\psi = \arctan2\left(\frac{R_{21}}{\sin\theta}, \frac{-R_{01}}{\sin\theta}\right), \tag{B.6}$$

Equation B.6 is valid for all cases except when $\sin\theta = 0$. We will deal with this case in the next section. For each value of θ, we compute a corresponding value of ψ using Equation B.6, yielding:

$$\begin{aligned}
\psi_1 &= \arctan2\left(\frac{R_{21}}{\sin\theta_1}, \frac{-R_{01}}{\sin\theta_1}\right), \\
\psi_2 &= \arctan2\left(\frac{R_{21}}{\sin\theta_2}, \frac{-R_{01}}{\sin\theta_2}\right),
\end{aligned} \tag{B.7}$$

Values of ϕ

Using Eqs. A.5 and B.1,

$$\frac{R_{12}}{R_{10}} = \tan\phi \tag{B.8}$$

Using similar arguments as above, we end up with two values of ϕ:

$$\begin{aligned}
\phi_1 &= \arctan2\left(\frac{R_{12}}{\sin\theta_1}, \frac{R_{10}}{\sin\theta_1}\right), \\
\phi_2 &= \arctan2\left(\frac{R_{12}}{\sin\theta_2}, \frac{R_{10}}{\sin\theta_2}\right),
\end{aligned} \tag{B.9}$$

We now have two solutions $x_1 := (\theta_1, \psi_1, \phi_1)$ and $x_2 := (\theta_2, \psi_2, \phi_2)$ when $|R_{11}| \neq 1$. Both the solutions are valid. We use $x := (\theta_1, \psi_1, \phi_1)$ in the last step of Algorithm 1.

If $|R_{11}| = 1$

When $|\cos\theta| = 1$, $\sin\theta = 0$ and the RHS of equations B.7 and B.9 boil down to $\arctan2\left(\frac{0}{0}, \frac{0}{0}\right)$. In this case, R_{12}, R_{10}, R_{21} and R_{01} do not constrain the values of ψ and ϕ. Therefore, we must use different elements of the rotation matrix to compute the values of ψ and ϕ.

If $R_{11} = 1$

Obviously,

$$\theta = 0. \tag{B.10}$$

From equations A.5 and B.1,

$$R_{0,0} = \cos\psi\cos\phi - \sin\psi\sin\phi = \cos(\psi+\phi)$$
$$R_{0,2} = \cos\psi\sin\phi + \sin\psi\cos\phi = \sin(\psi+\phi)$$
$$R_{2,0} = -\sin\psi\cos\phi - \cos\psi\sin\phi = -\sin(\psi+\phi)$$
$$R_{2,2} = -\sin\psi\sin\phi + \cos\psi\cos\phi = \cos(\psi+\phi)$$

(B.11)

Therefore,

$$\tan(\psi+\phi) = \frac{R_{0,2}}{R_{0,0}}$$
$$\psi+\phi = \text{arctan2}(R_{0,2}, R_{0,0})$$
$$\phi = \psi + \text{arctan2}(R_{0,2}, R_{0,0})$$

(B.12)

Infinite solutions exist.

If $R_{11} = -1$

Obviously,

$$\theta = \pi.$$

(B.13)

Same as above, from equations A.5 and B.1

$$R_{0,0} = -\cos\psi\cos\phi - \sin\psi\sin\phi = -\cos(\psi-\phi)$$
$$R_{0,2} = -\cos\psi\sin\phi + \sin\psi\cos\phi = \sin(\psi-\phi)$$
$$R_{2,0} = \sin\psi\cos\phi - \cos\psi\sin\phi = -\sin(\psi-\phi)$$
$$R_{2,2} = \sin\psi\sin\phi + \cos\psi\cos\phi = \cos(\psi-\phi)$$

(B.14)

Therefore,

$$\tan(\psi-\phi) = \frac{R_{0,2}}{-R_{0,0}}$$
$$\psi-\phi = \text{arctan2}(R_{0,2}, -R_{0,0})$$
$$\phi = \psi - \text{arctan2}(R_{0,2}, -R_{0,0})$$

(B.15)

Infinite solutions exist.

In both the above cases, we set $\psi = 0$ and calculate ϕ to obtain a unique solution. This obviously makes sense since ψ rotation is much slower than ϕ.

Bibliography

Als-Nielsen, J. and McMorrow, D. (2011). *Elements of Modern X-ray Physics*. Wiley.

Arboleda, C., Wang, Z., and Stampanoni, M. (2014). Tilted-grating approach for scanning-mode X-ray phase contrast imaging. *Optics Express*, 22(13):15447.

Attwood, D. (1999). *Soft X-Rays and Extreme Ultraviolet Radiation: Principles and Applications*. Cambridge University Press.

Bachche, S., Nonoguchi, M., Kato, K., Kageyama, M., Koike, T., Kuribayashi, M., and Momose, A. (2017). Laboratory-based X-ray phase-imaging scanner using Talbot-Lau interferometer for non-destructive testing. *Scientific Reports*, 7(1):6711.

Banhart, J. (2008). *Advanced Tomographic Methods in Materials Research and Engineering*. Monographs on the Physics and Chemistry of Materials. Oxford Univ. Press, Oxford.

Bayer, F., Zabler, S., Brendel, C., Pelzer, G., Rieger, J., Ritter, A., Weber, T., Michel, T., and Anton, G. (2013). Projection angle dependence in grating-based x-ray dark-field imaging of ordered structures. *Opt. Express*, 21(17):19922–19933.

Bayer, F. L., Hu, S., Maier, A., Weber, T., Anton, G., Michel, T., and Riess, C. P. (2014). Reconstruction of scalar and vectorial components in x-ray dark-field tomography. *Proceedings of the National Academy of Sciences*, 111(35):12699–12704.

Bech, M. (2009). *X-ray imaging with a grating interferometer*. PhD thesis, University of Copenhagen.

Bech, M., Bunk, O., Donath, T., Feidenhans'l, R., David, C., and Pfeiffer, F. (2010). Quantitative x-ray dark-field computed tomography. *Physics in Medicine and Biology*, 55(18):5529–5539.

Birnbacher, L., Willner, M., Velroyen, A., Marschner, M., Hipp, A., Meiser, J., Koch, F., Schröter, T., Kunka, D., Mohr, J., Pfeiffer, F., and Herzen, J. (2016). Experimental Realisation of High-sensitivity Laboratory X-ray Grating-based Phase-contrast Computed Tomography. *Scientific Reports*, 6:24022.

Cloetens, P., Guigay, J. P., De Martino, C., Baruchel, J., and Schlenker, M. (1997). Fractional Talbot imaging of phase gratings with hard x rays. *Optics letters*, 22(14):1059–1061.

Cnudde, V. and Boone, M. N. (2013). High-resolution X-ray computed tomography in geosciences: A review of the current technology and applications. *Earth-Science Reviews*, 123:1–17.

Coello, E., Sperl, J. I., Bequé, D., Benz, T., Scherer, K., Herzen, J., Sztrókay-Gaul, A., Hellerhoff, K., Pfeiffer, F., Cozzini, C., and Grandl, S. (2017). Fourier domain image fusion for differential x-ray phase-contrast breast imaging. *European Journal of Radiology*, 89:27–32.

Cormack, A. M. (1963). Representation of a function by its line integrals, with some radiological applications. *Journal of Applied Physics*, 34(9):2722–2727.

Cormack, A. M. (1964). Representation of a function by its line integrals, with some radiological applications. ii. *Journal of Applied Physics*, 35(10):2908–2913.

Creath, K. (1988). V phase-measurement interferometry techniques. volume 26 of *Progress in Optics*, pages 349 – 393. Elsevier.

Eggl, E., Malecki, A., Schaff, F., Potdevin, G., Noël, P. B., Bauer, J. S., Gordijenko, O., Grande García, E., Burgkart, R., Rummeny, E. J., Baum, T., and Pfeiffer, F. (2015). Prediction of Vertebral Failure Load by Using X-Ray Vector Radiographic Imaging. *Radiology*, 275(2):553–561.

Feldkamp, J. M., Kuhlmann, M., Roth, S. V., Timmann, A., Gehrke, R., Shakhverdova, I., Paufler, P., Filatov, S. K., Bubnova, R. S., and Schroer, C. G. (2009). Recent developments in tomographic small-angle X-ray scattering. *Phys. Status Solidi A*, 206(8):1723–1726.

Francesco, S. D. and da Silva, A. M. F. (2004). Efficient NUFFT-based direct Fourier algorithm for fan beam CT reconstruction. In *Proc. SPIE, Medical Imaging 2004: Image Processing*, volume 5370, pages 5312–5370.

Fratzl, P., Jakob, H. F., Rinnerthaler, S., Roschger, P., and Klaushofer, K. (1997). Position-Resolved Small-Angle X-ray Scattering of Complex Biological Materials. *Journal of Applied Crystallography*, 30(5 Part 2):765–769.

Funk, P. (1913). Über Flächen mit lauter geschlossenen geodätischen Linien. *Math. Ann.*, 74(2):278–300.

Gage, S. H. (1920). Modern dark-field microscopy and the history of its development. *Transactions of the American Microscopical Society*, 39(2):95–141.

Glatter, O. and Kratky, O. (1982). *Small Angle X-Ray Scattering*. Academic Press.

Gresil, M., Revol, V., Kitsianos, K., Kanderakis, G., Koulalis, I., Sauer, M. O., Trétout, H., and Madrigal, A. M. (2017). EVITA Project: Comparison Between Traditional Non-Destructive Techniques and Phase Contrast X-Ray Imaging Applied to Aerospace Carbon Fibre Reinforced Polymer. *Applied Composite Materials*, 24(2):513–524.

Gromann, L. B., De Marco, F., Willer, K., Noîl, P. B., Scherer, K., Renger, B., Gleich, B., Achterhold, K., Fingerle, A. A., Muenzel, D., Auweter, S., Hellbach, K., Reiser, M., Baehr, A., Dmochewitz, M., Schroeter, T. J., Koch, F. J., Meyer, P., Kunka, D., Mohr, J., Yaroshenko, A., Maack, H.-I., Pralow, T., van der Heijden, H., Proksa, R., Koehler, T., Wieberneit, N., Rindt, K., Rummeny, E. J., Pfeiffer, F., and Herzen, J. (2017). In-vivo x-ray dark-field chest radiography of a pig. *Scientific Reports*, 7(1).

Guinier, A. and Fournet, G. (1955). *Small-angle scattering of X-rays*. Structure of matter series. Wiley.

Hamam, H. (1997). Talbot array illuminators: general approach. *Applied optics*, 36(11):2319–27.

Hannesschlager, C., Revol, V., Plank, B., Salaberger, D., and Kastner, J. (2015). Fibre structure characterisation of injection moulded short fibre-reinforced polymers by x-ray scatter dark field tomography. *Case Studies in Nondestructive Testing and Evaluation*, 3:34 – 41.

Hardin, R. H. and Sloane, N. J. A. (1996). Mclaren's improved snub cube and other new spherical designs in three dimensions. *Discrete & Computational Geometry*, 15(4):429–441.

Hellbach, K., Baehr, A., De Marco, F., Willer, K., Gromann, L. B., Herzen, J., Dmochewitz, M., Auweter, S., Fingerle, A. A., Noël, P. B., Rummeny, E. J., Yaroshenko, A., Maack, H.-I., Pralow, T., van der Heijden, H., Wieberneit, N., Proksa, R., Koehler, T., Rindt, K., Schroeter, T. J., Mohr, J., Bamberg, F., Ertl-Wagner, B., Pfeiffer, F., and Reiser, M. F. (2018). Depiction of pneumothoraces in a large animal model using x-ray dark-field radiography. *Scientific Reports*, 8(1).

Hetterich, H., Webber, N., Willner, M., Herzen, J., Birnbacher, L., Auweter, S., SchÃŒller, U., Bamberg, F., Notohamiprodjo, S., Bartsch, H., Wolf, J., Marschner, M., Pfeiffer, F., Reiser, M., and Saam, T. (2017). Dark-field imaging in coronary atherosclerosis. *European Journal of Radiology*, 94:38 – 45.

H.F., T. (1836). Lxxvi. facts relating to optical science. no. iv. *The London, Edinburgh, and Dublin Philosophical Magazine and Journal of Science*, 9(56):401–407.

Hotelling, H. (1933). *Analysis of a complex of statistical variables into principal components.*, volume 24. Warwick & York, US.

Jahns, J. and Lohmann, A. (1979). The lau effect (a diffraction experiment with incoherent illumination). *Optics Communications*, 28(3):263 – 267.

Jensen, T. H., Bech, M., Bunk, O., Donath, T., David, C., Feidenhans'l, R., and Pfeiffer, F. (2010). Directional x-ray dark-field imaging. *Physics in Medicine and Biology*, 55(12):3317.

Joseph, P. M. (1982). An improved algorithm for reprojecting rays through pixel images. *IEEE Transactions on Medical Imaging*, 1(3):192–196.

Jud, C., Schaff, F., Zanette, I., Wolf, J., Fehringer, A., and Pfeiffer, F. (2016). Dentinal tubules revealed with x-ray tensor tomography. *Dental Materials*, 32:1189–1195.

Kagias, M., Wang, Z., Jefimovs, K., and Stampanoni, M. (2017). Dual phase grating interferometer for tunable dark-field sensitivity. *Applied Physics Letters*, 110(1):014105.

Kagias, M., Wang, Z., Villanueva-Perez, P., Jefimovs, K., and Stampanoni, M. (2016). 2d-omnidirectional hard-x-ray scattering sensitivity in a single shot. *Physical Review Letters*, 116:093902.

Kang, H., Attota, R., Tondare, V., VladÃ¡r, A. E., and Kavuri, P. (2015). A method to determine the number of nanoparticles in a cluster using conventional optical microscopes. *Applied Physics Letters*, 107(10):103106.

Kevles, B. (1997). *Naked to the Bone: Medical Imaging in the Twentieth Century*. Sloan technology series. Rutgers University Press.

Kinney, J., Pople, J., Marshall, G., and Marshall, S. (2001). Collagen Orientation and Crystallite Size in Human Dentin: A Small Angle X-ray Scattering Study. *Calcified Tissue International*, 69(1):31–37.

Klaus, W. and Arimoto, Y. (1997). Talbot array illuminators providing spatial intensity and phase modulation. *Journal of the Optical Society of America A*, 14(5):1092–1102.

Koehler, T., Daerr, H., Martens, G., Kuhn, N., Löscher, S., van Stevendaal, U., and Roessl, E. (2015). Slit-scanning differential x-ray phase-contrast mammography: Proof-of-concept experimental studies. *Medical Physics*, 42(4):1959–1965.

Kottler, C., Pfeiffer, F., Bunk, O., GrÃŒnzweig, C., and David, C. (2007). Grating interferometer based scanning setup for hard x-ray phase contrast imaging. *Review of Scientific Instruments*, 78(4):043710.

Lauridsen, T., Lauridsen, E. M., and Feidenhans'l, R. (2014). Mapping misoriented fibers using X-ray dark field tomography. *Applied Physics A*, 115(3):741–745.

Loewen, E. and Popov, E. (1997). *Diffraction Gratings and Applications*. Optical Science and Engineering. Taylor & Francis.

Lohmann, A. W. and Thomas, J. A. (1990). Making an array illuminator based on the Talbot effect. *Applied Optics*, 29(29):4337.

Lynch, S. K., Pai, V., Auxier, J., Stein, A. F., Bennett, E. E., Kemble, C. K., Xiao, X., Lee, W.-K., Morgan, N. Y., and Wen, H. H. (2011). Interpretation of dark-field contrast and particle-size selectivity in grating interferometers. *Appl. Opt.*, 50(22):4310–4319.

Maire, E. and Withers, P. J. (2014). Quantitative x-ray tomography. *International Materials Reviews*, 59(1):1–43.

Malecki, A., Potdevin, G., Biernath, T., Eggl, E., Grande Garcia, E., Baum, T., NoÃ«l, P. B., Bauer, J. S., and Pfeiffer, F. (2013). Coherent superposition in grating-based directional dark-field imaging. *PLOS ONE*, 8(4):1–7.

Malecki, A., Potdevin, G., Biernath, T., Eggl, E., Willer, K., Lasser, T., Maisenbacher, J., Gibmeier, J., Wanner, A., and Pfeiffer, F. (2014). X-ray tensor tomography. *EPL (Europhysics Letters)*, 105(3):38002.

Mardia, K. V. and Jupp, P. E. (2008). *Distributions on Spheres*, pages 159–192. John Wiley and Sons, Inc.

Marschner, M., Willner, M., Potdevin, G., Fehringer, A., Noël, P. B., Pfeiffer, F., and Herzen, J. (2016). Helical X-ray phase-contrast computed tomography without phase stepping. *Scientific reports*, 6:23953.

Miao, H., Chen, L., Bennett, E. E., Adamo, N. M., Gomella, A. A., DeLuca, A. M., Patel, A., Morgan, N. Y., and Wen, H. (2014). Motionless phase stepping in X-ray phase contrast imaging with a compact source. *Proceedings of the National Academy of Sciences*, 111(52):18799–18799.

Modregger, P., Pinzer, B. R., Thüring, T., Rutishauser, S., David, C., and Stampanoni, M. (2011). Sensitivity of X-ray grating interferometry. *Optics Express*, 19(19):18324.

Momose, A. (2005). Recent Advances in X-ray Phase Imaging. *Japanese Journal of Applied Physics*, 44(9A):6355–6367.

Momose, A., Kawamoto, S., Koyama, I., Hamaishi, Y., Takai, K., and Suzuki, Y. (2003). Demonstration of x-ray Talbot interferometry. *Japanese Journal of Applied Physics, Part 2: Letters*, 42(7 B):5–8.

Natterer, F. (2001). *The Mathematics of Computerized Tomography*. Society for Industrial and Applied Mathematics.

Nayar, S. K. and Nakagawa, Y. (1994). Shape from focus. *IEEE Transactions on Pattern Analysis and Machine Intelligence*, 16(8):824–831.

Nielsen, M. S., Christensen, L. B., and Feidenhans'l, R. (2014). Frozen and defrosted fruit revealed with X-ray dark-field radiography. *Food Control*, 39(1):222–226.

Paganin, D. (2006). *Coherent X-Ray Optics*. Oxford University Press (OUP).

Pennec, X., Fillard, P., and Ayache, N. (2006). A Riemannian Framework for Tensor Computing. *Int J Comput Vision*, 66(1):41–66.

Pfeiffer, F., Bech, M., Bunk, O., Kraft, P., Eikenberry, E. F., Brönnimann, C., Grünzweig, C., and David, C. (2008). Hard-X-ray dark-field imaging using a grating interferometer. *Nature materials*, 7(2):134–137.

Pfeiffer, F., Weitkamp, T., Bunk, O., and David, C. (2006). Phase retrieval and differential phase-contrast imaging with low-brilliance X-ray sources. *Nature Physics*, 2(4):258–261.

Potdevin, G., Malecki, A., Biernath, T., Bech, M., Jensen, T. H., Feidenhans'l, R., Zanette, I., Weitkamp, T., Kenntner, J., Mohr, J., Roschger, P., Kerschnitzki, M., Wagermaier, W., Klaushofer, K., Fratzl, P., and Pfeiffer, F. (2012). X-ray vector radiography for bone micro-architecture diagnostics. *Physics in Medicine and Biology*, 57(11):3451–3461.

Prade, F., Schaff, F., Senck, S., Meyer, P., Mohr, J., Kastner, J., and Pfeiffer, F. (2016). Nondestructive characterization of fiber orientation in short fiber reinforced polymer composites with X-ray vectorradiography. *NDT & E International*, 86(August 2016):65–72.

Prade, F., Yaroshenko, A., Herzen, J., and Pfeiffer, F. (2015). Short-range order in mesoscale systems probed by X-ray grating interferometry. *EPL (Europhysics Letters)*, 112(6):68002.

Radon, J. (1986). On the determination of functions from their integral values along certain manifolds. *IEEE Transactions on Medical Imaging*, 5(4):170–176.

Revol, V., Kottler, C., Kaufmann, R., Neels, A., and Dommann, A. (2012). Orientation-selective x-ray dark field imaging of ordered systems. *Journal of Applied Physics*, 112(11):114903.

Revol, V., Plank, B., Kaufmann, R., Kastner, J., Kottler, C., and Neels, A. (2013). Laminate fibre structure characterisation of carbon fibre-reinforced polymers by X-ray scatter dark field imaging with a grating interferometer. *NDT & E International*, 58:64–71.

Rieger, J., Bayer, F., Durst, J., Gödel, K., Haas, W., Horn, F., Michel, T., Pelzer, G., Ritter, A., Weber, T., Zang, A., and Anton, G. (2013). Grating-based dark-field breast imaging. In *Proc. SPIE Medical Imaging 2013: Physics of Medical Imaging*, volume 8668, pages 866810–866816.

Rinnerthaler, S., Roschger, P., Jakob, H. F., Nader, A., Klaushofer, K., and Fratzl, P. (1999). Scanning Small Angle X-ray Scattering Analysis of Human Bone Sections. *Calcified Tissue International*, 64(5):422–429.

Schaff, F. (2017). *Directional Small-Angle X-ray Scattering Computed Tomography*. Phd thesis, Technical University of Munich.

Schaff, F., Bech, M., Zaslansky, P., Jud, C., Liebi, M., Guizar-Sicairos, M., and Pfeiffer, F. (2015). Six-dimensional real and reciprocal space small-angle X-ray scattering tomography. *Nature*, 527(7578):353–356.

Schaff, F., Malecki, A., Potdevin, G., Eggl, E., Noël, P. B., Baum, T., Garcia, E. G., Bauer, J. S., and Pfeiffer, F. (2014). Correlation of X-ray vector radiography to bone micro-architecture. *Scientific reports*, 4:3695.

Schaff, F., Prade, F., Sharma, Y., Bech, M., and Pfeiffer, F. (2017). Non-iterative Directional Dark-field Tomography. *Scientific Reports*, 7(1):3307.

Scherer, K., Yaroshenko, A., Bölükbas, D. A., Gromann, L. B., Hellbach, K., Meinel, F. G., Braunagel, M., Berg, J. v., Eickelberg, O., Reiser, M. F., Pfeiffer, F., Meiners, S., and Herzen, J. (2017). X-ray dark-field radiography - in-vivo diagnosis of lung cancer in mice. *Scientific Reports*, 7(1).

Scholkmann, F., Revol, V., Kaufmann, R., Baronowski, H., and Kottler, C. (2014). A new method for fusion, denoising and enhancement of x-ray images retrieved from Talbot-Lau grating interferometry. *Physics in Medicine and Biology*, 59(6):1425–1440.

Sharma, Y., Bachche, S., Kageyama, M., Kuribayashi, M., Pfeiffer, F., Lasser, T., and Momose, A. (2018). Trochoidal X-ray Vector Radiography: Directional dark-field without grating stepping. *Applied Physics Letters*, 112(11):111902.

Sharma, Y., Schaff, F., Wieczorek, M., Pfeiffer, F., and Lasser, T. (2017). Design of Acquisition Schemes and Setup Geometry for Anisotropic X-ray Dark-Field Tomography (AXDT). *Scientific Reports*, 7(1):3195.

Sharma, Y., Wieczorek, M., Schaff, F., Seyyedi, S., Prade, F., Pfeiffer, F., and Lasser, T. (2016). Six dimensional x-ray tensor tomography with a compact laboratory setup. *Applied Physics Letters*, 109(13):134102.

Strobl, M. (2014). General solution for quantitative dark-field contrast imaging with grating interferometers. *Scientific Reports*, 4:7243.

Suleski, T. J. (1997). Generation of Lohmann images from binary-phase Talbot array illuminators. *Applied optics*, 36(20):4686–4691.

Takeda, M., Ina, H., and Kobayashi, S. (1982). Fourier-transform method of fringe-pattern analysis for computer-based topography and interferometry. *J. Opt. Soc. Am.*, 72(1):156–160.

Tanaka, J., Nagashima, M., Kido, K., Hoshino, Y., Kiyohara, J., Makifuchi, C., Nishino, S., Nagatsuka, S., and Momose, A. (2013). Cadaveric and in vivo human joint imaging based on differential phase contrast by x-ray talbot-lau interferometry. *Zeitschrift für medizinische Physik*, 23(3):222–227.

Testorf, M. and neda, J. O.-C. (1996). Fractional talbot effect: analysis in phase space. *J. Opt. Soc. Am. A*, 13(1):119–125.

Teuffenbach, M. v., Koehler, T., Fehringer, A., Viermetz, M., Brendel, B., Herzen, J., Proksa, R., Rummeny, E. J., Pfeiffer, F., and Noel, P. B. (2017). Grating-based phase-contrast and dark-field computed tomography: a single-shot method. *Scientific Reports*, 7(1).

Thüring, T., Guggenberger, R., Alkadhi, H., Hodler, J., Vich, M., Wang, Z., David, C., and Stampanoni, M. (2013). Human hand radiography using x-ray differential phase contrast combined with dark-field imaging. *Skeletal radiology*, 42(6):827–835.

Vogel, J., Schaff, F., Fehringer, A., Jud, C., Wieczorek, M., Pfeiffer, F., and Lasser, T. (2015). Constrained X-ray tensor tomography reconstruction. *Opt. Express*, 23(12):15134–15151.

Wang, Z., Hauser, N., Singer, G., Trippel, M., Kubik-Huch, R. a., Schneider, C. W., and Stampanoni, M. (2014). Non-invasive classification of microcalcifications with phase-contrast X-ray mammography. *Nature communications*, 5(May):3797.

Weitkamp, T., Diaz, A., David, C., Pfeiffer, F., Stampanoni, M., Cloetens, P., and Ziegler, E. (2005). X-ray phase imaging with a grating interferometer. *Optics Express*, 13(16):6296.

Wieczorek, M. (2017). *Anisotropic X-ray Dark-field Tomography*. Phd thesis, Technical University of Munich.

Wieczorek, M., Schaff, F., Pfeiffer, F., and Lasser, T. (2016). Anisotropic X-Ray Dark-Field Tomography: A Continuous Model and its Discretization. *Physical Review Letters*, 117(15):158101.

Withers, P. J. (2007). X-ray nanotomography. *Materials Today*, 10(12):26–34.

Wolf, J., Sperl, J. I., Schaff, F., Schüttler, M., Yaroshenko, A., Zanette, I., Herzen, J., and Pfeiffer, F. (2015). Lens-term- and edge-effect in X-ray grating interferometry. *Biomedical Optics Express*, 6(12):4812–4824.

Yang, Y. and Tang, X. (2012). The second-order differential phase contrast and its retrieval for imaging with x-ray Talbot interferometry. *Medical Physics*, 39(12):7237–7253.

Yashiro, W., Harasse, S., Kawabata, K., Kuwabara, H., Yamazaki, T., and Momose, A. (2011). Distribution of unresolvable anisotropic microstructures revealed in visibility-contrast images using x-ray Talbot interferometry. *Physical Review B*, 84(9):094106.

Yashiro, W. and Momose, A. (2015). Effects of unresolvable edges in grating-based x-ray differential phase imaging. *Opt. Express*, 23(7):9233–9251.

Yashiro, W., Noda, D., and Kajiwara, K. (2017). Sub-10-ms X-ray tomography using a grating interferometer. *Applied Physics Express*, 10(5).

Yashiro, W., Terui, Y., Kawabata, K., and Momose, A. (2010). On the origin of visibility contrast in x-ray talbot interferometry. *Opt. Express*, 18(16):16890–16901.

Yokozeki, S. (1982). Moire fringes. *Optics and Lasers in Engineering*, 3(1):15 – 27.

Dissemination

Journal Publications as first author

1. **Sharma, Y.**, Bachche, S., Kageyama, M., Kuribayashi, M., Pfeiffer, F., Lasser, T., and Momose, A. (2018). Trochoidal X-ray Vector Radiography: Directional dark-field without grating stepping. Applied Physics Letters, 112(11):111902.

2. **Sharma, Y.**, Schaff, F., Wieczorek, M., Pfeiffer, F., and Lasser, T. (2017). Design of Acquisition Schemes and Setup Geometry for Anisotropic X-ray Dark-Field Tomography (AXDT). Scientific Reports, 7(1):3195.

3. **Sharma, Y.**, Wieczorek, M., Schaff, F., Seyyedi, S., Prade, F., Pfeiffer, F., and Lasser, T. (2016). Six dimensional x-ray tensor tomography with a compact laboratory setup. Applied Physics Letters, 109(13):134102.

Journal Publications as co-author

1. Schaff, F., Prade, F., **Sharma, Y.**, Bech, M., and Pfeiffer, F. (2017). Non-iterative Directional Dark-field Tomography. Scientific Reports, 7(1):3307.

2. Han, H., **Sharma, Y.**, Zan, G., Wu, Z., Wang, S., Wu, Y., Momose, A., Zhai, C. Preliminary research on body composition measurement using X-ray phase contrast imaging. Submitted.

Conference Proceedings

1. Boghiu, T. C., **Sharma, Y.**, Pfeiffer, F., Lasser, T. Detectability Indices in Anisotropic X-ray Dark-field Tomography. International Conference on Image Formation in X-Ray Computed Tomography, Salt Lake City, USA, May 2018.

2. Vegso, K., Takano, H., Wu, Y., Hoshino, M., Han, H., **Sharma, Y.**, Momose, A. The dynamical structural changes in polymers induced by laser irradiation studied by spectrum-tuned 4D X-ray phase tomography based on X-ray Talbot interferometry. JSAP-OSA Joint Symposia, 2017 Abstracts, (Optical Society of America, 2017).

3. **Sharma, Y.**, Schaff, F., Wieczorek, M., Pfeiffer, F., Lasser T. Acquisition Schemes for Directional Dark-field Imaging Modalities. International Meeting on Fully Three-Dimensional Image Reconstruction in Radiology and Nuclear Medicine (Fully3D), Xi'an Shaanxi, China, June 2017.

4. **Sharma, Y.**, Wieczorek, M., Jud, C., Schaff, F., Pfeiffer, F., Lasser T. X-ray Tensor Tomography: How much to measure? International Conference on Image Formation in X-Ray Computed Tomography, Bamberg, Germany, July 2016.

5. Seyyedi, S., Wieczorek M., Sharma Y., Schaff F., Jud C., Pfeiffer F., Lasser T. Component-based TV Regularization for X-ray Tensor Tomography International Symposium on Biomedical Imaging (ISBI), Prague, Czech Republic, April 2016.

Oral Presentations

1. Scanning X-ray Vector Radiography. International conference on X-ray and Neutron Phase Imaging with Gratings, Zurich, Switzerland, 2017.

2. Acquisition Schemes for Anisotropic X-ray Dark-field Tomography. International Conference on Fully Three-Dimensional Image Reconstruction in Radiology and Nuclear Medicine, Xi'an Shaanxi, China, 2017.

Poster Presentations

1. Trochoidal X-ray Vector Radiography: Directional Dark-field without grating stepping. KNMF User Meeting, Karslruhe, Germany, 2018

2. Trochoidal X-ray Vector Radiography: Directional Dark-field without grating stepping. International Symposium on BioMedical Applications of X-Ray Phase Contrast Imaging, Garmisch-Partenkirchen, Germany, 2018.

3. X-ray Tensor Tomography: Towards Compact Imaging Setups. International Conference X-ray Microscopy, Oxford, UK, 2016.

4. X-ray Tensor Tomography: How much to measure? International Conference on Image Formation in X-Ray Computed Tomography, Bamberg, Germany, July 2016.

5. X-ray Tensor Tomography: How much to measure? International Symposium on BioMedical Applications of X-Ray Phase Contrast Imaging, Garmisch-Partenkirchen, Germany, 2016.

Patent Applications

1. **Sharma, Y.**, Momose, A., Kageyama, M., Nonoguchi, M. (2017) Method and Apparatus for Radiation Imaging. Japanese Patent Application, within embargo, patent pending.

2. **Sharma, Y.**, Lasser, T., Pfeiffer, F. (2017) X-ray Tensor Tomography System. International Patent Application, WO2017216178A1, patent pending.

3. **Sharma, Y.**, Lasser, T., Pfeiffer, F. (2016) X-ray Tensor Tomography System. European Patent Application, EP3258253A1, patent pending.

Acknowledgements

Even though I am listed as the sole author of this thesis, I used the pronoun 'We' throughout the text (except this section), because everything in this thesis is the result of a collective effort of a lot of people and I would like to dedicate this section for thanking each and every one of them.

First of all, I wish to thank Prof. Dr. Franz Pfeiffer for providing me the opportunity to be a part of his research group. I feel lucky to have gotten this amazing opportunity in what is undoubtedly one of the best research groups in the world. The kind of guidance, opportunities and resources you provided me for this thesis is incredible and invaluable. You always managed to be available for me despite your busy schedule and made sure that I always got everything I needed in a timely manner. I can't imagine how you do it!

I am extremely thankful to Dr. Tobias Lasser for being so much more than my second supervisor. You have been a colleague, friend, troubleshooter, and simply the best supervisor I could have hoped for. I wish to thank you for guiding me like a baby in the stressful Phd journey, and for bearing with my stupidest of issues at any time of the day or night. You always managed to provide just the right amount of push for me to be successful without being stressed. None of my work would have been published if it was not for you pushing me to do so and for guiding me through the grinding processes. The progress in my writing skills from the first paper in 2015 to today is phenomenal and I owe it solely to you!

I want to thank Prof. Dr. Atsushi Momose at Tohoku university for hosting me as a visiting student for 7 months last year. This was another excellent opportunity where I got to experience life and research in a completely different setting. I am thankful to you for exposing me to so many other research directions, especially at synchrotrons. You were always available for me during and after my stay in Japan and our numerous scientific discussions enriched my knowledge by leaps and bounds. I feel fortunate to have worked with a scientist of your stature.

It was close to impossible for me to have availed such opportunities, if it was not for BERTI. I wish to thank Petra and Katharina for their efforts in initiating this program and to Andrea for seeing it through till the end, all of whom always went out of their way to help us out. Your support was invaluable to the group of 14 international researchers struggling to make sense of life in Germany. We got to step out of our respective labs every now and then for BERTI events, which were always fun and exciting besides imparting us invaluable transferrable skills.